Dynamical Decoupling Based Quantum Sensing: Floquet Analysis and Finite-Duration-Pulse Effects

Jacob Lang

University College London

A dissertation submitted for the degree of

Doctor of Philosophy

September 2018

Declaration

I, Jacob Lang, confirm that the work presented in this thesis is my own. Where information has been derived from other sources, I confirm that this has been indicated in the thesis.

Jacob Lang

September 2018

Abstract

A spin qubit can be protected from a dephasing spin bath using dynamical decoupling (DD). Microwave π-pulses are repeatedly applied to the spin qubit to invert its state and average out any dephasing. Importantly, this protection fails when the DD pulse spacing is resonant with nuclear spins in the bath and characteristic dips appear in coherence traces forming the basis for nanoscale NMR and MRI. This emerging quantum technology has been demonstrated with the nitrogen vacancy center in diamond.

Most DD protocols apply periodic repetitions of a basic pulse unit. This repetition motivates us to model the experiments using Floquet analysis. The characteristic coherence dips are found to be associated with avoided crossings in an underlying Floquet spectrum. The width and shape of these crossings determines the contrast and sharpness of the coherence dips. We derive analytic expressions for the coherence dips in terms of the Floquet quasienergies and Floquet modes.

Typically, the DD microwave pulses are modelled as being instantaneous; however, real pulses have some finite duration and it was recently demonstrated that this pulse duration can cause extra dips to appear in coherence traces. We apply Floquet analysis to accurately model the complete system dynamics in the presence of these finite duration pulses and derive analytic expressions for the complete coherence response. We interpret the arrival of extra coherence dips as the opening of previously closed avoided crossings. We use this new understanding to propose protocols to exploit (for increased resolution) or suppress these extra coherence dips.

Finally, we model the interplay between finite-duration-pulse effects and microwave detuning errors - an important problem as the detuning error is completely removed by instantaneous pulses so is not captured by most analytic models. We observe drastic effects including the splitting and suppression of the expected DD signal.

Impact Statement

The importance of standard NMR and MRI cannot be overstated. The application to medical imaging alone proved revolutionary - offering an extremely detailed and totally non-invasive window inside the human body. Beyond medical imaging the tools are applicable for the structure determination of almost any substance. The shortcoming of standard NMR and MRI is the inductive detection of the magnetic resonance which places limits on its sensitivity and spatial resolution. Magnetic resonance detection with nitrogen vacancy centers in diamond promises a new *nanoscale* NMR and MRI platform capable of detecting and imaging at the single atom and single molecule level. The work presented in this thesis contributes to the future realisation of functionalised nanoscale NMR and MRI.

The nitrogen vacancy (NV) center has not just been used for magnetic resonance detection but also for a wealth of other applications. The NV is sensitive to a range of physical properties and can be used for the detection of nanoscale magnetic and electric fields, temperatures, pressures and rotations. NV centers have been used to address quantum registers of nuclear spins for quantum computing purposes, are the basis of room temperature masers and have been used to dynamically polarise samples for increased sensitivity in standard NMR and MRI. Alongside being a versatile platform for new quantum technologies the NV center can be used to test concepts in fundamental physics such as the measurement problem and local realism. The field is inherently cross-disciplinary - sitting at the border of quantum physics and nano-engineering and finds applicability across all of science. The work presented in this thesis adds to a growing understanding of the NV center dynamics (in particular under dynamical decoupling control) which is essential for designing new applications and interpreting experimental data. The theoretical analysis is also quite general and can be readily applied to the study of new defect centers (e.g. silicon, germanium and tin vacancies in diamond and defects in silicon carbide and silicon) that are being explored as a result of NV center's success.

More specifically the work presented in this thesis provides mathematical tools for

understanding the sensor response in quantum sensing experiments. We elucidate the full system dynamics under realistic experimental conditions (by modelling the effect of finite duration pulses with and without detuning errors). We provide new experimental protocols for enhancing capabilities in sensing experiments which can be used to obtain enhanced resolution or to suppress unwanted signals. Whilst nanoscale NMR and MRI are still at the proof-of-concept stage the maturing field has already started to see the formation of industrial spin-off companies. As the technology develops, any advances will rely on the understanding laid down in this work and others like it.

Acknowledgements

First and foremost I must express my sincere gratitude to my supervisor Professor Tania Monteiro. Tania has consistently been a greater champion of my work and character than I ever have and her never ending enthusiasm and support during my PhD and now my early research career is truly appreciated.

I must also thank the collaborators who we have published work with. I was lucky enough to make connections with some truly great scientists and leaders in our field and I learnt a great deal from each one of them. Professor Ren Bao Liu at the Chinese University of Hong Kong hosted me on several occasions, including one two-month stay, and collaborated with us on our first paper. Professor Martin Plenio, Dr Jorge Casanova and Dr Zhenyu Wang at the University of Ulm also hosted me several times and collaborated with us on our second paper. Dr Jean-Philippe Tetienne, Dr Alastair Stacey, David Broadway and others at the University of Melbourne provided us with our first experimental collaboration which resulted in our third paper. I would like to thank them all for committing their time to work with us. I thank Dr Seto Balian who provided invaluable help at the start of my PhD and also Dr Tim Taminiau and Mohamed Abobeih at DELFT who provided experimental data to explore. Thanks also to the numerous other researchers that provided illuminating discussions throughout my PhD, including, among others, Dr Gavin Morley, Dr Wen Long Ma, the entire optomechanics group at UCL and my viva examiners Dr Eran Ginossar and Dr Animesh Datta.

I have been lucky to share my time at UCL with a group of incredibly talented friends who never fail to inspire and occasionally bewilder me: Erika Aranas, Andrew Maxwell, Katy Chubb, Richard Juggins, Harry Banks, Tom Meltzer, Stefan Siwiak-Jaszek, Duncan Little, the C25 boys, Paul Brookes, Sarah Hussain and many others. Our lunchtime talks have occasionally been stimulating debates but more often than not they have been entirely inane and a welcome break from a day of thinking too hard. I will also remember fondly my time at the Chinese University of Hong Kong, hiking and swimming with Qile and

Jelle.

I always say I ended up studying physics and maths because I hated writing essays - which has clearly backfired - but I must also thank Dr Capaldi and Mr Hubert, my physics and maths teachers at school, who taught so well and guided my early interest in the subjects.

I acknowledge the UK Engineering and Physical Sciences Research Council (and all UK tax payers!) for their generous support - I always considered being paid to go to university a massive privilege - and I thank UCL for hosting me.

Lastly, I'd like to to say that the last four years in London have been absolutely amazing and I thank *all* my family and friends for making this time so much fun. In particular, I say thank you to my parents for supporting me through everything.

Contents

List of Figures

List of Tables

1 Introduction

The detection of remote single nuclear spins via the nitrogen vacancy (NV) center defect in diamond [1, 2, 3] represents an important milestone in the effort to realise single molecule nuclear magnetic resonance (NMR) and magnetic resonance imaging (MRI) [4, 5, 6]. NMR and MRI [7] are well established and powerful tools for determining the structure of materials with a vast range of applications, ranging from medical imaging to chemical analysis. However, these schemes, which detect the sample net magnetisation, rely on the very small statistical polarisation of spins in the sample. This requirement sets a lower limit on the number of spins that can be detected (the sensitivity) and thus the voxel size in imaging applications (the spatial resolution). Typically, NMR is limited to Avogadro's numbers of spins and micron resolution. Increases in NMR sensitivity can be achieved by applying strong magnetic fields or cryogenic cooling, which both increase the sample polarisation, but this removes the technique's attractive bio-compatibility for in-vivo and in-vitro samples. Experiments with the nitrogen vacancy defect center in diamond [8] (and other solid state defect centers [9, 10, 11]) have paved the way towards NMR and MRI of single molecules in *ambient* conditions - promising, amongst other things, a wealth of applications in the life sciences [12].

The nitrogen vacancy center in diamond is formed of a substitutional nitrogen atom neighbouring a vacant site in the carbon lattice. The defect has an optically addressable spin-1 ground state that couples to other local spins offering a window into its nanoscale environment. Prior to the detection of remote nuclear spins [1, 2, 3], NV based NMR experiments were limited to the detection of nearest-neighbour or proximal nuclear spins that couple strongly to the NV [13, 14, 15]. These spins can be a valuable resource [14] but for sensing purposes a larger detection range is desirable. More remote spins, weakly coupled to the NV center are harder to detect as their signal is typically embedded in the noise from a bath of other nuclear spins in the environment. The key to detecting weak nuclear spins is dynamical decoupling (DD) [16] - the repeated application of microwave

pulses to invert the state of the NV sensor. Dynamical decoupling functions two-fold: it averages out environmental noise, extending the sensor coherence time (and thus the sample interrogation time) and it amplifies the weak signals from target nuclear spins. The nuclear spins are detected via the characteristic dips they imprint onto sensor coherence traces.

The first dynamical decoupling based detection of remote spins was demonstrated on single ^{13}C nuclear spin-1/2s resident in the diamond lattice itself [1, 2, 3]. Since then, the scheme has been extended to detect resident nuclear spin clusters [17, 18], electron spins external to the diamond [19, 20], nanoscale size samples of nuclear spins placed on the diamond surface [21, 22, 23] and finally external single nuclear spins [24, 25, 26]. The ultimate goal being a functionalised nanoscale NMR and MRI sensor for the complete structure determination and imaging of single molecules.

In addition to detection, the coupling between the NV center and these nuclei means the NV can be used to address nuclear spin states and form a quantum register. Quantum registers of proximal nuclear spins [14, 27, 28, 29] and remote nuclear spins [30] have been demonstrated. These registers are capable of initialisation, readout, entanglement and quantum error correction algorithms for quantum information applications [31] or even to assist sensing as ancilla qubits or quantum memories [26, 32, 33, 29, 34].

1.1 Motivation

The emerging technology of NV-based nanoscale NMR and MRI shows great promise and has achieved several important milestones. These experimental achievements must be paired with an accurate and instructive analytic model of the system dynamics under different experimental protocols. This need is clear in two cases: Firstly, in sensing experiments one must derive information from the features within experimental data and analytic models relate these features to the physical parameters of interest. Secondly, when designing new protocols to control the system in a desired way an accurate understanding of how the system behaves is required.

Dynamical decoupling based sensing experiments have been analysed with a mixture of semi-classical methods - where the nuclear spin signal is treated as classical oscillating magnetic field - and more quantum methods where the nuclear spin is treated as a quantum state that couples to the NV center. Semi-classical analysis interprets the dynamical decoupling as a narrow band filter that averages out any signals not resonant with the pulse spacing. The characteristic dips in sensor coherence appear when the dynamical decoupling

is resonant with an incident AC magnetic signal. By scanning the dynamical decoupling pulse spacing one can reconstruct the noise spectrum of the spin bath and detect single nuclear spins as distinct peaks in this spectrum [35, 1, 36]. More quantum approaches treat the nuclear spin quantum mechanically and take into account the quantum back action of the NV center on the nuclear spin. Quantum back-action refers to the fact that the dynamics of the nuclear spin are conditioned on the state of the sensor. The NV is not just a passive observer of the environment but actively affects it. In fact, quantum back-action causes the nuclear spin target to become entangled with the NV and dips in sensor coherence appear as the dynamical decoupling drives entanglement between the sensor and the nuclear target. There have been several quantum approaches including geometric methods [2, 3] and more recently methods based on the Magnus expansion [37, 38] and the rotating wave approximation [39]. Quantum approaches are essential if one seeks to understand the dynamics of the nuclear spin target, not only the sensor response, as is the case for quantum information protocols where the NV is used to drive quantum operations on nuclear spin registers.

We are motivated to explore a Floquet theory approach by the periodicity of many dynamical decoupling schemes (which typically define a basic pulse unit and then apply it repeatedly). Floquet theory is generally applicable to systems with periodic Hamiltonians [40] and has seen some application in standard NMR [41] but was not yet introduced to the nanoscale NMR field. This is a quantum method that seeks to obtain the Floquet quasienergies and modes of the system which are the eigenenergies and eigenstates of the stroboscopic evolution. As the experiments are only ever measured stroboscopically the sensor response can be expressed completely in terms of the Floquet quasienergies and modes.

Later, we are motivated to apply our Floquet model to dynamical decoupling based sensing experiments where the short duration of microwave π-pulses can no longer be ignored. These experiments are typically modelled assuming that the π-pulses are instantaneous - taking infinitesimal time. However, it was recently pointed out that the unavoidable finite duration of microwave pulses can cause new signals, so-called *spurious* dips, to appear in sensor coherence traces [42]. This issue is particularly important as the arrival of these new signals can create ambiguities in nuclear spin species classification. This phenomenon was modelled with a semi-classical analysis [42, 43, 44] which was used to propose a method for determining whether a signal is spurious or not. We apply our

quantum approach, Floquet theory, which generalises to the finite-duration-pulse case, and seek to predict the complete sensor response under any finite duration pulse control. With a new understanding of the system dynamics in the presence of finite pulse durations we are able to propose a new set of protocols for enhancing sensing schemes - by removing ambiguities or increasing resolution.

Finally, as real experiments include errors, many studies [45, 46, 47, 39, 48] have been performed to analyse the performance of different pulse sequences in the presences of certain pulse errors - e.g. detunings from resonance, pulse phase errors, pulse flip-angle errors. An interesting class of problems is the effect of detuning errors. Instantaneous pulses completely refocus the effect of static fields essentially removing all detuning effects. However, in the presence of finite duration pulses this is no longer the case. We are motivated to study the interplay between detuning errors and finite duration pulses as this effect vanishes in the limit of zero width pulses and thus cannot be captured by any model that doesn't include finite pulse widths.

1.2 Outcomes

The work presented in this thesis has been published in Jacob Lang et. al., *"Dynamical-Decoupling-Based Quantum Sensing: Floquet Spectroscopy"*, Physical Review X (2015) [49] and Jacob Lang et. al., *"Enhanced Resolution in Nanoscale NMR via Quantum Sensing with Pulses of Finite Duration"*, Physical Review Applied (2017) [50]. It also includes work from two manuscripts currently in preparation: Jacob Lang et. al., *"Universal method for mitigating spurious signals via randomisation of pulse phases"* and Jacob Lang et. al., *"The non-vanishing effect of detuning errors in dynamical decoupling based sensing experiments"*.

The key outcomes of our work are fourfold. Firstly, we apply for the first time, Floquet analysis to model dynamical decoupling based sensing experiments [49, 50]. We find that avoided crossings in an underlying spectrum of Floquet quasienergies herald the appearance of characteristic dips in sensor coherence traces. The contrast and position of these dips being determined by the position and width of the avoided crossings. We express the coherence response in terms of the Floquet quasienergies and modes. This outcome is evidenced across Chapter 3 and Chapter 4. Secondly, we include finite pulse durations in our model to accurately predict the position and shape of spurious dips [50]. More generally, we can predict the finite-duration-pulse effect on the complete coherence response. This outcome is shown in Chapter 4. Thirdly, this new understanding of the finite-pulse

effect allows us to design new protocols for enhanced sensing either via increased spectral resolution or by suppressing the spurious signals. These protocols are given in Chapter 5. Finally, and more recently, we have developed an analytic model to understand the effect of detuning errors in the presence of finite pulse durations. As expected we see that these detuning error effects vanish if the pulse width is assumed to be infinitesimal. This outcome is presented in Chapter 6.

Our first result shows that Floquet theory can be usefully applied to dynamical decoupling based sensing experiments. We derive a general expression, Eq. (3.7), for the sensor coherence response in terms of the Floquet quasienergies and modes. Characteristic dips in sensor coherence are associated with avoided crossings in the Floquet quasienergy spectra with the avoided crossing width determining the shape of the coherence dip. We consider single spin-1/2 detection using CPMG control and explicitly obtain the Floquet quasienergies and modes by constructing the one-period evolution operator and diagonalising it, Eqs. (3.20),(3.21),(3.22). The link between avoided crossing width and dip shape is evidenced in Eqs. (3.25),(3.27). We model the NV detection of single ^{13}C nuclear spins and a possible future detector, a bismuth donor is silicon, detecting ^{29}Si dimers and trimers.

To model finite pulse durations we use a different approach to obtain the Floquet quasienergies and modes. In this case it is inefficient to construct the one-period evolution operator directly. Instead we construct the Floquet Hamiltonian, an infinite dimensional Hamiltonian in Floquet space, from which we can read out an effective Hamiltonian governing the stroboscopic dynamics. The eigenvalues and eigenstates of this effective Hamiltonian *are* the Floquet quasienergies and modes. We derive the first analytic expression that accurately models the spurious coherence dips, Eq. (4.23). The arrival of spurious dips due to the finite pulse durations is understood as the opening of new avoided crossings in the Floquet spectrum. We see that at expected DD signals the sensor states are dephased whilst at spurious dips the sensor states are directly mixed. This allows us to propose a simple test to characterise the nature of coherence dips. We analyse the dependence of the finite pulse effect on the pulse *shape*. Key to our analysis is the derivation of generalised modulation functions, Eqs. (4.8), (4.9), (4.10), which exist in the toggling frame (the frame rotating under the pulse Hamiltonian). These modulation functions generalise the single step-modulation function used in many semi-classical *and* quantum analyses [35, 1, 36, 37, 38, 39]. The generalised modulation functions allow us to derive a static effective Hamiltonian that approximates the system dynamics at stroboscopic times,

Eq. (4.16), for any finite-duration-pulse control.

We then propose new protocols for enhanced sensing. By adding a global phase to all pulses in the sequence the contrast of the spurious dips can be controlled [43]. With our model we are able to prescribe the exact global phase required to selectively suppress or augment spurious dips. This is useful for removing ambiguities in spin species classification or using the spurious signals for enhanced resolution (they are naturally much sharper than the expected DD signal.) In Table 5.1 we prescribe the global phase required to selectively remove spurious coherence dips under XY8 control. In Fig. 5.1 we demonstrate how the natural sharpness of spurious dips can be used to obtain increased resolution - exploiting a feature (previously considered as an error) as a resource. We also propose a scheme of randomising the global phase between sequence repetitions. We show, in Fig. 5.4, that this scheme can universally suppress the spurious dips (rather than selectively) and is universally applicable (to any pulse sequence). We also address the recently proposed YY8 sequence [44] which was designed to be robust against finite-duration-pulse effects. Where the analysis presented in [44] was semi-classical, we apply our quantum model to show how the sequence prevents spurious signals from appearing. We also point out that the sequence can still produce spurious dips when microwave detuning errors are present but show that our randomised DD protocol is also effective in this case.

Finally, to model the effect of detuning errors in finite duration pulse experiments we move away from our Floquet analysis. Whilst we consider a *static* detuning, meaning that the Hamiltonian shares the same periodicity as before, it is useful to work in the toggling frame. We see that in this frame the Hamiltonian can lose its periodicity so, instead of applying Floquet theory, we augment an analysis based on the Magnus expansion [37, 38] by including the generalised modulation functions. We derive a static effective Hamiltonian that approximates the dynamics under any pulse sequence including detunings, Eq. (6.9). We are able to express the sensor coherence response in terms of the Fourier transforms of these modulation functions and observing the detuning effect on these modulation functions reveals how detunings affect the coherence response. Our analytic expression shows a good fit to numerics. We specifically model two important detuning effects: the increasing contrast of XY8 spurious dips and, more strikingly, the splitting of the CPMG expected dip due to detunings. These effects are understood by looking at the spectrum of the modulation functions, Figs. 6.4, 6.5. Importantly, we show that due to the finite duration of pulses the coherence signal can be significantly suppressed by inhomogeneous broadening

(the dephasing by a spin bath that is usually considered to be completely removed by dynamical decoupling).

Alongside the work described in this thesis I have also contributed ideas, relating to dynamical decoupling, to two papers based in optomechanics [51, 52]. In the heterodyne optical detection scheme, the optical cavity output signal is amplified with a reference laser oscillating at a different frequency. The beating between the two frequencies averages out quantum correlations carried by the signal. We imported the idea of dynamical decoupling as a filter of noise by introducing a filter function in the data processing of heterodyne experiments to recover the lost correlations.

1.3 Magnetic Resonance Detection

NMR [53] and MRI [54], whilst both powerful tools for structure determination and non-invasive imaging, are limited in their sensitivity and resolution by two factors. The first is that they detect the magnetic resonance of samples via an inductive coil and constraints on the physical size of this coil limit the spatial resolution of the sensor. The second factor is that both schemes detect the net magnetisation of the sample (or a voxel in the sample). Producing a magnetic field detectable by the inductive coil relies on sampling Avogadro's numbers of spins to counter the vanishingly small net polarisation (typically only a few spins per million). Thus for any sample or voxel too small there are not enough spins to generate a strong enough signal and this limits the sensitivity and spatial resolution. Advances in magnetic resonance detection rely on replacing the inductive coil with more sensitive detectors.

Magnetic resonance force microscopy (MRFM) increases the sensitivity of magnetic imaging by replacing the inductive coil with a cantilever, akin to atomic force microscopy. MRFM sensitivity vastly outperforms MRI and NMR and the detection of single electron spins [55] and nanoscale ensembles of nuclear spins [56, 57] has been demonstrated. However, MRFM is operated at cryogenic temperatures and in vacuum which removes the bio-compatibility that benefit MRI methods. Superconducting quantum interference devices (SQUIDs) also offer excellent sensitivity and nanoSQUIDS have been developed for nanoscale application but these must also be run cryogenically [58, 59]. Atomic vapour detectors offer a return to ambient detection and many life-sciences applications whilst still being capable of detecting very weak magnetic fields [60]. However, their physical size hinders them from use in nanoscale applications.

The nitrogen vacancy center offers a naturally nanoscale magnetic sensor with unparalleled sensitivity that can be operated in ambient conditions. A good review of current magnetic resonance detection methods and how they compare to the nitrogen vacancy center can be found in [61].

1.4 Nitrogen Vacancy Center Experiments

There are hundreds of known defects in diamond [62]. These defects are known as colour centers as they are responsible for the wide range of colours that diamonds can have - whilst a completely pure ^{12}C diamond is transparent. The nitrogen vacancy center, a substitutional nitrogen neighbouring a vacant site, fluoresces red light. Finding natural diamonds with the desired defect concentrations would be a hard (and expensive) task but artificial diamonds can be made through high pressure and high temperature (HPHT) [63] and chemical vapour deposition (CVD) [64] techniques. Nitrogen vacancy centers can be implanted into artificial diamonds during the CVD process [8] and more recently with laser writing methods [65]. With the aid of confocal microscopy it is possible to address single nitrogen vacancy centers [66] in diamond for their application in quantum sensing and other quantum technologies.

The nitrogen vacancy center has a spin-1 ground state, with a large zero field splitting, that can be initialised and read out optically and can be manipulated with microwave pulses providing optically detected magnetic resonance (ODMR) [66]. The NV has a weak spin-orbit coupling resulting in long coherence times, even at room temperature [67], as the quantum state is well isolated from perturbations in the crystal lattice. The combination of optical and microwave manipulation and the functionality at room temperature has contributed to the wealth of NV based experiments over the past two decades. One challenge with the NV center is the limited quality of the optical spectrum, where the zero phonon line is dominated by a large phonon sideband. This affects the detection efficiency and interfacing with photons for quantum information purposes [9], however this can be improved with single shot readout [29, 68, 34], by working at cryogenic temperatures [68] or coupling to optical cavities [69] and new defect centers with superior optical properties are also being explored, see Sec. 1.5. The dominant source of decoherence for the NV center is a large bath of nuclear spins in the host diamond. Coherence times can be extended by isotopic purification of the diamond [67] or with dynamical decoupling [70, 71, 46] and coherence times of up to one second have been reported [72, 73].

The NV center is a sensitive probe of its nanoscale environment making it a versatile quantum sensing platform. It is sensitive to magnetic fields [74, 75] via its spin magnetic moment and electric fields via the Stark shift in the spin levels [76, 77, 78]. It can detect local temperatures via strain induced effects on the zero field splitting [79, 80, 81] and is also sensitive to rotations for sensitive gyroscopy [82, 83, 84] and pressure [85].

The ambient functionality of the NV center creates many opportunities for application in the life-sciences [12]. So far NV centers have been used to image live magnetotactic bacteria [86] and magnetic biomarkers inside living cells [87]. Nanodiamonds hosting NVs have been inserted into cells as fluorescent biomarkers [88] and to perform thermometry of the conditions inside human cells [89]. Applications in neuroscience include imaging the action potentials of single neurons [90] which is even possible from the outside of the live animal [91].

The NV center's sensitivity to magnetic fields has been used for DC [5, 92] and AC sensing [74] and the latter forms the basis of nanoscale NMR - detecting the oscillating magnetic fields produced by nuclear spins. Dynamical decoupling is used to amplify the weak signal from remote nuclear spins and different DD sequences have been designed to increase resolution [39, 93, 94, 95], determine correlations in the target [96] and protect against pulse errors [39, 48, 44].

Whilst NV dynamical decoupling based sensing offers vast improvements in sensitivity and spatial resolution over NMR and MRI the frequency resolution is limited. This is because the signal can only be interrogated during the the finite coherence time of the quantum sensor and this places a limit on the frequency resolution (the ability to distinguish two signals close in frequency). This prevents the sensor from resolving the frequency shifts due to intermolecular couplings, such as are regularly seen in standard NMR. This limit has been overcome with correlation spectroscopy techniques [97], by utilising ancillary qubits (e.g the substitutional nitrogen atom) as a quantum memory [98, 32] and by using a classical clock to combine information from sequential measurements [99, 100]. These more complex protocols are, however, still based on dynamical decoupling based sensing - the focus of this thesis.

Not all applications make use of single NV centers in bulk diamond. Experiments with ensembles of, instead of single, NV centers can increase sensitivities by a factor $\sqrt{N_{NV}}$ where N_{NV} is the number of NVs [101, 102]. However, this typically sacrifices the nanoscale spatial resolution of the single sensor. Nanodiamonds hosting NV centers have been used

in bio-science applications [12] and have also been optically levitated to create hybrid quantum systems [103]. NV centers are used in several proposals to test fundamental physics, with levitated nanodiamonds being used to probe wavefunction collapse models [104] and quantum gravity [105] and NV centers in bulk diamond have already been used to demonstrate a loophole-free Bell test [106, 107].

Finally, other applications of the NV center outside of sensing have included quantum computing [14, 31, 30], room temperature masers [108] and dynamical nuclear polarisation [109, 110, 111, 112, 113].

1.5 Other Solid State Defect Centers

The success of the NV center has spurred on the search to find other defect centers with similar properties (as well as hybridising the NV sensor [114, 115]). In diamond, the silicon vacancy center has been explored [9] and has been shown to have superior optical properties compared to the NV which is useful for interfacing photonic and spin systems. Germanium and tin vacancies in diamond have also been studied [116, 117, 118, 119] as have defects in silicon carbide which show similar properties to diamond defects [120, 10, 121].

Group V donors in silicon have recently gained much attention due to their extremely long coherence times [122, 123]. The large hyperfine coupling means there is strong mixing of the sensor Zeeman states at moderate magnetic fields [124, 125, 126] and for sensing this means the coherence function is strongly dependent on magnetic field which offers a new system control. Addressing single donors in silicon has recently been demonstrated [11, 127, 128, 129]. Silicon platforms offer simple interfacing with current silicon based technologies but must be run at cryogenic temperatures to localise the donor electron wavefunction.

1.6 Reviews

There are several instructive reviews on the field of NV based sensing which we list here. Specifically regarding NV based magnetometry there are [61, 130, 131, 132] whilst the intrinsic properties of the NV center are covered here [8, 133]. NV based sensing applications in the life sciences are discussed here [12] and a good review of quantum sensing more generally is given here [134].

1.7 Outline of Thesis

In Chapter 2 we cover the relevant theoretical background that the work of this thesis is based upon. In Chapter 3 we discuss the application of Floquet theory to dynamical decoupling based sensing (published in [49]). In Chapter 4 we analyse the effect of finite pulse durations in dynamical decoupling based sensing and in Chapter 5 propose new protocols for enhanced sensing (both containing work published in [50] and some work currently being prepared for submission). In Chapter 6 we study the interplay between finite-duration-pulse effects and microwave detuning errors (currently being prepared for a separate submission). Finally, we conclude.

2 | Background Material

The purpose of the chapter is to provide the relevant background upon which the original work in this thesis will be built. We start by describing spin dynamics in general and discuss the transformation to a rotating frame which is utilised often in this work. Next we present the nitrogen vacancy (NV) center - detailing the internal dynamics, initialisation and readout, state manipulation and coupling to other spins. We then outline the different protocols used in dynamical decoupling experiments by first discussing free induction decay and the Hahn echo. We discuss typical results from these experiments and present available semi-classical and quantum models. The final section introduces Floquet theory as a general mathematical tool so that it can be applied in the coming chapters.

The vast majority of defect based quantum sensing experiments have used the nitrogen vacancy center so, with one exception, the discussion in this thesis will describe experiments in this context (for consistency and to reflect the wealth of experimental work that has used the NV center). As efforts are made to expand the range of available solid state defect centers for quantum sensing we point out that the analysis here is easily applicable to other systems.

2.1 Spin Dynamics

The dynamics of an ensemble of magnetic spins is governed by the Schrödinger equation,

$$i\frac{\partial}{\partial t}\left|\psi(t)\right\rangle = \frac{\hat{H}(t)}{\hbar}\left|\psi(t)\right\rangle, \tag{2.1}$$

where $\hat{H}(t)$ is the Hermitian Hamiltonian operator. Hamiltonians in this work will be presented in angular frequency units so that from this point we will write $\hat{H}(t)/\hbar \equiv \hat{H}(t)$. The formal solution to Schrödinger's equation is provided by the evolution operator $\hat{U}(t) = \hat{\mathcal{T}}\exp(-i\int_0^t \hat{H}(s)ds)$ which gives the evolution of any initial state $\left|\psi(t)\right\rangle = \hat{U}(t)\left|\psi(0)\right\rangle$. This solution is often hard to evaluate however due to $\hat{\mathcal{T}}$, the time-ordering operator and

because the Hamiltonian may not commute with itself at different times, $[\hat{H}(t_1), \hat{H}(t_2)] \neq 0$. For time-independent Hamiltonians the solution is obtained simply, $\hat{U}(t) = \exp(-i\hat{H}t)$ and only requires the diagonalisation of the Hamiltonian. The expectation value of a measurement, $\hat{O}$, is given by $\langle\hat{O}\rangle = \langle\psi(t)|\hat{O}|\psi(t)\rangle$.

If the initial state of the system is not exactly known (a pure state) but is selected from an ensemble of possible states (a mixed state) then the state can be represented by a density matrix $\rho(t) = \hat{U}(t)\rho_0\hat{U}^\dagger(t)$ which evolves from the initial density matrix. The initial density matrix, $\rho_0 = \sum_j p_j|\psi_j(0)\rangle\langle\psi_j(0)|$, describes the possible pure states that the system could start in, $|\psi_j(0)\rangle$ and their relative probabilities p_j. For density matrices the expectation value of measurements is given by $\langle\hat{O}\rangle = \mathrm{Tr}\{\hat{O}\rho(t)\}$.

The spin dynamics under a general 2-D spin Hamiltonian are discussed in App. A.

2.1.1 Rotating Frames

It will often be useful to move to a rotating frame where the Schrödinger equation is easier to solve. The switch to a rotating frame is usually performed with respect to a static reference Hamiltonian however this need not be the case and in App. B we derive the general case. The transform of a Hamiltonian, $\hat{H}(t)$, to a frame rotating under a reference Hamiltonian, $\hat{H}_\mathrm{r}(t)$, is given by

$$\hat{H}(t) \rightarrow \hat{H}'(t) = \hat{U}_\mathrm{r}^\dagger(t)[\hat{H}(t) - \hat{H}_\mathrm{r}(t)]\hat{U}_\mathrm{r}(t) \tag{2.2}$$

where $\hat{U}_\mathrm{r}(t) = \hat{\mathcal{T}}\exp(-i\int_0^t \hat{H}_\mathrm{r}(s)ds)$ is the reference evolution operator. This is valid for time-dependent and time-independent Hamiltonians and reference Hamiltonians and we will utilise this often in this work. If the dynamics of the system can be found in the rotating frame, $|\psi'(t)\rangle$, then the transformed state is related to the original state via $|\psi(t)\rangle = \hat{U}_\mathrm{r}(t)\,|\psi'(t)\rangle$.

As an example consider a static Hamiltonian subject to some time-dependent control, $\hat{H}(t) = \hat{H}_0 + \hat{H}_\mathrm{c}(t)$. In the original frame the solution to the Schrödinger equation, $|\psi(t)\rangle$, may be hard to obtain. We can move to the frame rotating under $\hat{H}_\mathrm{c}(t)$ to obtain a new Hamiltonian, $\hat{H}'(t) = \hat{U}_\mathrm{c}^\dagger(t)[\hat{H}(t) - \hat{H}_\mathrm{c}(t)]\hat{U}_\mathrm{c}(t) = \hat{U}_\mathrm{c}^\dagger(t)\hat{H}_0\hat{U}_\mathrm{c}(t)$. If the Schrödinger equation in this frame is easier to solve we can obtain $|\psi'(t)\rangle$ and then the solution in the original frame is given by $|\psi(t)\rangle = \hat{U}_\mathrm{c}(t)\,|\psi'(t)\rangle$.

2.1.2 The Rotating Wave Approximation

The rotating wave approximation (RWA) is useful when considering the response of a spin system to resonant magnetic fields. In the frame rotating with the frequency of the resonant field there is a residual rapidly oscillating term that is ignored - this is the RWA. As an example consider an oscillating magnetic field incident on a spin qubit,

$$\hat{H}(t) = \frac{\omega_0}{2}\hat{\sigma}_z + \Omega(t)\cos(\omega_{\rm d}t)\hat{\sigma}_x, \tag{2.3}$$

where ω_0 is the qubit energy splitting, $\omega_{\rm d} = \omega_0 - \Delta$ is the drive frequency which misses the resonant frequency by some detuning Δ and $\Omega(t)$ is the strength of the oscillating field. In the frame rotating under the reference Hamiltonian $\hat{H}_{\rm r} = \frac{\omega_{\rm d}}{2}\hat{\sigma}_z$ the transformed Hamiltonian is

$$\hat{H}'(t) = \frac{\Delta}{2}\hat{\sigma}_z + \frac{\Omega(t)}{2}\hat{\sigma}_x + \frac{\Omega(t)}{2}(\cos(2\omega_{\rm d}t)\hat{\sigma}_x - \sin(2\omega_{\rm d}t)\hat{\sigma}_y), \tag{2.4}$$

$$\approx \frac{\Delta}{2}\hat{\sigma}_z + \frac{\Omega(t)}{2}\hat{\sigma}_x. \tag{2.5}$$

where the RWA is made in the second line. If the detuning is zero then the spin state is rotated about the x-axis by an angle $\int_0^t \Omega(s)ds$. The example here describes an oscillating field that is linearly polarised along the x-axis but the polarisation could be along any axis in the xy-plane generating a whole class of possible spin rotations. If Δ is small compared to $\Omega(t)$ then it slightly perturbs the spin rotation. If $\Delta \gg \Omega(t)$ then the spin state is not affected by the oscillating field. This is useful for isolating two levels out of a large state space. For instance, the 3 levels of the spin-1 NV center are reduced to a spin qubit by applying microwave control only resonant with a single transition.

Hamiltonians in this work will often include microwave control and we present them in the frame rotating with the microwave frequency and make the rotating wave approximation.

2.2 The Nitrogen Vacancy Center in Diamond

The nitrogen vacancy (NV) center in diamond is a point defect that consists of a substitutional nitrogen atom and neighbouring vacant site replacing two carbon atoms in the diamond lattice, Fig. 2.1(a). The defect site then has an electronic structure (formed by the spare electrons from the atoms neighbouring the vacancy) and functions like a single, isol-

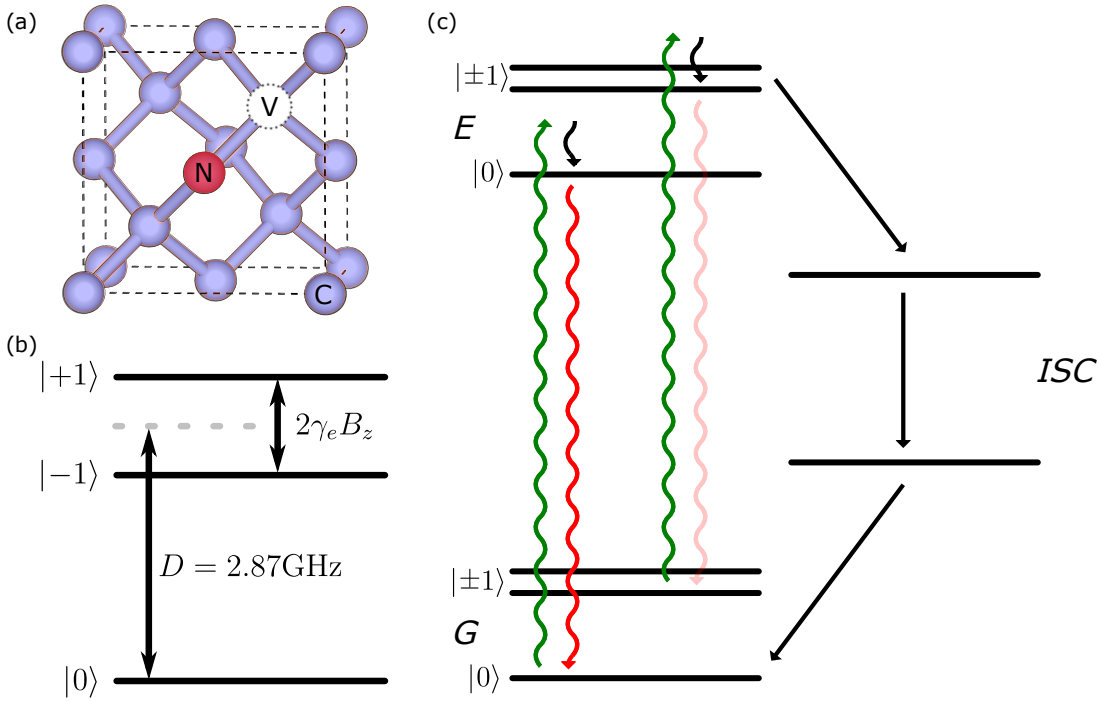

Figure 2.1: (a) The nitrogen vacancy center in diamond is a substitutional nitrogen next to a vacant site. (b) The electronic ground state is a spin-1 system with zero-field splitting D and the $m_s = \pm 1$ levels are split by an applied magnetic field. (c) The larger electronic structure of the NV. The excited state is also spin-1 and there is an inter-system crossing (ISC). Green laser light excites from ground to excited states in a spin preserving transition. The excited state can decay again via the spin-preserving transition fluorescing red light but the $m_s = \pm 1$ levels preferentially decay through the non-radiative ISC to the $m_s = 0$ state. This allows for readout and initialisation.

ated atom locked into the diamond. The defect electronic state is then neutral, NV^0, unless it captures a free electron from the environment making it negatively charged, NV^-. In magnetometry applications only the negatively charged state is used as it has the required optical and spin properties [131, 8] and we refer to it simply as the NV.

2.2.1 The NV Center Ground State Hamiltonian

The NV ground state is a spin-1 system with a large zero-field splitting, $D = 2.87$ GHz$\times 2\pi$, along the crystal axis which runs between the nitrogen and the vacancy. A strain-induced, off-axis zero-field splitting, E, is also present but can typically be ignored as it is several orders of magnitude smaller than the on-axis splitting ($\sim$ kHz $\rightarrow$ MHz) [131]. When an external magnetic field, $\mathbf{B}$, is applied the NV ground state Hamiltonian is

$$\hat{H}_{\mathrm{NV}} = D\hat{S}_z^2 + E(\hat{S}_x^2 - \hat{S}_y^2) - \gamma_{\mathrm{e}}\mathbf{B}\cdot\hat{\mathbf{S}}, \tag{2.6}$$

where $\gamma_e = -28.025$ GHz/T $\times 2\pi$ is the electronic gyromagnetic ratio [135] and $\hat{\mathbf{S}} = (\hat{S}_x, \hat{S}_y, \hat{S}_z)$ is the NV spin operator. Here, the NV spin operators are

$$\hat{S}_x = \frac{1}{\sqrt{2}} \begin{pmatrix} 0 & 1 & 0 \\ 1 & 0 & 1 \\ 0 & 1 & 0 \end{pmatrix}, \hat{S}_y = \frac{1}{\sqrt{2}} \begin{pmatrix} 0 & -i & 0 \\ i & 0 & -i \\ 0 & i & 0 \end{pmatrix}, \hat{S}_z = \begin{pmatrix} 1 & 0 & 0 \\ 0 & 0 & 0 \\ 0 & 0 & -1 \end{pmatrix} \tag{2.7}$$

but these will be reduced to spin-1/2 operators when microwave control pulses are applied resonantly with only one of the NV transitions. The zero-field splitting separates the $m_s = 0$ from the $m_s = \pm 1$ states and a magnetic field $\mathbf{B} = B_z\mathbf{z}$ aligned with the NV axis will split the $m_s = \pm 1$ states by $2\gamma_e B_z$ as shown in Fig. 2.1(b). Due to the large zero-field splitting, off-diagonal terms $(\hat{S}_x, \hat{S}_y)$ in the Hamiltonian can typically be neglected (as they are too weak to flip the NV spin over the large energy gap). When only $\hat{S}_z$ terms are retained the Hamiltonian is called *pure-dephasing* as it does not mix the NV center states. Due to the lattice structure of diamond the NV can exist in 4 possible orientations. In this thesis we consider experiments using single NVs so once the crystal axis is identified the relative orientation is not important.

2.2.2 Readout and Initialisation

Single NV centers can be optically addressed using confocal microscopy and fluoresce red (637 nm) when irradiated with green (532 nm) laser light. The strength of the fluorescence is coupled to the projection of the NV spin along the crystal axis enabling state readout. This optically detected magnetic resonance (ODMR) is the window into the nanoscale environment of the nitrogen vacancy center [4].

Under 532 nm laser illumination, the NV center is excited via a spin-preserving transition to an excited state. The NV can then decay through two channels as seen in Fig 2.1(c), directly back to the ground state in a spin-preserving radiative transition that causes the NV to fluoresce with red light (637 nm), or through a singlet state inter-system crossing (ISC) that is non-radiative and only decays to the $m_s = 0$ state. The structure of the inter-system crossing is the cause of some debate [136, 133, 131], with different sources reporting it to be made up of one, two or three singlet states. Importantly, however, the inter-system crossing does not fluoresce and it is not spin-preserving.

The $m_s = 0$ state preferentially decays through the radiative transition, and is thus denoted the bright state, whilst the $m_s = \pm 1$ states preferentially decay through the non-

radiative ISC transition and are thus denoted as dark states. By measuring the fluorescence after laser illumination one can measure the population difference between the $m_s = 0$ and $m_s = \pm 1$ states. (Effectively a measurement of $\langle \hat{S}_z^2 \rangle$.) The fluorescence contrast between the bright and dark states is $\sim 20\%$ [131].

Additionally, the NV center can be initialised by illuminating with green light for an extended time so that the spin-state will be optically pumped into the $m_s = 0$ state.

2.2.3 Microwave Manipulation

For moderate magnetic fields the transition between the NV $m_s = 0$ and $m_s = \pm 1$ is a few gigahertz and can be addressed with resonant microwave driving. Rapid NV spin rotations can be achieved by applying pulses of resonant microwave radiation. The microwave frequency is chosen to match one of the NV transitions, $0 \leftrightarrow m_u = \pm 1$, so that $\omega_{\mathrm{MW}} = D + m_u |\gamma_{\mathrm{e}}| B_z - \Delta$, where Δ is some detuning error. Moving to the frame rotating under the reference Hamiltonian, $\hat{H}_{\mathrm{ref}} = m_u \omega_{\mathrm{MW}} \hat{S}_z$ and making the rotating wave approximation (ignoring fast rotating terms) one obtains a pulse Hamiltonian describing the microwave control of the resonant transition,

$$\hat{H}_p(t) = m_u \Delta \hat{S}_z + \left[\Omega_x(t) \hat{S}_x + \Omega_y(t) \hat{S}_y \right], \tag{2.8}$$

where $m_u = \pm 1$ depending on which transition is chosen and $\Omega_{x,y}(t)$ is the strength of the microwave drive along the x and y axes. The NV spin operators are now given by

$$\hat{S}_x = \frac{1}{2} \begin{pmatrix} 0 & 1 \\ 1 & 0 \end{pmatrix}, \hat{S}_y = \frac{1}{2} \begin{pmatrix} 0 & -i \\ i & 0 \end{pmatrix}, \hat{S}_z = \begin{pmatrix} 1 & 0 \\ 0 & 0 \end{pmatrix} \tag{2.9}$$

as the microwave radiation does not address the 3rd state. We consider microwave pulses that are linearly polarised but can be oriented at any phase, ϕ, in the xy-plane. Thus during a pulse the phase does not change: $\Omega_x(t) + i\Omega_y(t) \equiv \Omega(t) \exp(i\phi)$ and here $\Omega(t)$ describes the pulse shape. The pulse shape is often assumed to be a delta-spike which creates instantaneous pulses. In fact, the pulses have some finite duration and later we model them as square (top-hat) and also consider other shapes. A pulse is defined by its phase ϕ and its shape $\Omega(t)$ which is zero outside some width $t = [-t_p/2, +t_p/2]$. The pulse rotates the state by an angle $\theta = \int_{-t_p/2}^{t_p/2} \Omega(t) dt$ about an axis, specified by the phase, in the xy-plane.

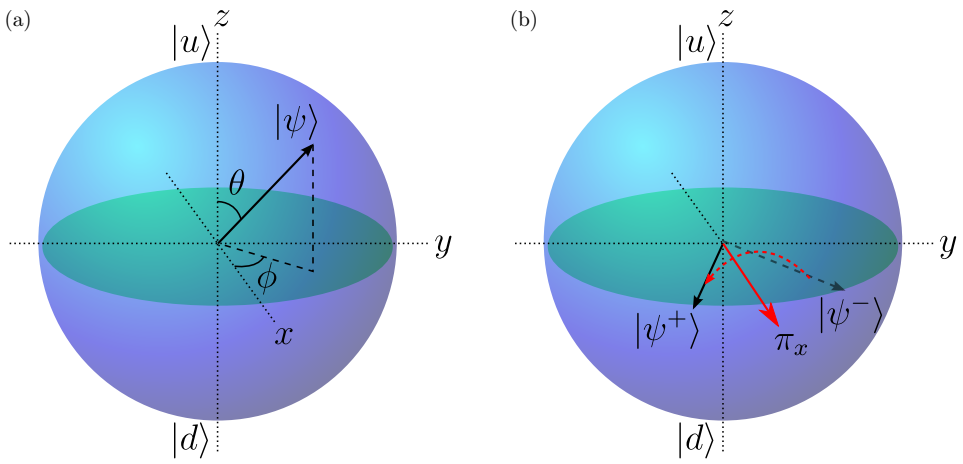

Figure 2.2: (a) Bloch sphere representation of the qubit sensor state. The state $|\psi\rangle = \cos\frac{\theta}{2}|u\rangle + \sin\frac{\theta}{2}\exp(i\phi)|d\rangle$ can be represented as a vector $\sin\theta\cos\phi\hat{\mathbf{x}} + \sin\theta\sin\phi\hat{\mathbf{y}} + \cos\theta\hat{\mathbf{z}}$ on the Bloch sphere. (b) Microwave pulses can rotate the qubit state about any axis on the xy-plane by any angle. Here we illustrate a π-rotation about the x-axis denoted π_x. For sensing experiments a $\frac{\pi}{2}$-pulse is used to initialise the sensor from the state $|d\rangle$ to an equal superposition state.

Under microwave manipulation of a selected transition $m_s = 0 \leftrightarrow m_u = \pm 1$ the third state $m_s \neq m_u$ is strongly detuned and will not be affected by control pulses. Thus two states are isolated from the NV spin-1 levels resulting in a spin qubit with states $|u\rangle \equiv |m_u\rangle$ and $|d\rangle \equiv |0\rangle$. An arbitrary qubit state, $|\psi\rangle = \cos\frac{\theta}{2}|u\rangle + \sin\frac{\theta}{2}\exp(i\phi)|d\rangle$, can be represented on a Bloch sphere as seen in Fig. 2.2(a) and microwave pulses rotate the state about an axis on the xy-plane as seen in Fig. 2.2(b).

In NV based dynamical decoupling experiments a combination of optical initialisation to the $m_s = 0$ state and a microwave $\pi/2$-pulse is used to initialise the NV to an equal superposition state. In dynamical decoupling experiments the effect of a static detuning error is usually considered to be completely removed. However, in Chapter 6 we show that when the control pulses have finite duration the detuning error *can* have an effect.

The absorption and emission of a photon by the NV changes its spin by ± 1. The applied microwave radiation thus addresses the $m_s = -1 \leftrightarrow m_s = 0$ and $m_s = 0 \leftrightarrow m_s = +1$ transitions. When the $m_s = \pm 1$ energy levels are split (e.g. by an applied magnetic field) one of these transitions is chosen as the sensor qubit neglecting the third state as it is strongly detuned ($\Delta \gg \Omega(t)$). In Chapter 6 we discuss the effect of small detunings ($\Delta < \Omega(t)$).

2.2.4 The Host Nitrogen

The substitutional nitrogen also has a nuclear spin that couples to the NV electronic spin via the hyperfine interaction. The nitrogen can be a ^{14}N spin-1 isotope or a ^{15}N spin-1/2 isotope. The combined Hamiltonian is

$$\hat{H}_{\text{NV-N}} = \hat{H}_{\text{NV}} - \gamma_{\text{N}}\mathbf{B}\cdot\hat{\mathbf{I}}^{\text{N}} + Q(\hat{I}_z^{\text{N}})^2 + A_{\parallel}^{\text{N}}\hat{S}_z\hat{I}_z^{\text{N}} + A_{\perp}^{\text{N}}\left(\hat{S}_x\hat{I}_x^{\text{N}} + \hat{S}_y\hat{I}_y^{\text{N}}\right), \tag{2.10}$$

where γ_{N} is the nitrogen gyromagnetic ratio, Q is a zero-field splitting (only present for the ^{14}N), $A_{\parallel}^{\text{N}}$ and $A_{\perp}^{\text{N}}$ are the parallel and perpendicular components of the hyperfine coupling respectively and $\hat{\mathbf{I}}^{\text{N}} = (\hat{I}_x^{\text{N}}, \hat{I}_y^{\text{N}}, \hat{I}_z^{\text{N}})$ represents the nitrogen spin which are either spin-1/2 or spin-1 operators depending on the nitrogen isotope. Table. 2.1 lists the specific parameters for ^{14}N and ^{15}N [137].

Isotope	Spin	γ_{N} (MHz/T $\times 2\pi$)	Q (MHz $\times 2\pi$)	$A_{\parallel}^{\text{N}}$ (MHz $\times 2\pi$)	$A_{\perp}^{\text{N}}$ (MHz $\times 2\pi$)
^{14}N	1	3.077	-5.01	-2.14	-2.7
^{15}N	1/2	-4.316	0	3.03	3.65

Table 2.1: Physical parameters for the two possible host nitrogen isotopes.

Due to the large zero-field splitting we can make the pure-dephasing approximation and neglect $A_{\perp}^{\text{N}}$. If the applied magnetic field is also aligned with the NV axis then this removes any nitrogen spin mixing. Assuming the nitrogen initial state is the Zeeman state $|m_I\rangle$ then the NV only feels an additional static field along the crystal axis,

$$\hat{H}_{\text{NV-N}} = \hat{H}_{\text{NV}} + m_I A_{\parallel}^{\text{N}}\hat{S}_z. \tag{2.11}$$

In ideal dynamical decoupling experiments the effect of a static field is removed completely (detailed below) so the host nitrogen can often be neglected entirely. However, in Chapter 6 we show that static fields *can* have an appreciable effect in certain situations due to the finite duration of control pulses and we discuss the effect the host nitrogen can have on the NV in these cases.

2.2.5 Spin Bath Hamiltonian

Due to the weak spin-orbit coupling the dominant decoherence source for the NV center is not lattice phonons but a large fluctuating spin bath, illustrated in Fig. 2.3. Most of the diamond carbon atoms, ^{12}C, have zero spin but a natural abundance (1.1%) of ^{13}C causes the nitrogen vacancy to dephase. The NV center couples to nuclear spins in the

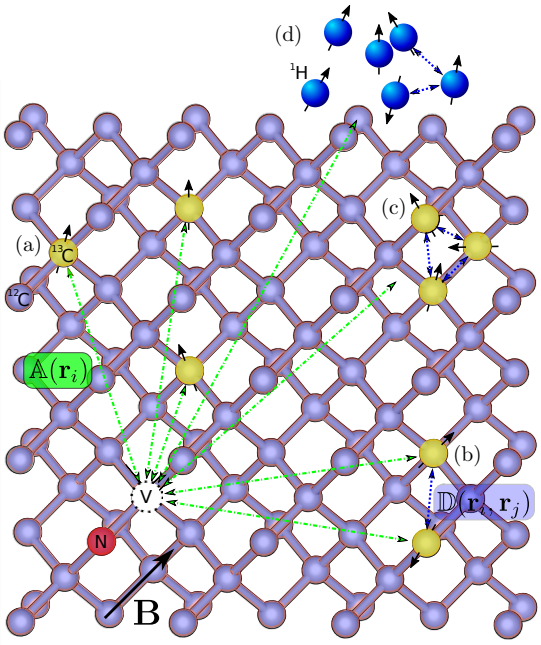

Figure 2.3: The local spin environment of the nitrogen vacancy center in diamond. The majority of lattice sites are zero-spin ^{12}C atoms but a natural abundance (1.1%) of ^{13}C have a nuclear spin-1/2. (a) The NV hyperfine couples to nuclear spins in the environment. (b) Nuclear spins in the environment couple together. (c) Many-body correlations may be present but the dominant effect on the NV is from the single-spin effect. (d) Ultimately the NV based sensor is designed to detect nuclear spins external to the diamond.

environment via the hyperfine interaction and the NV-bath Hamiltonian is

$$\hat{H}_{\text{NV-bath}} = \hat{H}_{\text{NV}} + \hat{H}_{\text{hyp}} + \hat{H}_{\text{bath}}. \tag{2.12}$$

The spin bath dynamics is governed by

$$\hat{H}_{\text{bath}} = -\sum_i \gamma_n^{(i)} \mathbf{B} \cdot \hat{\mathbf{I}}_i + \sum_{i,j} \hat{\mathbf{I}}_i^T \mathbb{D}_{i,j} \hat{\mathbf{I}}_j, \tag{2.13}$$

where $\gamma_n^{(i)}$ is the gyromagnetic ratio of the i-th nuclear spin represented by $\hat{\mathbf{I}}_i$, $\mathbf{B}$ is an applied magnetic field, $\mathbb{D}_{i,j}$ is the dipolar coupling tensor between spins and $\hat{\mathbf{I}}^T$ denotes the transpose of $\hat{\mathbf{I}}$. The first term is the Zeeman energy and the second term is the dipolar coupling between spins.

The hyperfine coupling is described by

$$\hat{H}_{\text{hyp}} = \sum_i \hat{\mathbf{S}}^T \mathbb{A}(\mathbf{r}_i) \hat{\mathbf{I}}_i, \tag{2.14}$$

where $\mathbb{A}(\mathbf{r}_i)$ is the hyperfine coupling tensor which depends on the position of the nuclear spin relative to the NV, $\mathbf{r}_i$. Making the pure-dephasing approximation (only retaining S_z

terms) we obtain

$$\hat{H}_{\text{hyp}} = \sum_i \hat{S}_z \mathbf{A}(\mathbf{r}_i) \cdot \hat{\mathbf{I}}_i, \tag{2.15}$$

where $\mathbf{A}(\mathbf{r}_i)$ is a hyperfine *field* felt by the i-th nuclei. The hyperfine field, in Cartesian and polar coordinates is given by:

$$\mathbf{A}(\mathbf{r}_i) = -\hbar \frac{\mu_0}{4\pi} \frac{\gamma_e \gamma_n}{r^3} \left(\frac{3r_z r_x}{r^2}, \frac{3r_z r_y}{r^2}, \frac{3r_z^2}{r^2} - 1 \right) \tag{2.16}$$

$$= -\hbar \frac{\mu_0}{4\pi} \frac{\gamma_e \gamma_n}{r^3} \left(\frac{3}{2} \sin 2\theta \cos\phi, \frac{3}{2} \sin 2\theta \sin\phi, 3\cos^2\theta - 1 \right), \tag{2.17}$$

where $\mathbf{r} = (r_x, r_y, r_z) = r(\sin\theta\cos\phi, \sin\theta\sin\phi, \cos\theta)$ is defined relative to the NV crystal axis. Figure 2.3 illustrates the typical spin environment of the NV center in spin sensing experiments. In nanoscale NMR and MRI experiments the goal is to identify single nuclear spins and spin clusters from this bath of nuclear spins.

2.3 Dynamical Decoupling Based Sensing Experiments

Dynamical decoupling (DD) is a method to *decouple* the state of the NV (or other qubit systems) from its environment by applying a train of π-pulses that repeatedly invert the state and *dynamically* average out any unwanted evolution due to the environment. These protocols can be best understood by first describing the free induction decay and Hahn echo experiments [138]. The protocols for all these experiments are also shown in Fig. 2.4.

For experiments with the NV center we assume that the $m_s = \pm 1$ states are split and one one of these states is selected (by resonant microwave control) as the *up* state of the sensor qubit. We denote $|d\rangle \equiv |m_s = 0\rangle$ and $|u\rangle \equiv |m_s = \pm 1\rangle$. In this section we consider a general sensor qubit.

Typically, the Hamiltonian is assumed to be *pure-dephasing*. That is to say, the Hamiltonian contains no terms that mix the u and d qubit states. This is justified in the case of NV sensing as the large zero-field splitting makes it hard for environment spins to flip the spin state of the NV. A general pure-dephasing Hamiltonian can be written as $\hat{H} = |u\rangle\langle u|\hat{H}_u + |d\rangle\langle d|\hat{H}_d$ where $\hat{H}_{u,d} = \langle u, d|\hat{H}|u, d\rangle$ is the environment Hamiltonian conditioned on the sensor spin state. This Hamiltonian encompasses the *quantum back-action* of the sensor on the environment. The sensor directly affects the evolution of the target instead of being a passive probe. In fact, for nuclear spin detection, the sensor becomes entangled with the nuclear spins and the experimental signal is a measure of this entangle-

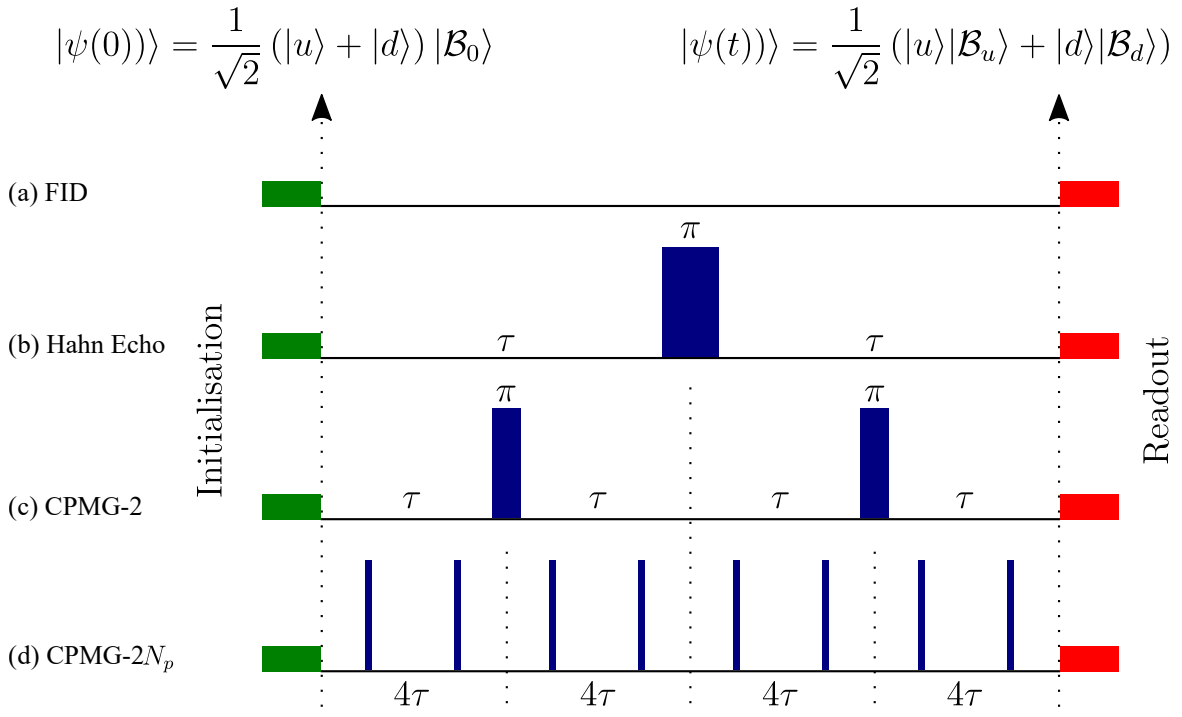

Figure 2.4: Dynamical decoupling based sensing protocols. All experiments begin by initialising the sensor to an equal superposition state and end by measuring the spin projection along the original superposition axis. The different protocols are composed of sections of free evolution interspersed with control π-pulses. Shown here are the (a) free induction decay (FID) (b) Hahn echo (HE) (c) CPMG-2 and (d) CPMG-2N_p experiments. Notice that the CPMG sequence is just two repetitions of the Hahn echo and the CPMG-2N_p sequence is N_p repetitions of the CPMG sequence.

ment. The evolution operator takes the form $\hat{U}(t) = \exp(-i\hat{H}t) = |u\rangle\langle u|\hat{U}_u(t) + |d\rangle\langle d|\hat{U}_d(t)$ where $\hat{U}_{u,d}(t) = \exp(-i\hat{H}_{u,d}t)$ so that if the sensor is in the u state then the environment evolves according to $\hat{U}_u$ and if the sensor is in the d state the environment evolves according to $\hat{U}_d$. In dynamical decoupling experiments we begin with the sensor in a superposition state and this bifurcates the evolution of the environment.

All dynamical decoupling based sensing experiments begin and end the same way, see Fig. 2.4. The qubit sensor is initialised to an equal superposition state,

$$|\psi_0\rangle = \frac{1}{\sqrt{2}}(|u\rangle + |d\rangle)\,|\mathcal{B}_0\rangle\,, \tag{2.18}$$

where $|\mathcal{B}_0\rangle$ is the initial state of the environment, selected from a thermal ensemble. It is possible to initialise the nuclear spin states but this requires prior knowledge of the nuclear spin coupling parameters and in the context of sensing we assume the nuclear spins are not initialised. For nuclear spin-1/2s the initial state can be $|\uparrow\rangle$ or $|\downarrow\rangle$ with probabilities determined by the Boltzmann distribution. At room-temperature the thermal energy vastly outweighs the nuclear Zeeman energy so the nuclear spin is said to be in a thermal state. That is to say, it is equally likely for the nuclear spin-1/2 to be in the $|\uparrow\rangle$ and $|\downarrow\rangle$ states. For low-temperature experiments the mixture of the initial nuclear state is not equal and this will affect the shape of the coherence dips. However, the theoretical analysis remains much the same as the system evolution operator is independent of the initial state. Experiments at low temperature will also typically have longer coherence times and are also capable of single shot readout (via resonant optical excitation [68]) although this is also possible at room temperature [29].

The spin state evolves under the particular experimental pulse sequence to

$$|\psi(t)\rangle = \frac{1}{\sqrt{2}}(|u\rangle\,|\mathcal{B}_u\rangle + |d\rangle\,|\mathcal{B}_d\rangle), \tag{2.19}$$

where $|\mathcal{B}_{u,d}\rangle = \hat{U}_{u,d}(t)\,|\mathcal{B}_0\rangle$.

The experiment then measures the state along the initial superposition axis to obtain $\mathcal{L}(t) = \langle\hat{\sigma}_x\rangle$ and averages over many experimental runs to achieve an adequate signal to noise ratio. In NV center experiments, $\langle\hat{\sigma}_x\rangle$ cannot be measured directly as the optical readout only measures a population difference between the $m_s = 0$ and $m_s = \pm 1$ levels. However, applying a $\pi/2$-pulse before a measurement of $\langle\hat{\sigma}_z\rangle$ is equivalent to measuring $\langle\hat{\sigma}_x\rangle$. The experimental data then reports a value between ± 1 depending on how much the

evolution has perturbed the initial state of the sensor.

2.3.1 Free Induction Decay

In a free induction decay experiment there are no control pulses between initialisation and readout and the system is left to evolve freely, Fig. 2.4(a). As the sensor is coupled to a noise bath (of nuclear spins) the sensor *dephases*, losing the initial phase information of the superposition state. This process is called decoherence and the quantity $\mathcal{L}(t)$ is called the sensor coherence. Specifically, this is T_2^* decoherence caused by *inhomogeneous broadening*.

Inhomogeneous broadening is caused by the nuclear spins in the bath starting each experimental run in some random configuration. This configuration of spins produces a quasi-static magnetic field that changes between each experimental run but can be considered static during each experimental run. Consider a sensor in a static magnetic field. The evolved state is $\frac{1}{\sqrt{2}}(|u\rangle \exp(-i\omega_u t) + |d\rangle \exp(-i\omega_d t))$ with some phase difference $(\omega_u - \omega_d)t$ determined by the strength of the magnetic field. When the experiment is repeated and the quasistatic field strength changes the signals are out of phase with each other and the averaged signal produces an exponential decay as seen in Figs. 2.5(a)(i) and (ii). The characteristic time scale for this decay is T_2^*. The dephasing effect of inhomogeneous broadening can be completely removed by the Hahn echo (although in Chapter 6 we show that this is not always true).

2.3.2 Hahn Echo

Hahn echo experiments [138] proceed as follows (see Fig. 2.4(b)): The sensor is initialised into an equal superposition; the system is allowed to evolve for a time τ; a control π-pulse is applied to invert the u and d states; the system is allowed to evolve again for an equal time τ; the system is measured along the original superposition axis. In this case, the final state of the system (before measurement) can still be written in the form of Eq. (2.19) but now the bath states are given by $|\mathcal{B}_u(t=2\tau)\rangle = \hat{U}_u(\tau)\hat{U}_d(\tau)\,|\mathcal{B}_0\rangle$ and $|\mathcal{B}_d(t=2\tau)\rangle = \hat{U}_d(\tau)\hat{U}_u(\tau)\,|\mathcal{B}_0\rangle$ where we see that the evolution of the bath state has switched at time $t=\tau$ due to the quantum back-action of the sensor on the bath.

The Hahn echo completely cancels the effect of inhomogeneous broadening as it is insensitive to static fields. Consider the Hahn echo experiment in a static field. The final state will be $\frac{1}{\sqrt{2}}(|u\rangle \exp(-i\omega_u\tau)\exp(-i\omega_d\tau) + |d\rangle \exp(-i\omega_d\tau)\exp(-i\omega_u\tau)) \equiv \frac{1}{\sqrt{2}}(|u\rangle + |d\rangle)$, so the initial state is completely recovered. At the time $t=2\tau$ the dephased signals have

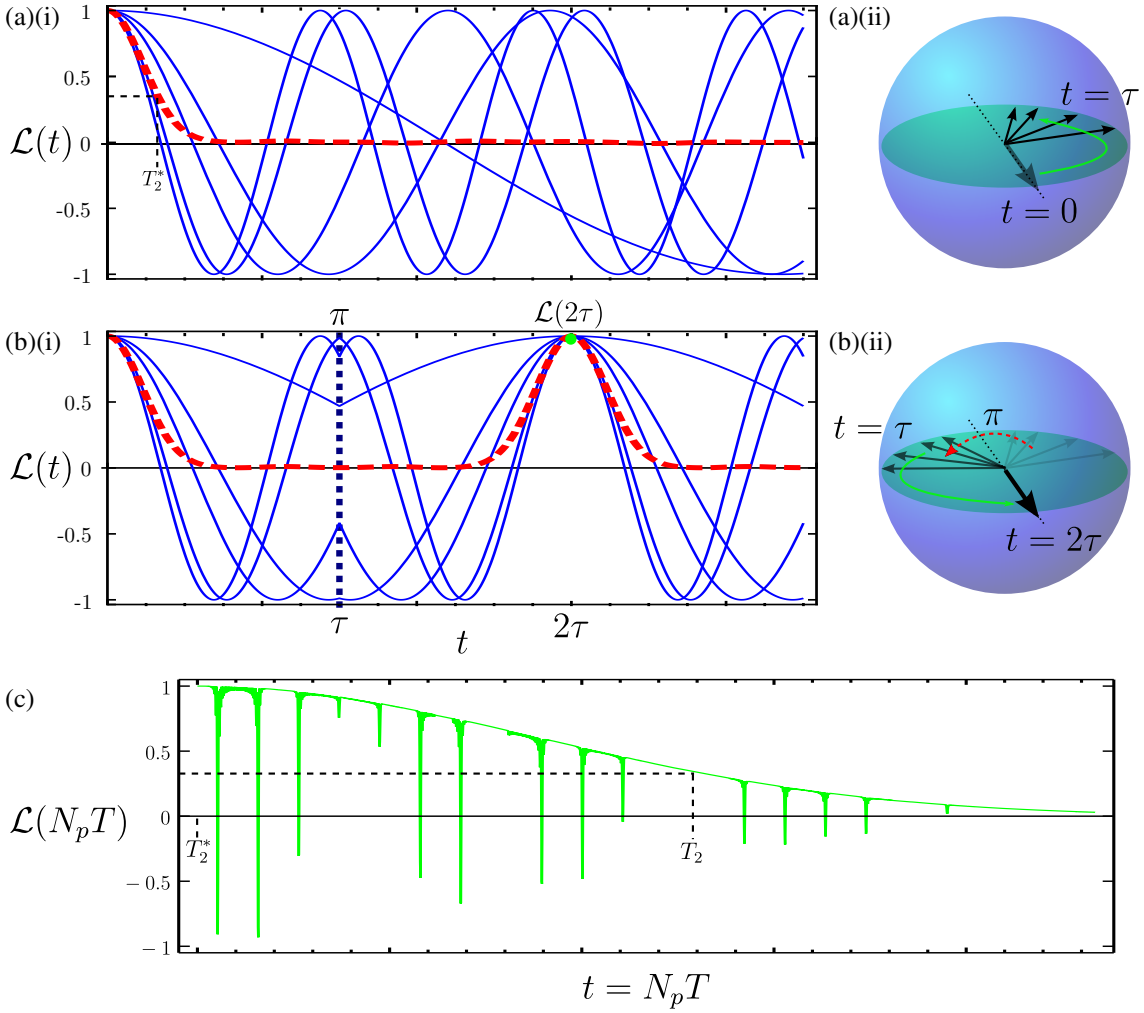

Figure 2.5: Dephasing and decoherence. (a)(i) shows the dephasing of a qubit sensor in an FID experiment. For each repetition of the experiment the quasistatic magnetic field the sensor feels from the environment is slightly different. The oscillating signals (blue lines) go out of phase with each other and under statistical averaging the signal decays (red dashed line) on a timescale T_2^*. The Bloch sphere representation of the dephasing state is shown in (a)(ii). (b)(i) shows the dephasing and subsequent refocussing of a qubit sensor in a Hahn echo experiment. The signal dephases as for the FID experiment but the π-pulse causes the dephasing to refocus at at time $t = 2\tau$. Stretching the delay, τ, the echo will survive until the coherence time $T_2 \gg T_2^*$. The Bloch sphere representation of the Hahn echo evolution is shown in (b)(ii). (c) shows the response under dynamical decoupling. Here the Hahn echo sequence is replaced by a basic pulse sequence of length T and is repeated N_p times. The length of the sequence is stretched to produce a coherence trace that decays on a timescale T_2. Sharp dips appear in the coherence trace when the spacing of the DD sequence pulses is resonant with a target nuclear spin and this forms the basis for DD based sensing.

been refocussed forming a distinct echo signal as shown in Figs. 2.5(b)(i) and (ii). The Hahn echo is used to protect an initial state from quasistatic noise and extend coherence times. For increasing τ the refocussed sensor state will eventually decohere due to non-stationary noises (e.g. flip-flopping nuclear spin-dimers) that cannot be refocused by the Hahn echo pulse. However, this is on a much longer timescale called the T_2 coherence time.

2.3.3 Dynamical Decoupling

Dynamical decoupling was developed to extend the state protection provided by the Hahn echo. The principle is the same and is described in the preceding sections - a control π-pulse can refocus the dephasing due to quasistatic noise. Dynamical decoupling sequences are constructed from the repeated application of the Hahn echo. This allows one to extend the coherence time further than that afforded by the Hahn echo. Essentially, the Hahn echo breaks down when τ becomes too large as slowly fluctuating noise begins to have an effect. By increasing the number of pulses applied one can shorten the duration between pulses and become less sensitive to that slowly fluctuating noise. The efficacy of applying more and more pulses is then constrained by errors within those pulses and many sequences have been designed to mitigate this [152, 141, 48, 70, 144] and extend coherence times further.

The simplest dynamical decoupling sequence is the Carr-Purcell-Meiboom-Gill (CPMG) sequence [139, 140] which is just two Hahn echo pulses in a row and is described by $\tau - \pi_x - 2\tau - \pi_x - \tau$. This sequence can then be repeated N_p times to build longer sequences. In DD experiments the inter-pulse delay is scanned to obtain coherence traces, see Fig. 2.5(c). Like for the Hahn echo, the coherence under DD control decays on a timescale T_2. Dynamical decoupling removes the effect of static fields and also suppresses the effects of oscillating magnetic signals that are not resonant with the frequency of control pulses. When the signal *is* resonant with the pulses the DD fails leaving a characteristic coherence dip and this is the basis for DD based sensing.

Different DD sequences are specified by the phase of the pulses applied (i.e. about which axis in the xy-plane they flip the sensor state) and the spacing between the pulses. The choice of pulse phase and spacing has a large effect on the robustness to experimental errors [141, 48] (typically detunings, pulse flip angle errors and pulse phase angle errors).

The decay of the DD signal seen in Fig. 2.5(c) is caused by the fluctuating spin-bath. Many studies are interested in the interaction of the sensor with the entire bath [71, 142, 143] and how dynamical decoupling sequences can be designed to extend coherence times

[70, 144]. In the context of sensing and in particular nanoscale NMR and MRI we are interested in the interaction of the sensor with a single nuclear spin or small cluster of nuclear spins. In the work presented in this thesis we model the unitary dynamics of this reduced system and as a result the coherence traces presented do not exhibit an exponential decay. To more closely match experimental data this decay can be fit with the measured value of T_2.

In dynamical decoupling based quantum sensing the important property is that the decoupling actually fails when the control π-pulses are applied resonantly with an incident AC signal (i.e. a nearby nuclear spin). This failure presents as a characteristic dip in the coherence trace (see Fig. 2.5(c)). The position and strength of this coherence dip encode information about the nuclear spin's Larmor frequency (revealing the spin species) and hyperfine coupling to the NV (revealing the spin position). These characteristic coherence dips created by dynamical decoupling form the basis for nanoscale NMR and MRI and extracting accurate information from experimental data requires an accurate theoretical model. Different available models are discussed below and we then lay the groundwork for the new model developed in this thesis.

2.3.4 Semi-Classical Models

Dynamical decoupling experiments have been modelled effectively with semi-classical treatments [35, 1, 36, 143]. This assumption treats the nuclear spin signal as a classical fluctuating field which is useful when the quantum back-action on the environment is negligible, for instance for the detection of a large ensemble of weakly coupled nuclear spins [145]. In this thesis we will present a fully quantum treatment of the system but it is worth briefly discussing semi-classical method as we will take inspiration from it later. The semi-classical sensing Hamiltonian can be written

$$\hat{H}(t) = f(t)b(t)\hat{S}_z, \tag{2.20}$$

where $\hat{S}_z$ is the sensor spin operator, $b(t)$ is the incident classical noise and $f(t)$ is called the modulation function. The modulation function is a square wave that flips between ± 1 at each DD pulse. There is no back-action on the environment as $b(t)$ does not depend on the sensor spin state. If the noise is assumed to be Gaussian [143] then the coherence

signal can be derived as

$$\mathcal{L}(t) = \exp\left(-\frac{t^2}{2}\int_{-\infty}^{+\infty} S(\omega)F(\omega t)\frac{d\omega}{2\pi}\right), \tag{2.21}$$

where $S(\omega) = \int_{-\infty}^{+\infty} \langle b(t)b(0)\rangle e^{i\omega t}dt$ is the noise spectrum of $b(t)$ and $F(\omega t) = \frac{1}{t^2}\left|\int_0^t f(t)e^{-i\omega t}dt\right|^2$ is the dimensionless filter function. The semi-classical picture is that the dynamical decoupling creates a filter that is scanned across the noise spectrum as the spacing between the control pulses increases. Dips in coherence are generated when the peaks in the filter function coincide with peaks in the noise spectrum.

2.3.5 Quantum Models

During dynamical decoupling protocols the sensor becomes entangled with the nuclear spin target (see Eq. (2.19)). To model this entanglement accurately the nuclear spin target must be treated as a quantum state rather than a classical field. This is particularly important if one is interested in the effect of the DD protocol on the nuclear spin as well as the sensor spin e.g. in nuclear spin registers [14, 27, 28, 29, 30]. The semi-classical expression for the sensor coherence response, Eq. (2.21), is also strictly positive and thus fails to model strong coherence dips which report a negative coherence, like those seen in Fig. 2.5(c). Quantum models are required to accurately models these strong signals. Several quantum models have been developed including geometric methods [2, 3] and methods based on the Magnus expansion [37, 38] and the rotating wave approximation [39]. The Floquet theory approach that we develop is also a quantum model.

The geometric method is valid for the detection of single nuclear spin-1/2s under simple DD sequences. The free evolution of the nuclear spin between pulses is defined as a rotation about an effective magnetic field. This rotation is conditioned on the sensor spin state and the π-pulses repeatedly change the rotation axis. Studying the combination of all the rotations the sensor coherence response is expressed in terms of the effective magnetic fields. This method is mathematically equivalent to the Floquet treatment of spin-1/2 detection we develop in Chapter 3 however whereas we are able to generalise the Floquet approach to more complex systems the geometric method becomes unsuitable for treating the detection of larger clusters of spins or detection with complex DD sequences.

Two other quantum methods have been developed in the same time we developed our Floquet treatment. One applies the Magnus expansion to approximate the time ordered

exponential $\hat{\mathcal{T}}\exp(-i\int_0^t \hat{H}(s)ds)$. In Chapter 6 we actually expand this approach by including finite pulse durations. The other, based on the rotating wave approximation, transforms the Hamiltonian to the interaction picture and then neglects fast oscillating terms. Both these approaches provide effective static Hamiltonians that approximate the dynamics. The Floquet theory approach we develop also provides a static effective Hamiltonian.

In the current work we utilise Floquet theory by exploiting the fact that many experiments use dynamical decoupling sequences that are periodic repetitions of a basic unit. This treatment is quantum and can accurately model the entanglement of the sensor with the spin bath. We study the closed-system unitary dynamics of the interacting spin sensor and nuclear spin target.

2.4 Floquet Theory

Floquet theory is an analytic method for treating systems with temporally periodic Hamiltonians [40]. Floquet's *theorem* asserts the quasiperiodicity of the solutions to Schrödinger's equation under periodic Hamiltonians and represents a temporal analogue to Bloch theory which is concerned with spatially periodic Hamiltonians. The theory has been applied in conventional NMR [41, 146] and more recently in NV based experiments in the context of "time crystals" [147] - robustly periodic many-body systems.

2.4.1 Floquet's Theorem

Floquet's theorem states that for periodic Hamiltonians, $\hat{H}(t) = \hat{H}(t+T)$, there exist solutions to the Schrödinger equation with the property

$$|\psi_\gamma(t+T)\rangle = \exp(-i\epsilon_\gamma T)\,|\psi_\gamma(t)\rangle\,, \tag{2.22}$$

where ϵ_γ are called the *Floquet quasienergies* and $\gamma = 1, ..., D$ with D the dimension of the Hilbert space. Thus, Floquet's theorem tells us that these quantum states evolving under a periodic Hamiltonian are not themselves periodic but are, in fact, quasiperiodic, with the state obtaining a global phase $\epsilon_\gamma T$ every period. We call these states, *Floquet states*.

An equivalent formulation of Floquet's theorem asserts the existence of solutions of the form

$$|\psi_\gamma(t)\rangle = \exp(-i\epsilon_\gamma t)\,|\phi_\gamma(t)\rangle\,, \tag{2.23}$$

where $|\phi_\gamma(t+T)\rangle = |\phi_\gamma(t)\rangle$ *are* periodic and are called the *Floquet modes*.

A proof of Floquet's theorem follows from considering the eigenvalue equation for the one-period evolution operator, $|\psi_\gamma(t+T)\rangle = \hat{U}(t+T,t)\,|\psi_\gamma(t)\rangle = \exp(ir_\gamma(t))\,|\psi_\gamma(t)\rangle$, where the unitarity of $\hat{U}$ ensures that the eigenvalues are complex phases. It is only required to prove that the eigenvalues are independent of the initial time, t, so that we can define $\exp(ir_\gamma(t)) \equiv \exp(i\epsilon_\gamma T)$. Multiplying the eigenvalue equation by $\hat{U}(t'+T,t+T)$ achieves this, $|\psi_\gamma(t'+T)\rangle = \hat{U}(t'+T,t+T)\,|\psi_\gamma(t+T)\rangle = \exp(ir_\gamma(t))\hat{U}(t'+T,t+T)\,|\psi_\gamma(t)\rangle = \exp(ir_\gamma(t))\hat{U}(t',t)\,|\psi_\gamma(t)\rangle = \exp(ir_\gamma(t))\,|\psi_\gamma(t')\rangle$, where the periodicity of $\hat{H}(t)$ is necessary to assert that $\hat{U}(t'+T,t+T) = \hat{U}(t',t)$. Thus, solutions of the Schrödinger equation exist with the property $|\psi_\gamma(t+T)\rangle = \exp(-i\epsilon_\gamma T)\,|\psi_\gamma(t)\rangle$ for arbitrary t.

2.4.2 Stroboscopic Evolution

The Floquet states form a complete orthornormal basis so they can be used to propagate any arbitrary state. The evolution operator can be written as

$$\hat{U}(t) = \sum_\gamma |\psi_\gamma(t)\rangle\langle\psi_\gamma(0)| \tag{2.24}$$

$$= \sum_\gamma \exp(i\epsilon_\gamma t)|\phi_\gamma(t)\rangle\langle\phi_\gamma(0)|. \tag{2.25}$$

In dynamical decoupling experiments the state is typically only measured at integer multiples of the DD period, i.e. after N_p repetitions of a basic pulse sequence. Thus, we are uninterested in the state between these times and can simplify our analysis by only considering the stroboscopic evolution,

$$\hat{U}(N_pT) = \sum_\gamma \exp(i\epsilon_\gamma N_pT)|\phi_\gamma\rangle\langle\phi_\gamma|. \tag{2.26}$$

Thus the evolution is completely determined by the quasienergies and the static Floquet modes $|\phi_\gamma\rangle = |\phi_\gamma(N_pT)\rangle = |\phi_\gamma(0)\rangle$ and can be used to model the outcomes of experimental measurements $\langle\hat{O}\rangle$. If we define a static effective Hamiltonian, $\hat{H}_{\text{eff}}$, such that $\hat{U}(N_pT) = \exp(-i\hat{H}_{\text{eff}}N_pT)$, then the Floquet quasienergies are the energies of $\hat{H}_{\text{eff}}$ and the Floquet modes are the eigenstates of $\hat{H}_{\text{eff}}$. The effective Hamiltonian describes dynamics that match the true evolution at stroboscopic times, but does not correctly model the dynamics within each period. This is satisfactory for DD experiments and can be a useful tool for understanding the dynamics.

If one can construct the one-period evolution operator directly, then the quasienergies

and Floquet modes are obtained by diagonalisation. This is the method used in Chapter 3. However, if the state space is large or if the time-dependence of the Hamiltonian is complex the one-period evolution operator can be hard to construct. In this case Floquet theory offers an alternative method for determining the Floquet quasienergies and modes, as detailed below.

2.4.3 Floquet Space and the Floquet Hamiltonian

The formal solution to the time-dependent Schrödinger equation can be written as a time-ordered exponential, $\hat{U}(t) = \hat{T}\exp(-i\int_0^t \hat{H}(t')dt')$, however this can be difficult to evaluate due to the Hamiltonian not commuting with itself at different times, $[\hat{H}(t), \hat{H}(t')] \neq 0$. In contrast, the solution to the time-independent Schrödinger equation, $\hat{U}(t) = \exp(-i\hat{H}t)$, can be evaluated simply by diagonalising the Hamiltonian.

Floquet's theorem offers a new route to solving the Schrödinger equation for time-dependent periodic Hamiltonians - by expanding the periodic Hamiltonian into a static Hamiltonian in Floquet space. This new *Floquet Hamiltonian* is infinite in dimension but can often be diagonalised regardless, allowing for propagation of the system.

Substituting Eq. (2.23) into the Schrödinger equation we obtain

$$\hat{H}^F \left|\phi_\gamma(t)\right\rangle \equiv \left[\hat{H}(t) - i\frac{\partial}{\partial t}\right] \left|\phi_\gamma(t)\right\rangle = \epsilon_\gamma \left|\phi_\gamma(t)\right\rangle \tag{2.27}$$

which is the Floquet Hamiltonian, $\hat{H}^F$, eigenvalue equation when represented in Floquet space.

Floquet space [146] is an extended Hilbert space, $\mathcal{F} = \mathcal{H} \otimes \mathcal{L}_T$, which is the product space of the original Hamiltonian Hilbert space $\mathcal{H}$ and Fourier space $\mathcal{L}_T$, the space of all (square-integrable) T-periodic functions. The scalar product on this extended space is defined as

$$\langle\langle\varphi|\varphi'\rangle\rangle = \frac{1}{T}\int_0^T dt\, \langle\varphi(t)|\varphi'(t)\rangle\,, \tag{2.28}$$

where $|\varphi\rangle\rangle \in \mathcal{F}$ and we use double angle brackets to denote states in Floquet space. A complete orthonormal basis of the Floquet space is given by $|\alpha, m\rangle\rangle \iff |\alpha\rangle e^{im\omega t}$ where $\omega = 2\pi/T$ and $|\alpha\rangle$ forms a complete orthonormal basis of the original Hilbert space. A periodic state, $|\varphi(t)\rangle$ in $\mathcal{H}$ can be represented in $\mathcal{F}$ as

$$|\varphi\rangle\rangle = \sum_{\alpha m} \frac{1}{T}\int_0^T \langle\alpha|\varphi(t)\rangle\, e^{-im\omega t} dt |\alpha m\rangle\rangle, \tag{2.29}$$

which is time-independent. Similarly, the Floquet Hamiltonian can be represented in Floquet space with elements

$$\langle\langle \alpha, m|\hat{H}^F|\alpha', m'\rangle\rangle = \int_0^T \langle\alpha|\hat{H}(t)|\alpha'\rangle\, e^{-i(m-m')\omega t} dt + m\omega\delta_{\alpha\alpha'}\delta_{mm'} \tag{2.30}$$

and the eigenvalue equation Eq. (2.27) can be rewritten

$$\hat{H}^F|\phi_\gamma\rangle\rangle = \epsilon_\gamma|\phi_\gamma\rangle\rangle. \tag{2.31}$$

Consequently, diagonalising the Floquet Hamiltonian reveals the quasienergies and Floquet modes, $|\phi_\gamma\rangle\rangle$ which can be converted back to the original Hilbert space,

$$|\phi_\gamma(t)\rangle = \sum_{\alpha,m} \langle\langle \alpha, m|\phi_\gamma\rangle\rangle e^{im\omega t}\, |\alpha\rangle\,. \tag{2.32}$$

The Floquet modes and quasienergies fully describe the dynamics of the system and can be used to construct an evolution operator as described by Eq. (2.26).

This new route to solving the Schrödinger equation is applicable for periodic Hamiltonians and is useful if the dynamics is hard to solve in the original Hilbert space but the Floquet Hamiltonian can be diagonalised.

3 Floquet Theory for Dynamical Decoupling Based Quantum Sensing Experiments

In this chapter we present the first Floquet analysis of dynamical decoupling (DD) based quantum sensing experiments. The motivation for this is clear - many DD experiments employ periodic repetitions of a basic pulse unit (e.g. the Carr-Purcell-Meiboom-Gill (CPMG) or XY8 sequences). Our key finding is that we can associate the characteristic dips in sensor coherence traces with avoided crossings in an underlying Floquet spectrum.

Dynamical decoupling experiments apply trains of microwave pulses to a qubit sensor to effectively average out dephasing due to a noisy spin bath. However, when these pulses are applied resonantly with a nearby nuclear spin the decoupling drastically fails and characteristic dips appear in sensor coherence traces. Analytic modelling of these experiments often uses a semi-classical approach [35, 1, 36] where the sensor is subject to a classical AC magnetic field from the environment. This approximation is useful when the quantum back-action of the sensor on the environment is negligible but fails to capture the the true dynamics of the coupled sensor-nuclear target system. In fact, the sensor becomes entangled with the nuclear target and a more quantum approach is needed to model this. Quantum models include the geometric method [2, 3] and more recently (after publication of the work described here [49]) approaches based on the Magnus expansion [37, 38] and the rotating wave approximation [39]. Here we are motivated by the periodicity of many DD sequences to apply Floquet theory [40] which is an alternative quantum model. A key quantity is the Floquet quasienergy and we find that avoided crossings in the quasienergy spectrum are linked with the sensor coherence dips. The width of the avoided crossing determines the depth and width of the coherence dip. We are able to provide an analytic

expression for the coherence dip in terms of the system quasienergy only.

We begin by obtaining a general expression for the qubit sensor response to a dynamical decoupling sensing protocol in terms of the system Floquet quasienergies and Floquet modes. We then look further into the cases where the CPMG sequence is used and where the spin target is described by a 2-D Hilbert space (i.e. the detection of a spin-1/2 or a pseudospin-1/2). This discussion is then applied to the specific case of a nitrogen vacancy center detecting a single ^{13}C nuclear spin. Next we model a potential future sensor - the bismuth donor in silicon. This system is described and we model the detection of a ^{29}Si spin dimer. We also discuss the detection of a spin-trimer and how it can be distinguished from 3 equivalent spin dimers revealing the higher order correlations.

In this chapter the theoretical model is constrained by a common assumption - that the microwave control pulses are instantaneous, taking infinitesimal time to invert the sensor state. In the following chapter this assumption is relaxed and we utilise Floquet theory again to provide the first quantum model of finite-duration-pulse effects. This chapter covers content published in Lang et. al (2015) [49].

3.1 Spin Sensing

Here we consider a general spin-qubit sensor, with *up* ($|u\rangle$) and *down* ($|d\rangle$) states coupled to a nuclear spin target which could be a single spin or spin cluster. The sensor-target coupling is assumed to be pure dephasing so that in general the Hamiltonian can be written as

$$\hat{H} = |u\rangle\langle u| \otimes \hat{H}_u + |d\rangle\langle d| \otimes \hat{H}_d, \tag{3.1}$$

where $\hat{H}_{u,d}$ is the nuclear spin Hamiltonian conditioned on the sensor spin state. This Hamiltonian is described as pure-dephasing because it does not mix the qubit states (no $|u\rangle\langle d|$ or $|d\rangle\langle u|$ terms) and can only affect the qubit phase. The conditional nuclear Hamiltonian arises due to the *quantum back-action* of the sensor on the spin target. The qubit sensor is not a passive observer but actively affects the dynamics of the target. This back-action leads to the bifurcated evolution of the nuclear spin $\hat{U}(t) = |u\rangle\langle u| \otimes \hat{U}_u^{(0)} + |d\rangle\langle d| \otimes \hat{U}_d^{(0)}$ where $\hat{U}_{u,d}^{(0)}(t) = \exp\left(-i\hat{H}_{u,d}t\right)$ is the free evolution of the nuclear spin conditioned on the sensor spin state.

Dynamical decoupling based sensing experiments begin by initialising the sensor spin into an equal superposition state. The nuclear spin target is assumed to be in the initial

state, $|\mathcal{B}_0\rangle$, selected from a thermal ensemble. The initial state of the combined system is the product state

$$|\psi_0\rangle = \frac{1}{\sqrt{2}}\left(|u\rangle + |d\rangle\right)|\mathcal{B}_0\rangle\,. \tag{3.2}$$

Whilst a general qubit superposition state can also have some complex phase difference between the u and d states we define the x-axis such that the initial superposition state is always of the form in Eq. (3.2). Any other phases will be defined relative to this (e.g. the phase of microwave π-pulses).

The initial state is allowed to evolve under the bifurcated evolution to the (possibly) entangled state

$$|\psi(t)\rangle = \frac{1}{\sqrt{2}}\left(|u\rangle\,|\mathcal{B}_u(t)\rangle + |d\rangle\,|\mathcal{B}_d(t)\rangle\right), \tag{3.3}$$

where $|\mathcal{B}_{u,d}(t)\rangle = \hat{U}_{u,d}(t)\,|\mathcal{B}_0\rangle$. This state is entangled if $|\mathcal{B}_u(t)\rangle \neq c\,|\mathcal{B}_d(t)\rangle$ for some complex number, c.

Experiments then measure the remaining spin projection along the initialisation axis (the x-axis) to obtain $\mathcal{L}(t) = \langle\hat{\sigma}_x\rangle = \langle\psi(t)|\hat{\sigma}_x|\psi(t)\rangle = \mathrm{Re}\{\langle\mathcal{B}_u(t)|\mathcal{B}_d(t)\rangle\}$. This sensor response is called the *coherence* and takes values between $+1$ and -1. Experiments measure the coherence for a range of times, t, and produce coherence traces which we seek to model analytically.

If the bifurcated evolution happens to produce identical bath states, $|\mathcal{B}_u(t)\rangle = |\mathcal{B}_d(t)\rangle$ then the initial sensor state is preserved and $\mathcal{L}(t) = 1$. If the sensor and the spin target are maximally entangled $\mathcal{L}(t) = 0$ and $\mathcal{L}(t) = -1$ if the bifurcated evolution produces bath states differing only in sign, $|\mathcal{B}_u(t)\rangle = -\,|\mathcal{B}_d(t)\rangle$, which leaves the sensor and target completely unentangled but the sensor state has been flipped to $|\psi\rangle = \left(|u\rangle - |d\rangle\right)/\sqrt{2}$.

To obtain the expectation value, $\langle\hat{\sigma}_x\rangle$, in experiments the measurement is repeated many times. In this case we must average over all possible initial thermal bath states, $|\mathcal{B}_0\rangle$. Using the evolution operators we can express the coherence in terms of the initial bath state $\mathcal{L}(t) = \mathrm{Re}\left\{\langle\mathcal{B}_0|\hat{U}_u^\dagger\hat{U}_d|\mathcal{B}_0\rangle\right\}$ and then the average over the thermal ensemble of bath states can be expressed with the trace operator,

$$\mathcal{L}(t) = \frac{1}{D}\,\mathrm{Re}\left\{\mathrm{Tr}\left\{\hat{U}_u^\dagger\hat{U}_d\right\}\right\}. \tag{3.4}$$

where D is the dimension of the bath Hilbert space.

In a free-induction-decay experiment, where the system is allowed to evolve freely between initialisation and readout, the evolution of the states is simply given by the

conditional free evolution, $\hat{U}_{u,d}(t) = \hat{U}^{(0)}_{u,d}(t)$. However, in pulsed experiments the evolution is constructed by switching between the *up* and *down* evolution at each pulse, (e.g. for a CPMG experiment $\hat{U}^{(2)}_u(t = 4\tau) = \hat{U}^{(0)}_u(\tau)\hat{U}^{(0)}_d(2\tau)\hat{U}^{(0)}_u(\tau)$ and $\hat{U}^{(2)}_d(t = 4\tau) = \hat{U}^{(0)}_d(\tau)\hat{U}^{(0)}_u(2\tau)\hat{U}^{(0)}_d(\tau)$) so the the evolution operators must be replaced by the pulsed evolution operators (e.g. $\hat{U}_{u,d}(t) = \hat{U}^{(2)}_{u,d}(t)$). Coherence traces are then constructed by scanning the inter-pulse delay, τ.

3.1.1 Floquet Analysis

Motivated by the periodicity of CPMG and many other sequences we apply Floquet theory. This states that for a periodic Hamiltonian (with period T) one can find solutions to Schrödinger's equation of the form $|\psi(t)\rangle = e^{-i\epsilon t}|\phi(t)\rangle$ where ϵ is the Floquet quasienergy and $|\phi(t)\rangle$ is the periodic Floquet mode. In DD experiments we are only interested in the state at stroboscopic times, $t = N_pT$, so we write $|\psi(N_pT)\rangle = e^{-i\epsilon N_pT}|\phi(N_pT)\rangle \equiv e^{-i\epsilon N_pT}|\phi\rangle$.

The stroboscopic evolution operator can be written in terms of the Floquet modes and quasienergies,

$$\hat{U}(N_pT) = \sum_\gamma |\psi_\gamma(N_pT)\rangle\langle\psi_\gamma(0)| = \sum_\gamma \exp(-i\epsilon_\gamma N_pT)|\phi_\gamma\rangle\langle\phi_\gamma|, \tag{3.5}$$

where $\gamma = 1, ..., D$ with D the Hamiltonian dimension. Substituting this expression into Eq. (3.4) we obtain

$$\mathcal{L}(N_pT) = \frac{1}{D}\,\mathrm{Re}\left\{\mathrm{Tr}\left\{\sum_{\gamma,\gamma'}\exp(i(\epsilon_{u\gamma} - \epsilon_{d\gamma'})N_pT)\,|\phi_{u\gamma}\rangle\langle\phi_{u\gamma}|\phi_{d\gamma'}\rangle\langle\phi_{d\gamma'}|\right\}\right\}. \tag{3.6}$$

We then choose to perform the trace over the $|\phi_{u\gamma}\rangle$ basis and take the real part to get the general expression

$$\mathcal{L}(N_pT) = \frac{1}{D}\sum_{\gamma,\gamma'}\cos((\epsilon_{u\gamma} - \epsilon_{d\gamma'})N_pT)|\,\langle\phi_{u\gamma}|\phi_{d\gamma'}\rangle\,|^2 \tag{3.7}$$

which expresses the sensor response completely in terms of the Floquet modes and quasienergies of the system. This expression is valid for all periodic DD experiments where the control π-pulses are assumed to be instantaneous and this is a key result of this chapter. This expression presents a general way to express the sensor coherence response in any periodic dynamical decoupling based quantum sensing.

Considering the CPMG sequence specifically, we are able to utilise a symmetry in the bifurcated evolution to reshape this expression into a more instructive form. The CPMG sequence is described by $\tau - \pi_x - 2\tau - \pi_x - \tau$ where π_x denotes a π-flip about the x-axis and 2τ is the inter-pulse delay. The CPMG period is $T = 4\tau$ and the one-period evolution operators are

$$\hat{U}_u^{(2)}(T = 4\tau) = \hat{U}_u^{(0)}(\tau)\hat{U}_d^{(0)}(\tau)\hat{U}_d^{(0)}(\tau)\hat{U}_u^{(0)}(\tau), \tag{3.8}$$

$$\hat{U}_d^{(2)}(T = 4\tau) = \hat{U}_d^{(0)}(\tau)\hat{U}_u^{(0)}(\tau)\hat{U}_u^{(0)}(\tau)\hat{U}_d^{(0)}(\tau). \tag{3.9}$$

Importantly, the upper and lower evolution operators are related by the form $\hat{U}_u^{(2)} = \hat{A}\hat{B}$ and $\hat{U}_d^{(2)} = \hat{B}\hat{A}$ where $\hat{A} = \hat{U}_u^{(0)}\hat{U}_d^{(0)}$ and $\hat{B} = \hat{U}_d^{(0)}\hat{U}_u^{(0)}$. This symmetry causes the upper and lower evolutions to have identical eigenvalues and thus identical quasienergies. This can be seen by considering the eigenvalue equation for $\hat{A}\hat{B}$: $\hat{A}\hat{B}\mathbf{v} = \lambda\mathbf{v}$ and then pre-multiplying by $\hat{B}$: $\hat{B}\hat{A}\left(\hat{B}\mathbf{v}\right) = \lambda\left(\hat{B}\mathbf{v}\right)$ which shows that the eigenvalue, λ, is shared by $\hat{A}\hat{B}$ and $\hat{B}\hat{A}$. This symmetry simplifies the analysis as we can write $\epsilon_{u\gamma} = \epsilon_{d\gamma} \equiv \epsilon_\gamma$.

Grouping the double summation in Eq. (3.7) into equal, $\gamma = \gamma'$, and unequal, $\gamma \neq \gamma'$, indices then gives

$$\mathcal{L}(N_pT) = \frac{1}{D}\sum_\gamma |\left\langle\phi_{u\gamma}|\phi_{d\gamma}\right\rangle|^2 + \frac{1}{D}\sum_{\gamma\neq\gamma'} \cos((\epsilon_\gamma - \epsilon_{\gamma'})N_pT)|\left\langle\phi_{u\gamma}|\phi_{d\gamma'}\right\rangle|^2 \tag{3.10}$$

and we can rewrite the first term by using the orthonormality of the Floquet modes ($\sum_{\gamma'} |\phi_{d\gamma'}\rangle\langle\phi_{d\gamma'}| = \hat{\mathbb{I}}$). The first term can be rewritten as

$$\frac{1}{D}\sum_\gamma |\left\langle\phi_{u\gamma}|\phi_{d\gamma}\right\rangle|^2 = \frac{1}{D}\sum_\gamma \left\langle\phi_{u\gamma}|\phi_{d\gamma}\right\rangle\left\langle\phi_{d\gamma}|\phi_{u\gamma}\right\rangle, \tag{3.11}$$

$$= \frac{1}{D}\sum_\gamma \langle\phi_{u\gamma}|\left(\mathbb{I} - \sum_{\gamma'\neq\gamma} |\phi_{d\gamma'}\rangle\langle\phi_{d\gamma'}|\right)|\phi_{u\gamma}\rangle, \tag{3.12}$$

$$= 1 - \frac{1}{D}\sum_{\gamma\neq\gamma'} |\left\langle\phi_{u\gamma}|\phi_{d\gamma'}\right\rangle|^2. \tag{3.13}$$

We can thus combine the first and second terms in Eq. (3.10) to obtain our final form,

$$\mathcal{L}(N_pT) = 1 - \frac{2}{D}\sum_{\gamma\neq\gamma'} \sin^2(\frac{1}{2}(\epsilon_\gamma - \epsilon_{\gamma'})N_pT)|\left\langle\phi_{u\gamma}|\phi_{d\gamma'}\right\rangle|^2. \tag{3.14}$$

which models the sensor response to a nuclear spin target under CPMG control (or any pulse sequence with the same internal symmetry ($\epsilon_{u\gamma} = \epsilon_{d\gamma}$)).

Clearly when the summation is zero the the coherence signal is $\mathcal{L} = 1$, implying the dynamical decoupling has successfully protected the initial sensor state. The summation terms are formed of two parts: a pulse-number dependent part and a pulse-number independent part. The parameter N_p is set by the experiment when choosing how many repetitions of the basic DD sequence to apply. Scanning N_p causes the signal to oscillate but we can see from the above equation that the signal is bound between $\mathcal{L}(N_pT) \leq 1$ and a coherence *envelope* $\mathcal{L}(N_pT) \geq \mathcal{L}_{\text{env}}(T) \equiv 1 - \frac{2}{D}\sum_{\gamma\neq\gamma'} |\langle\phi_{u\gamma}|\phi_{d\gamma'}\rangle|^2$. This envelope is filled with oscillating dips and sidebands upon increasing N_p. It is important to remember that although the Floquet quasienergies and modes are time independent, they are still parametrised by the sequence period, T. Characteristic coherence dips appear at values of T where $|\langle\phi_{u\gamma}|\phi_{d\gamma'}\rangle|^2 = 1$, these dips have a maximal contrast when $(\epsilon_\gamma - \epsilon_{\gamma'})N_pT = \pi$.

Thus the coherence response can be completely understood in terms of the Floquet quasienergies and modes. In the next section we treat the $D = 2$ case and connect the Floquet quasienergies and modes to the physical parameters present in the static Hamiltonian by directly constructing and then diagonalising the one-period evolution operator.

3.2 Spin-1/2 Detection

For the detection of single spin-1/2 nuclei the target Hilbert space is clearly 2-dimensional. However, 2-D Hilbert spaces can also be isolated from larger spaces when the transitions to other levels are suppressed. This happens for the Si:Bi system coupled to nuclear spin-dimers [142] as will be discussed in Sec. 3.4. In this section we treat a general 2-D spin system coupled to the sensor and analyse the coherence response. Later we apply this to the specific case of the NV detection of a single ^{13}C spin-1/2 and the Si:Bi detection of a ^{29}Si spin-dimer pseudospin-1/2.

For the $D = 2$ case, orthonormality requires that $|\langle\phi_{u1}|\phi_{d2}\rangle|^2 = |\langle\phi_{u2}|\phi_{d1}\rangle|^2$ and we can always define $\epsilon_1 = -\epsilon_2 \equiv \epsilon$ by some arbitrary shift in energy. The sensor response under CPMG control, Eq. (3.14), can then be written

$$\mathcal{L}(N_pT) = 1 - 2\sin^2(\epsilon N_pT)\,|\langle\phi_{u1}|\phi_{d2}\rangle|^2. \tag{3.15}$$

We seek to connect the Floquet quasienergies and modes to the physical parameters in the static nuclear Hamiltonian. This is done by constructing, then diagonalising the one-period evolution operators, $\hat{U}^{(2)}_{u,d}$.

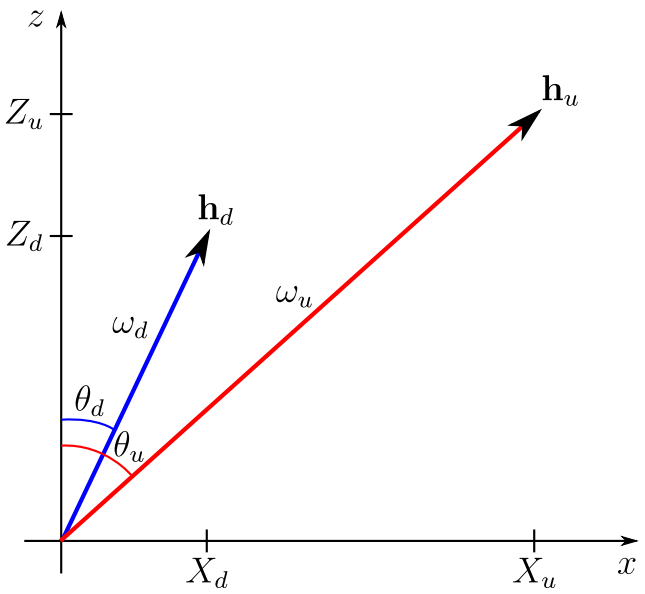

Figure 3.1: The spin-1/2 target feels a field conditioned on the state of the sensor, $\mathbf{h}_{u,d} = (X_{u,d}, 0, Z_{u,d}) = \omega_{u,d}(\sin\theta_{u,d}, 0, \cos\theta_{u,d})$.

A general nuclear spin-1/2 Hamiltonian (conditioned on the sensor spin state) can be written as

$$\hat{H}_{u,d} = \mathbf{h}_{u,d} \cdot \hat{\mathbf{I}}, \tag{3.16}$$

where $\mathbf{h}_{u,d}$ is a sensor-spin-state dependent magnetic field felt by the nuclear spin. The specifics of these fields are determined by the system of study. For now we simply take our fields to be

$$\mathbf{h}_{u,d} = (X_{u,d}, 0, Z_{u,d}) = \omega_{u,d}(\sin\theta_{u,d}, 0, \cos\theta_{u,d}) \tag{3.17}$$

(in Cartesian and polar coordinates). In general, the fields may have a $Y_{u,d}$ component however one can always eliminate this by choosing the correct coordinate system (defining the xz-plane as the plane containing both $\mathbf{h}_u$ and $\mathbf{h}_d$) and this simplifies the analysis. Fig. 3.1 is a schematic of the fields $\mathbf{h}_{u,d}$ and their components.

The free evolution under $\hat{H}_{u,d}$ is given by

$$\hat{U}^{(0)}_{u,d}(t) = \exp(-i\hat{H}_{u,d}t) = \cos(\frac{\omega_{u,d}t}{2})\hat{\mathbb{I}} - i\sin(\frac{\omega_{u,d}t}{2})(\sin\theta_{u,d}\hat{\sigma}_x + \cos\theta_{u,d}\hat{\sigma}_z), \tag{3.18}$$

(see App. A) where $\hat{\sigma}_x$ and $\hat{\sigma}_z$ are Pauli matrices. The nuclear spin-1/2 evolves simply by precessing about either field $\mathbf{h}_{u,d}$ with frequency $\omega_{u,d}$ (depending on the state of the sensor). Starting with the sensor spin in a superposition of u and d states means the nuclear spin evolution bifurcates with the nuclear spin simultaneously evolving around each field. In dynamical decoupling experiments π-pulses repeatedly flip the state of the sensor. This

causes the evolution of the nuclear spin to flip between $\hat{H}_u$ and $\hat{H}_d$.

Under CPMG control, the one-period evolution operators are given by Eqs. (3.8) and (3.9). These are found by explicit concatenation of the free evolution operators, Eq. (3.18) and is detailed in Appendix C. The one-period evolution operators can be written in the form

$$\hat{U}^{(2)}_{u,d}(T) = \cos(\epsilon T)\hat{\mathbb{I}} - i\sin(\epsilon T)(\sin\theta^F_{u,d}\hat{\sigma}_x + \cos\theta^F_{u,d}\hat{\sigma}_z), \tag{3.19}$$

which resembles the free evolution operators, Eq. (3.18). Note that this operator acts as a black-box to transform the initial state to the final state after one period, i.e. it does not give the evolution within the period. One can define a conditional *effective* Hamiltonian, $\hat{H}^{\text{eff}}_{u,d} = \mathbf{h}^{\text{eff}}_{u,d}\cdot\hat{\mathbf{I}}$, and a conditional effective field, $\mathbf{h}^{\text{eff}}_{u,d} = 2\epsilon\left(\sin\theta^F_{u,d}, 0, \cos\theta^F_{u,d}\right)$, such that $\hat{U}^{(2)}_{u,d}(T) \equiv \exp\left(-i\hat{H}^{\text{eff}}_{u,d}T\right)$. Thus instead of considering the true dynamics of the nuclear state, rotating about $\mathbf{h}_u$ and $\mathbf{h}_d$ and switching at every pulse, one can consider instead that the nuclear spin undergoes some constant free evolution about the effective fields $\mathbf{h}^{\text{eff}}_u$ and $\mathbf{h}^{\text{eff}}_d$ for the entire period T. Note that the effective angular frequency is 2ϵ and is independent of the sensor spin state, as expected from the symmetry of the CPMG sequence. The quasienergy, ϵ, here describes the energy of the effective Hamiltonian.

Diagonalising $\hat{U}^{(2)}_{u,d}(T)$ gives the Floquet quasienergies, $\epsilon_1 = -\epsilon_2 \equiv \epsilon$, where ϵ is given by the relation (see Appendix C)

$$\cos\epsilon T = \cos\frac{\omega_u T}{4}\cos\frac{\omega_d T}{4} - \sin\frac{\omega_u T}{4}\sin\frac{\omega_d T}{4}\cos(\theta_u - \theta_d) \tag{3.20}$$

and the Floquet modes,

$$|\phi_{u,d1}\rangle = \begin{pmatrix}\cos\frac{\theta^F_{u,d}}{2}\\ \sin\frac{\theta^F_{u,d}}{2}\end{pmatrix}, \quad |\phi_{u,d2}\rangle = \begin{pmatrix}-\sin\frac{\theta^F_{u,d}}{2}\\ \cos\frac{\theta^F_{u,d}}{2}\end{pmatrix}, \tag{3.21}$$

which are defined by the angles $\theta^F_{u,d}$ which also specify the direction of the effective fields $\mathbf{h}^{\text{eff}}_{u,d}$. This Floquet angle is defined in Appendix C. Substituting these into Eq. (3.15) gives

$$\mathcal{L}(N_pT) = 1 - 2\sin^2(\epsilon N_pT)\sin^2\left(\frac{\theta^F_u - \theta^F_d}{2}\right), \tag{3.22}$$

which is our Floquet expression of the sensor coherence for the detection of a spin-1/2 system. Figure 3.2(a) compares the coherence response with the Floquet quasienergies and the Floquet angles. We see that dips in coherence are associated with avoided crossings in

the Floquet quasienergy spectrum. Equations (3.20),(3.21),(3.22) refine our more general expression for the sensor coherence response (Eq. (3.7)) to a specific case seen in sensing experiments.

The above expression can be understood in two parts; a pulse-number-independent coherence envelope, $\mathcal{L}_{\text{env}}(T)$, and the pulse-number-dependent oscillatory behaviour. When scanning over N_p the signal oscillates within the bounds $\mathcal{L}_{\text{env}}(T) \leq \mathcal{L}(N_p T) \leq 1$ where the envelope is given by

$$\mathcal{L}_{\text{env}}(T) = 1 - 2\sin^2\left(\frac{\theta_u^F - \theta_d^F}{2}\right). \tag{3.23}$$

When $\theta_u^F - \theta_d^F = 0$ the effective fields, $\mathbf{h}_{u,d}^{\text{eff}}$, are parallel and the envelope takes a maximal value of $\mathcal{L}_{\text{env}}(T) = +1$, i.e. there is no dip. In this case the effective Hamiltonian is independent of the sensor spin state, i.e. the quantum back action is removed by the DD sequence and the sensor records no signal. When $\theta_u^F - \theta_d^F = \pi$ the effective fields are anti-parallel and the envelope reaches a minimum of $\mathcal{L}_{\text{env}}(T) = -1$. This defines the position of the coherence dips as demonstrated in Fig. 3.2(a). What remains is for the experiment to provide enough pulses to fill the envelope. Fig. 3.2(b) shows a coherence envelope and its successive filling as N_p increases. At the dip position, the signal contrast is given by the pulse-number-dependent behaviour

$$\mathcal{L}_{\text{dip}}(N_p) = 1 - 2\sin^2(\epsilon N_p T). \tag{3.24}$$

It is also possible to re-express the coherence, Eq. (3.22) in terms of the quasienergy only (see Appendix C), i.e. removing $\theta_{u,d}^F$ from the expression. For simplicity we define the Floquet *phase* as $\varepsilon(T) = \epsilon(T)T$ (note that the quasienergy is also a function of T) and we can write

$$\mathcal{L}(N_p T) = 1 - 2\sin^2(N_p \varepsilon(T)) \left[\frac{\cos^2(\varepsilon(T)/2) - \cos^2(\varepsilon(T/2))}{\cos^2(\varepsilon(T)/2)}\right] \tag{3.25}$$

which again separates into pulse-number dependent and independent terms. Scanning N_p causes the coherence signal to oscillate but this is bounded by the coherence envelope, obtained by setting $\sin^2(N_p\varepsilon(T)) = 1$. The dip condition is determined from $\mathcal{L}_{\text{env}}(T_{\text{dip}}) = -1$ which is satisfied when

$$\varepsilon(T_{\text{dip}}/2) = \pi/2, \tag{3.26}$$

as this causes the term in the square brackets in Eq. (3.25) to reach unity. Equation (3.26)

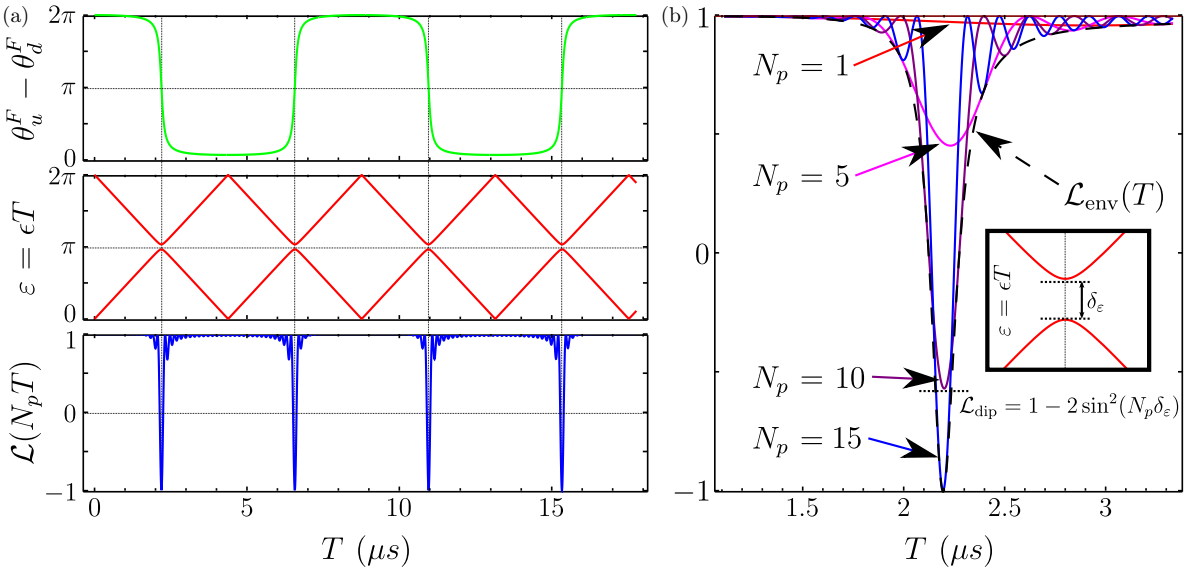

Figure 3.2: (a) Shows the coherence response, $\mathcal{L}(N_pT)$, Floquet quasienergies ϵ (plotted as a the Floquet phase, $\varepsilon = \epsilon T$, for readability) and Floquet angle difference $\theta_u^F - \theta_d^F$ of a sensor detecting a spin-1/2 system with $N_p = 15$ repetitions of CPMG. The conditional fields felt by the spin-1/2 are $\mathbf{h}_u = (50, 0, 460)$ kHz $\times 2\pi$ and $\mathbf{h}_d = (0, 0, 450)$ kHz $\times 2\pi$. Dips in coherence appear when $\theta_u^F - \theta_d^F = \pi$ and coincide with avoided crossings in the quasienergy spectra. (b) Shows a zoom of the first dip appearing in (a). The pulse-number independent coherence envelope is shown and the filling of the envelope with increasing N_p is demonstrated.

is our Floquet theory dip condition. We see from Fig. 3.2(a) that the coherence dips are associated with avoided crossings in the Floquet quasienergy spectrum. (In plots we scale the quasienergy by T and plot this as the Floquet phase, $\varepsilon = \epsilon T$, as it makes it easier to see the avoided crossings in scans of T.) The *depth* of the dip is related to the splitting parameter, $\delta_\varepsilon = 2(\pi - \varepsilon(T_{\rm dip}))$, which is the width of the avoided crossing, see Fig. 3.2(b) inset. At the dip position it is still necessary to apply enough pulses so that one obtains a visible contrast. We can model the dip contrast by inserting the Floquet theory dip condition (Eq. (3.26)) into the expression Eq. (3.25). In terms of the avoided crossing width the dip contrast is then given by

$$\mathcal{L}(N_p T_{\rm dip}) = 1 - 2\sin^2(\frac{1}{2}N_p\delta_\varepsilon). \tag{3.27}$$

Hence a true level crossing provides no signal as the avoided crossing width would be zero, $\delta_\varepsilon = 0$. For $N_p\delta_\varepsilon > \pi$ the width and shape of the dip becomes largely independent of N_p and is fully determined by the Floquet anti-crossing and envelope function, since the $\sin^2(\frac{1}{2}N_p\varepsilon)$ factor simply superposes fast oscillations on the coherence envelope. A narrow avoided-crossing (low splitting, δ_ε small) gives a single, sharp (but weaker) coherence dip,

while a wider avoided crossing (large δ_ε) has a broad envelope. It is only for low $N_p\delta_\varepsilon \ll \pi$ that the dip height is strongly dependent on N_p; here the central height increases as $(N_p\delta_\varepsilon)^2$. Equations (3.25),(3.27) are a key result from this chapter as they link the avoided crossing shape to the coherence dip shape.

3.2.1 The Average Hamiltonian

The avoided crossing in the Floquet quasienergy spectrum indicates the mixing of some unperturbed states. When the quantum back-action is small (i.e. $\hat{H}_u \approx \hat{H}_d$) these unperturbed states are the eigenstates of the average Hamiltonian, $\hat{H}_{\rm av} = \frac{1}{2}(\hat{H}_u + \hat{H}_d)$, as can be seen from the short τ behaviour

$$\hat{U}_{u,d}(T = 4\tau) = \exp(-i\hat{H}_{u,d}\tau)\exp(-i\hat{H}_{d,u}2\tau)\exp(-i\hat{H}_{u,d}\tau) \approx \exp(-i\frac{1}{2}(\hat{H}_u + \hat{H}_d)4\tau) \tag{3.28}$$

for small τ. The average Hamiltonian can be used to predict the dip positions when the quantum back action is weak. More specifically, considering the Baker-Campbell-Hausdorff formula, the above approximation is valid when $||\hat{H}_{\rm av}|| \gg |||[\hat{H}_u, \hat{H}_d]|||$. The average Hamiltonian has energies $\epsilon_{\rm av} = \pm\frac{1}{2}\sqrt{\omega_u^2 + \omega_d^2 + 2\omega_u\omega_d\cos(\theta_u - \theta_d)}$ and the spectrum has a level crossing when $T = \pi/\epsilon_{\rm av}$.

The average Hamiltonian can provide a good measure of the dip position in certain conditions but the (inactive) level crossing cannot account for the signal contrast (as discussed in the previous section). As the modelling in this chapter does not assume any constraints on the quantum back-action strength the dip condition $\varepsilon(T_{\rm dip}/2) = \pi/2$ is always valid.

3.3 Sensing with the Nitrogen Vacancy Center in Diamond

The nitrogen vacancy center has provided a fertile testbed for nanoscale NMR and MRI experiments [61, 130, 131, 132] as well as other sensing experiments [77, 81, 91]. Whilst other solid state defect systems are being explored for similar purposes [9, 11, 116, 118, 120] the NV center remains the most productive platform.

Watershed experiments have detected single remote ^{13}C spins [1, 2, 3] and spin clusters [17, 18] in the diamond interior and demonstrated their application as quantum registers [27, 30]. The detection of nanoscale volumes of nuclear spins external to the diamond has also been demonstrated [21, 22, 23] and even the detection of single nuclear spins on the diamond surface [24, 25, 26].

Here we model an NV center coupled to a single ^{13}C spin-1/2 nuclei in the diamond lattice. We will choose the NV $m_s = 0$ and $m_s = +1$ spin states as the d and u qubit sensor states respectively. The static Hamiltonian is given by

$$\hat{H} = -\gamma_n \mathbf{B} \cdot \hat{\mathbf{I}} + \hat{S}_z \mathbf{A} \cdot \hat{\mathbf{I}}, \tag{3.29}$$

where γ_n is the nuclear gyromagnetic ratio, $\mathbf{B}$ is the applied magnetic field, usually applied parallel to the NV crystal axis, $\mathbf{A}$ is the position dependent hyperfine field felt by the nuclear spin, $\hat{\mathbf{I}}$ represents the nuclear spin-1/2 and $\hat{S}_z = |+1\rangle\langle+1|$ is the NV spin operator.

The conditional nuclear spin evolution is governed by $\hat{H}_{u,d} = \mathbf{h}_{u,d} \cdot \hat{\mathbf{I}}$ where the $\mathbf{h}_{u,d} = -\gamma_{\mathrm{n}} \mathbf{B} + m_{u,d} \mathbf{A}$ and $m_d = 0$, $m_u = +1$. Thus, when the NV is in the $d \equiv m_s = 0$ state the nuclear spin simply precesses about the applied magnetic field at the Larmor frequency. When the the NV is the $m_s = 1$ state the nuclear spin precesses about the magnetic field perturbed by the hyperfine field.

For simplicity we consider magnetic and hyperfine fields that have no y-component, $\mathbf{A} = (A_x, 0, A_z)$, $\mathbf{B} = (B_x, 0, B_z)$. As discussed in the previous section it is always possible to find a frame where this is the case. We can then write $\mathbf{h}_{u,d} = \omega_{u,d}(\sin\theta_{u,d}, 0, \cos\theta_{u,d})$ where $\omega_{u,d} = \sqrt{(-\gamma_n B_x + m_{u,d} A_x)^2 + (-\gamma_n B_z + m_{u,d} A_z)^2}$ and $\theta_{u,d} = \arctan((-\gamma_n B_x + m_{u,d} A_x)/(-\gamma_n B_z + m_{u,d} A_z))$.

Our result from the previous section allows us to express the coherence response of the NV center, Eq. (3.22), in terms of the Floquet quasienergies and modes, Eqs. (3.20),(3.21). As dynamical decoupling based sensing is typically employed to detect remote spins the hyperfine coupling will be much weaker than the Larmor frequency. In Fig. 3.3 we simulate the detection of a single ^{13}C and plot the associated quasienergy spectrum. We can see that that the coherence dips are associated with avoided crossings and the width of the avoided crossing controls the coherence dip contrast.

As the hyperfine coupling is weak the average Hamiltonian provides a good approximation for the coherence dip positions. However, as we derived our expression for the coherence by directly constructing the one-period evolution operator (and making no approximations) the expression remains valid in regimes where the average Hamiltonian prediction does not. In fact, the Floquet expression can be useful when the picture of sharp dips breaks down completely. To show this generality, we imagine an experiment that scans the magnetic field strength perpendicular to the NV crystal axis rather than aligned with it. Later, from Chapter 4 onwards, we use apply Floquet theory to more complex

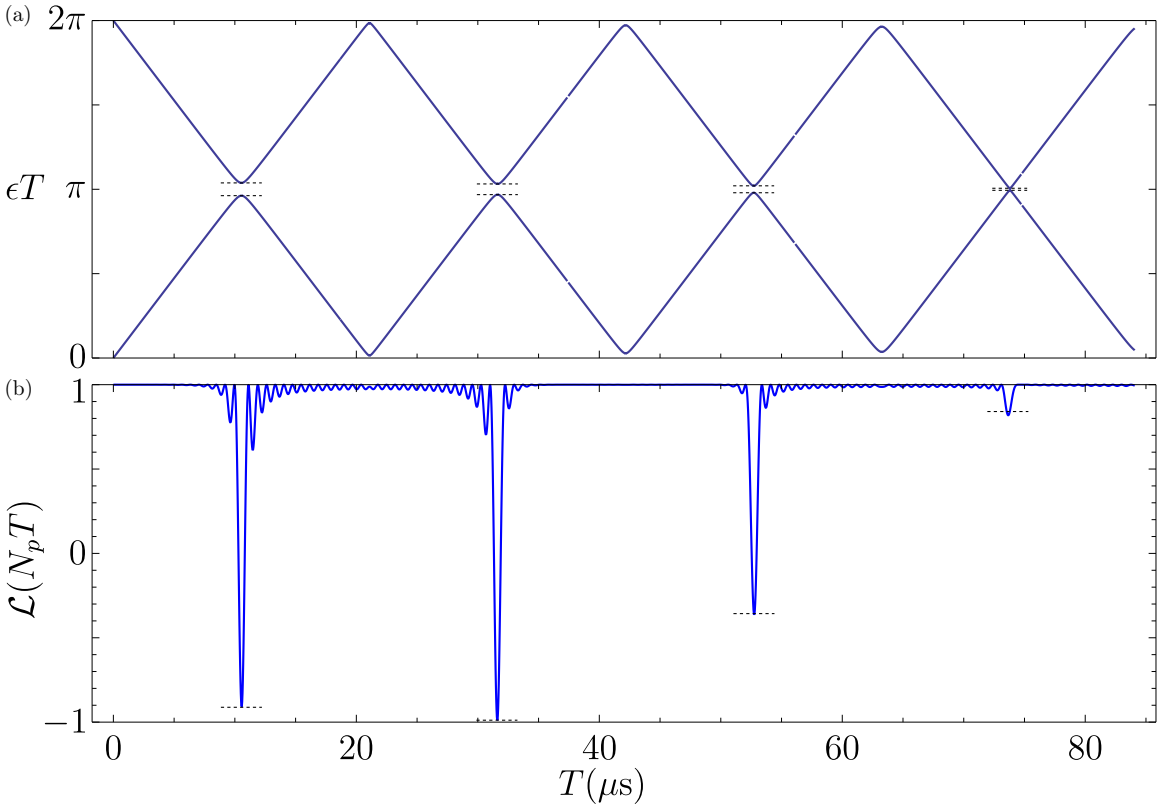

Figure 3.3: The nitrogen vacancy detection of a single ^{13}C. (a) Shows the Floquet quasienergy spectrum with avoided crossings. The dotted black lines indicate the width of the avoided crossings. (b) Shows the NV coherence response with sharp coherence dips associated with the avoided crossings. The black dotted lines indicate the dip depth calculated from our analytic expression, $\mathcal{L}(N_pT_{\text{dip}}) = 1 - 2\sin^2(N_p\delta_\varepsilon)$, which depends on the avoided crossing width, δ_ε. For simulation a magnetic field of 100 G is applied along the NV axis, the hyperfine coupling is $[A_x, A_z] = [10, 25]$ kHz $\times 2\pi$ and $N_p = 15$ repetitions of the CPMG sequence are applied (30 pulses total).

dynamical decoupling control and for this require a perturbative approach. This limits the range of validity but is suitable for most sensing experiments. The strength of the analysis in this section is that it is not limited in the same way.

Figure 3.4(a) simulates a nitrogen vacancy center coupled to a single ^{13}C. A magnetic field is applied perpendicular to the NV crystal axis and we can see that there is no clear dip structure in the coherence trace and the average Hamiltonian prediction fails. Figure 3.4(b) shows a trace with a weaker applied magnetic field where the dip positions are well approximated by the average Hamiltonian prediction. Figure 3.4(c) shows the coherence behaviour whilst scanning the strength of the magnetic field and a clear checkerboard pattern of oscillatory and non-oscillatory regions appear. We can use Floquet theory to understand the transition between these regions. Our derived expressions are valid globally and we find plots of the coherence envelope reveal the underlying checkerboard structure that is filled with oscillatory sidebands. Understanding this behaviour opens up possibilities for controlling the coherence response, i.e. resolution, by tuning the applied magnetic field. In the next section we study a possible future sensor, the bismuth donor in silicon, that also promises high controllability.

3.4 Sensing with a Bismuth Donor in Silicon

The success of the NV center has prompted the study of other defect centers with similar properties in diamond [9, 116, 118] and silicon carbide [120]. Donors in silicon have recently received great interest due to their incredibly long coherence times [122] and the strong (Zeeman state) mixing they exhibit at moderate magnetic fields [124]. They have not yet been employed as spin sensors due to technical challenges involved in addressing a single donor spin however progress is being made in this respect [11, 127, 128] and the strong magnetic field dependence of the mixing promises a new handle for control in sensing experiments.

The group V donors: phosphorous, arsenic, antimony and bismuth donate an extra electron that is localised at the donor site at low temperatures. They all exhibit mixing, i.e. mixing of the uncoupled electron and nuclear Zeeman states due to the large hyperfine coupling, but bismuth exhibits the strongest mixing and the discussion here is restricted to bismuth donors. Here a single bismuth donor in silicon (Si:Bi) is considered for possible future sensing experiments.

There are two key differences between the NV and Si:Bi systems. The first difference

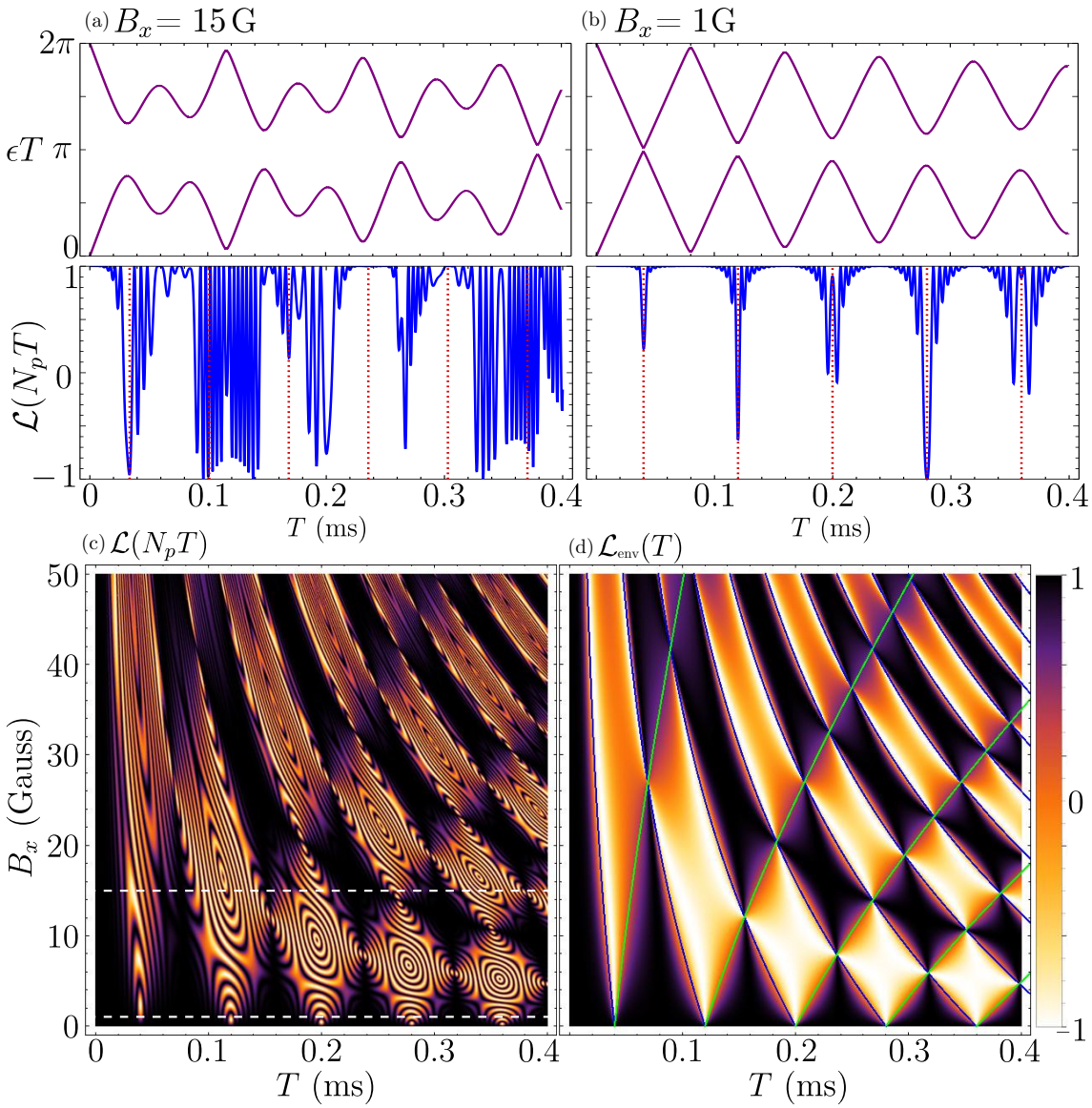

Figure 3.4: The nitrogen vacancy center detection of a single ^{13}C with a magnetic field applied perpendicular to the NV axis. Different coherence regimes appear at different magnetic field strengths (a) $B_x = 15$ G. The avoided crossings are wide and start to overlap resulting in a highly oscillatory coherence spectra with no clear dips. The average Hamiltonian prediction fails (red dotted vertical lines) (b) $B_x = 1$ G. The avoided crossings are narrow resulting in sharp coherence dips. The average Hamiltonian prediction is accurate. (c) Scanning the magnetic field strength reveals a checkerboard pattern. (d) Plotting the coherence envelope, Eq. (3.23) reveals the underlying structure. The blue and green bounding lines are given by $T = (2m-1) \times 2\pi/|\omega_u \pm \omega_d|$. For simulations here the hyperfine coupling is $[A_x, A_z] = [0, 50]$ kHz $\times 2\pi$ and 10 repetitions of the CPMG sequence are applied.

is that the Si:Bi defect is a point-like defect and thus has no inherent crystal axis like the NV center which means the hyperfine coupling for the Si:Bi is isotropic. The isotropic coupling causes the spin sensor to be insensitive to single nuclear spins as we will see from the Hamiltonian - the dominant decoherence source here are flip-flopping spin dimers [142]. The other difference is that the mixing of the Si:Bi spin levels leads to a sensor qubit transition, ΔE, that is non-linear in the applied magnetic field - i.e. points exist where $d\Delta E/dB_z = 0$ [148, 123]. At these magnetic fields the sensor is insensitive to small fluctuations in magnetic field so the effective coupling to the environment becomes massively suppressed. These points are called optimal working points (OWPs).

3.4.1 The Central Spin Hamiltonian

In this work we consider the bismuth donor as it exhibits the strongest mixing. The central spin Hamiltonian is

$$\hat{H}_{\text{Si:Bi}} = -\gamma_{\text{e}} B_z \hat{S}_z - \gamma_{\text{Bi}} B_z \hat{I}_z + A\hat{\mathbf{S}} \cdot \hat{\mathbf{I}}, \tag{3.30}$$

where γ_{e} and γ_{Bi} are the electron ($\hat{\mathbf{S}}$) and bismuth-nuclear ($\hat{\mathbf{I}}$) gyromagnetic ratios respectively, B_z is an applied magnetic field that defines the z-axis (there is no intrinsic crystal axis like for the NV), $A = 1.48$ GHz $\times 2\pi$ is the (isotropic) hyperfine coupling. The hyperfine coupling mixes the electron and nuclear Zeeman levels as seen in Fig. 3.5 (adapted from [149]). The electron has spin $S = 1/2$ and the bismuth has spin $I = 9/2$ so there are a total of $(2S+1)(2I+1) = 20$ states and two are selected from these to act as the sensor qubit - we choose the 12-9 transition, indicated in Fig. 3.5. Due to the mixing the spin projections $m_{u,d} = \langle u, d|\hat{S}_z|u, d\rangle \equiv m_{u,d}(B_z)$ are magnetic field dependent as shown in Fig. 3.6. This is in stark contrast to the NV case and offers controllability of the sensor-target coupling. For the 12-9 transition the OWP is at $B \approx 0.19$ T, where the two spin projections are equal $m_u = m_d$.

3.4.2 Spin Dimer Detection

For sensing experiments we consider the detection of a ^{29}Si nuclear spin dimer. Selecting the 12-9 Si:Bi transition, the experimental protocol will apply microwave pulses resonant with this energy splitting. In the frame rotating with this microwave frequency (and making the RWA by ignoring the counter-rotating terms) the Hamiltonian can be written

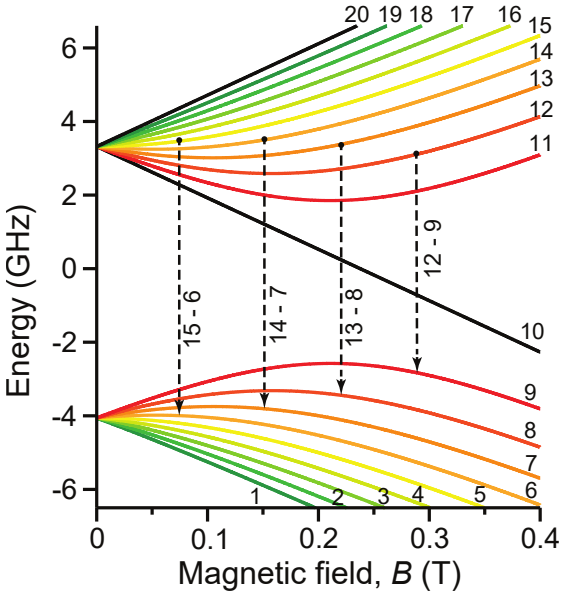

Figure 3.5: The spectrum of Si:Bi as a function of magnetic field, B. The energy levels are strongly mixed due to the large hyperfine coupling. The levels are labelled in terms of increasing energy $|l\rangle$ for $l = 1, ..., 20$ and possible qubit transitions are shown. Figure adapted from Balian et al. 2015

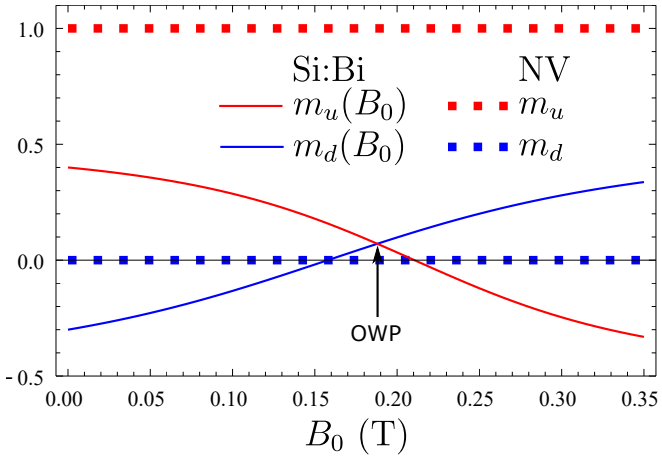

Figure 3.6: The spin projections $m_{u,d} = \langle u, d|\hat{S}_z|u, d\rangle$ for the Si:Bi ($12 \leftrightarrow 9$ transition) and NV ($0 \leftrightarrow +1$ transition). For Si:Bi the spin projections are highly dependent on the applied magnetic field and an optimal working point (OWP) exists at $B_0 \approx 0.19$ T where $m_u = m_d$ essentially removing the quantum back action of the sensor on the environment.

as

$$\hat{H}_0 = -\gamma_{\rm n} B_z(\hat{I}_{1z} + \hat{I}_{2z}) + \hat{S}_z(A_1\hat{I}_{1z} + A_2\hat{I}_{2z}) + C_{12}(\frac{1}{4}(\hat{I}_1^+\hat{I}_2^- + \hat{I}_1^-\hat{I}_2^+) - \hat{I}_{1z}\hat{I}_{2z}), \quad (3.31)$$

where $\gamma_{\rm n}$ is the ^{29}Si gyromagnetic ratio, $A_{1,2}$ are the isotropic hyperfine couplings to the ^{29}Si spins and C_{12} is the spin-spin dipolar coupling. Here $\hat{\mathbf{I}}_{1,2}$ represent the two ^{29}Si spins (not the bismuth nuclear spin as in $\hat{H}_{\rm Si:Bi}$). This Hamiltonian is in a pure dephasing form and can be written as $H_0 = |u\rangle\langle u|\hat{H}_u + |d\rangle\langle d|\hat{H}_d$ where

$$\hat{H}_{u,d} = -\gamma_n B_z(\hat{I}_{1z}+\hat{I}_{2z}) + m_{u,d}(B_z)(A_1\hat{I}_{1z}+A_2\hat{I}_{2z}) + C_{12}(\frac{1}{4}(\hat{I}_1^+\hat{I}_2^- + \hat{I}_1^-\hat{I}_2^+) - \hat{I}_{1z}\hat{I}_{2z}) \quad (3.32)$$

is the nuclear Hamiltonian conditioned on the sensor spin state and $m_{u,d} = \langle m_{u,d}|\hat{S}_z|m_{u,d}\rangle$. The insensitivity to single nuclear spins can be seen from this Hamiltonian by turning off the dipolar coupling. In the absence of the spin-spin coupling the Si:Bi is coupled to two single nuclear spins and the conditional nuclear Hamiltonians commute with each other, $[\hat{H}_u, \hat{H}_d] = 0$. Thus the CPMG sequence will completely remove their effect on the Si:Bi. For NV centers it is the anisotropic hyperfine coupling that allows single spins to be detected - for NV centers coupled to single nuclear spins the conditional nuclear Hamiltonians do not typically commute.

The nuclear dimer Hilbert space is 4-D but as the $|\uparrow,\uparrow\rangle$ and $|\downarrow,\downarrow\rangle$ states do not couple to the other states they can be neglected leaving a 2-D "pseudospin-1/2". Looking at only the part of the Hamiltonian affecting the $\{|\uparrow,\downarrow\rangle, |\downarrow,\uparrow\rangle\} \equiv \{|\Uparrow\rangle, |\Downarrow\rangle\}$ subspace we have

$$\hat{H}_{u,d} = \begin{pmatrix} \frac{m_{u,d}}{2}(A_1 - A_2) + \frac{C_{12}}{4} & \frac{C_{12}}{4} \\ \frac{C_{12}}{4} & \frac{m_{u,d}}{2}(A_2 - A_1) + \frac{C_{12}}{4} \end{pmatrix} \quad (3.33)$$

$$= \mathbf{h}_{u,d} \cdot \hat{\mathbf{I}}, \quad (3.34)$$

where $\mathbf{h}_{u,d} = (C_{12}/2, 0, m_{u,d}(A_1 - A_2))$ and now $\hat{\mathbf{I}}$ is the pseudospin-1/2 operator. Moving to the second line above we have ignored the secular dipolar coupling contribution ($\frac{C_{12}}{4}\hat{\mathbb{I}}$) which only shifts the total energy. Thus we have a nuclear pseudospin-1/2 Hamiltonian conditioned on the state of the Si:Bi so to calculate the sensor response under CPMG control we can apply the general form of the coherence function we derived via the Floquet formalism, Eq. (3.22).

Figure 3.7 simulates the Si:Bi detection of a ^{29}Si spin dimer. The coherence response

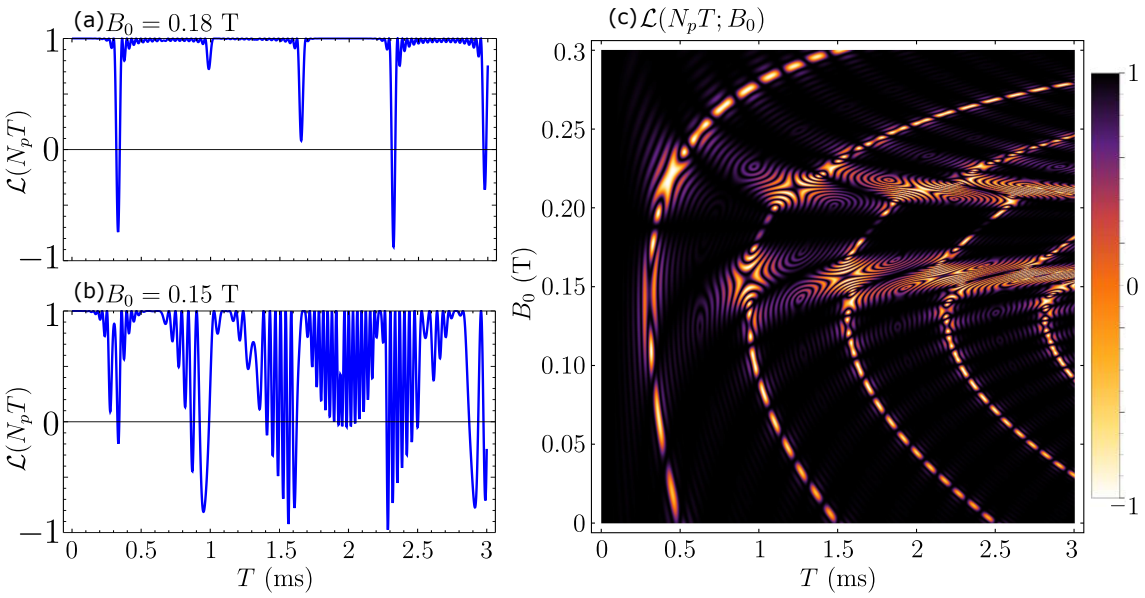

Figure 3.7: The Si:Bi detection of a ^{29}Si spin dimer at (a) 0.18 T (near the OWP) and (b) 0.15 T and (c) magnetic fields between 0 and 0.3 T. Here 10 repetitions of the CPMG sequence are applied, the dimer has hyperfine couplings $A_1 = 180$ kHz $\times 2\pi$ and $A_2 = 100$ kHz $\times 2\pi$ and dipolar coupling strength $C_{12} = 1.3$ kHz $\times 2\pi$.

resembles that of the NV detection of a single spin-1/2 because the spin-dimer dynamics are reduced to a single pseudospin-1/2. Due to the magnetic field dependence of the spin projections, $m_{u,d}(B_z)$, the sensor response is highly dependent on the applied magnetic field strength. As seen in parts Figs. 3.7(a) and (b) the coherence can switch between regions of highly oscillatory behaviour and sharp dips. When the magnetic field applied is close to the OWP ($B_z \approx 0.19$ T) the coherence dips are sharper. This corresponds to the Floquet avoided crossings being narrowed. Figure 3.7(c) shows a magnetic field sweep of the sensor coherence. This magnetic field control is desirable for increased resolution - to determine signals where the dips are close together. Furthermore, the long coherence times of silicon donors allows for increased sensitivity as the nuclear target can be interrogated for longer. The combination of these two properties would make the Si:Bi system an effective quantum sensor.

Figure 3.8 simulates the Si:Bi detection of a spin dimer for different coupling parameters. The average Hamiltonian prediction for the dip position is shown to be accurate for only a subset of experiments whilst the Floquet analysis prediction, $\varepsilon(T_{\text{dip}}/2) = \pi/2$, is always valid.

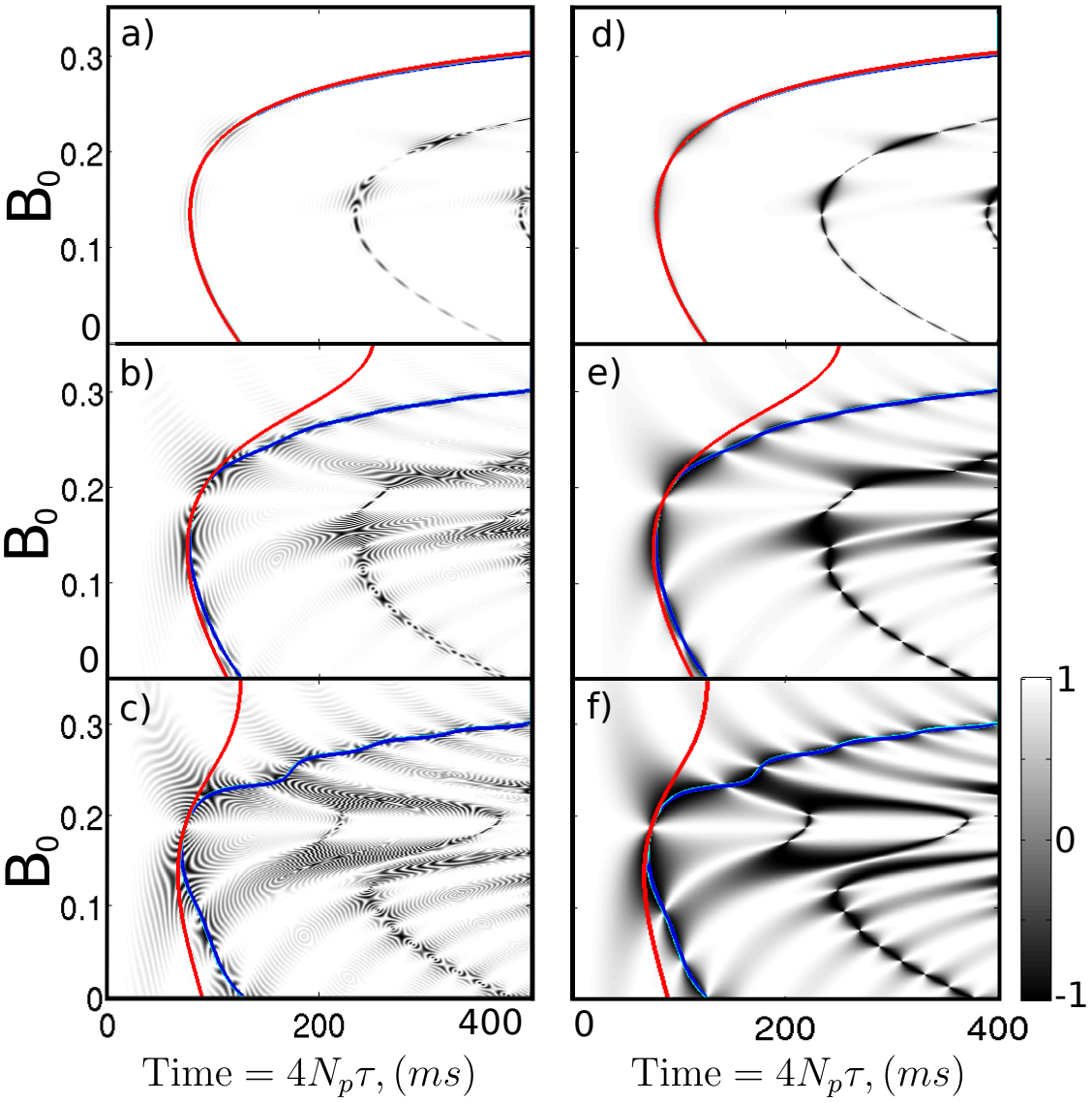

Figure 3.8: Magnetic field sweeps for a Si:Bi sensor detecting a ^{29}Si spin dimer. The full coherence function is shown on the left and its envelope on the right for different values of $R = |A_1 - A_2|/C_{12}$. (a) and (d) R = 100, (b) and (e) R = 20, (c) and (f) R = 10. The solid blue curve shows the dip prediction via the Floquet method. The solid red line is the average Hamiltonian prediction. Only for large R does the average Hamiltonian method offers a good approximation at all magnetic fields. The horizontal axis scans $4N_p\tau = N_pT$, the total sequence length.

3.4.3 Spin Trimer Detection

In this section we apply the Floquet approach to the system depicted in Fig. 3.9(a): we compare the Si:Bi DD based detection of three independent spin pairs (pseudospin-1/2s) with a 3-cluster which, in the absence of many-body interactions would give identical signatures.

For the 3-cluster, we take three spins, with hyperfine couplings $A_k \equiv A_1, A_2, A_3$ to the sensor spin and with mutual dipolar interactions $C_{ij} \equiv C_{12}, C_{23}, C_{31}$. Disregarding interactions, the energy cost of the spin dime flip-flops is $\Delta A_{ij} = A_i - A_j$. The Hamiltonian for three spin-1/2s interacting with a spin sensor and a magnetic field $\mathbf{B} = B_z\mathbf{z}$ is given by

$$\hat{H}_{\text{tot}} = -\gamma_n B_z \sum_k \hat{I}_{kz} + \hat{S}_z \sum_k A_k \hat{I}_{kz} + \sum_{ij} C_{ij}(\frac{1}{4}(\hat{I}_i^+ \hat{I}_j^- + \hat{I}_i^- \hat{I}_j^+) - \hat{I}_{iz}\hat{I}_{jz}). \tag{3.35}$$

For the independent pairs, we take three spin pairs, with the same dipolar interactions C_{ij} as the 3-cluster, but which are independent of each other. To have similar frequencies as the 3-cluster, we must have similar energy costs for all three spin flips; and they must obey the cyclic condition of the 3-cluster $\Delta A_{12} + \Delta A_{23} + \Delta A_{31} = 0$. Pair 1 has two spins with interaction C_{12} and a pair of hyperfine couplings (A_1, A_2); pair 2 has interaction C_{23} and hyperfine couplings (A_2, A_3); pair 3 has C_{31} and hyperfine couplings (A_3, A_1). We take $C_{12} = C_{23} = \frac{1.05}{2\pi}$ kHz and $C_{31} = \frac{2.2}{2\pi}$ kHz, realistic values for nuclear impurities in the silicon lattice. We take $A_1 = \frac{180}{2\pi}$ kHz, $A_3 = \frac{100}{2\pi}$ kHz and $A_2 = 0$, thus our pairs correspond to $R \simeq 100 - 40$ (as defined in Fig. 3.8). The choice of $A_2 = 0$ does not involve much loss of generality. If a state-dependent Hamiltonian is chosen, the A_1, A_2, A_3 values can be shifted by an arbitrary constant without perturbing the dynamics.

First we set aside all pseudospin approximations and diagonalise the full Hamiltonian to simulate the dynamics, using the complete 8-state basis of the 3-cluster as well as the complete 20-state basis of the bismuth sensor including the host nuclear spin. We evaluate the coherence numerically rather than using Eq. (3.22). A similar calculation was carried out with the three disjoint pairs and Figures 3.9(b) and (c) show maps of the coherence in both cases.

One striking feature of the 3-cluster coherence map in Fig. 3.9(c) is that some of the coherence dips are split into doublets with similar structure. The origin of these is the splitting of the Hilbert space into separate subspaces; we see that the $\sum_k \hat{I}_{kz} = \pm 3/2$ cluster states $|\uparrow\uparrow\uparrow\rangle$ and $|\downarrow\downarrow\downarrow\rangle$ do not mix with any other states and thus make no

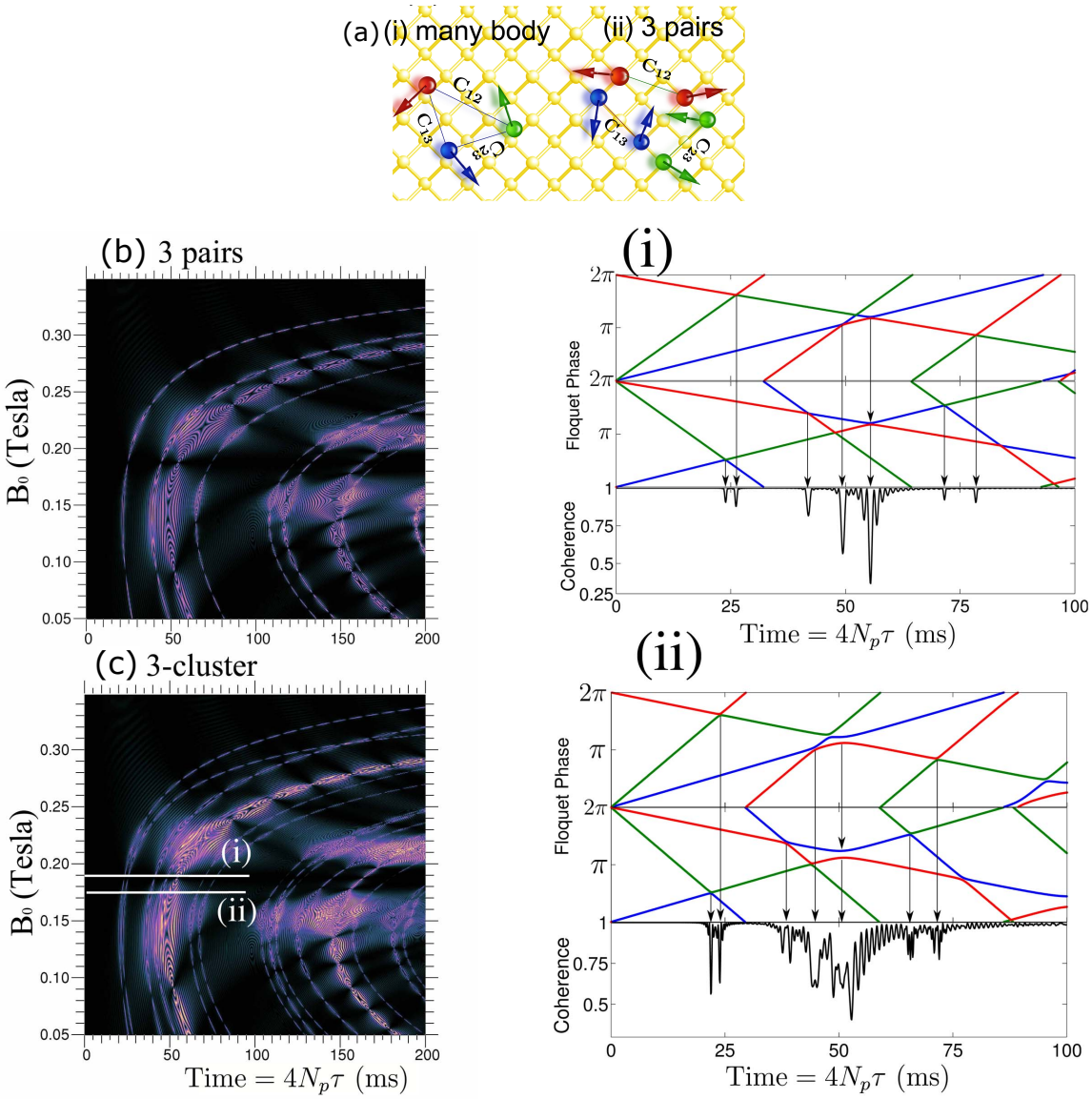

Figure 3.9: (a) To isolate many body effects we compare the 3-cluster with a system of 3 disjoint pairs that have the same dipolar couplings and hyperfine differences. (b) and (c) show the coherence function maps obtained for 3 pairs and the 3-cluster. The loci of dips are split for the 3-cluster, illustrating the effect of many-body correlations. The splitting is due to a secular dipolar coupling term $C_{ij}\hat{I}_{iz}\hat{I}_{jz}$ that affects the $I = +1/2$ and $I = -1/2$ subspaces differently. The two right hand panels (i) and (ii) show single traces corresponding to the cuts in (c) as well as the six corresponding quasienergies: in case (i) in a weak coupling regime the dips are narrow. In case (ii) there is stronger coupling, the avoided crossings of the corresponding quasienergies are broader. The dip splitting for the 3-cluster can be seen from the quasienergy spectra. Each subspace contributes a set of avoided crossings that are slightly unaligned creating pairs of coherence dips. The coherence maps here have been calculated with a full numerical propagation of the total Hamiltonian for $N_p = 100$ repetitions of the CPMG sequence. ($4N_p\tau = N_pT = t_{\rm tot}$).

contribution to the coherence signal. The doublets arise from the separate $\sum_k \hat{I}_{kz} = \pm 1/2$ subspaces. In other words, the $|\uparrow\uparrow\downarrow\rangle$, $|\uparrow\downarrow\uparrow\rangle$ and $|\downarrow\uparrow\uparrow\rangle$ states with total quantum number $\sum_k \hat{I}_{kz} = +1/2$ do not interact with the equivalent $\sum_k \hat{I}_{kz} = -1/2$ subspace. This is because the dipolar coupling preserves the total spin, $\sum_k \hat{I}_{kz}$. Each subspace provides a locus of dips with a slightly different shift. In contrast to the spin pairs, in the case of the 3-cluster, the secular components of the dipolar coupling, $(C_{jk}\hat{I}_{zj}\hat{I}_{zk})$, yield a non-trivial dynamical effect.

Figures 3.9(i) and (ii) show the coherence traces and Floquet quasienergy spectra for two magnetic field values. We can see that near the "weak-coupling" regime of optimal working points (i), the dips are sharp and narrow as are the avoided crossings; in contrast, away from the OWP point (ii), avoided crossings are broader and even overlap. We will use average Hamiltonian theory to estimate the avoided crossing position, and hence T_{dip}. The nuclear average Hamiltonian is

$$\hat{H}_{\text{av}} = -\gamma_n B_z \sum_k \hat{I}_{kz} + \frac{m_u + m_d}{2} \sum_k A_k \hat{I}_{kz} + \sum_{ij} C_{ij} \left(\frac{1}{4}(\hat{I}_i^+ \hat{I}_j^- + \hat{I}_i^- \hat{I}_j^+) - \hat{I}_{iz}\hat{I}_{jz}\right) \quad (3.36)$$

and we estimate the nuclear average Hamiltonian spectrum by considering only the diagonal terms (as the off-diagonal terms are much weaker, $C_{ij} \ll \Delta A_{ij}$). The average Hamiltonian quasienergies represent the initial gradient of the spectral lines seen in Figs. 3.9(i) and (ii). Thus we can determine where the degeneracy points will be and this estimates the coherence dip positions. We find that

$$T_{\text{dip}}^{\pm(ij)} = \frac{2\pi}{|(A_i - A_j)(\frac{m_u+m_d}{2}) \pm (\frac{C_{jk}-C_{ki}}{2})|}, \quad (3.37)$$

where $T_{\text{dip}}^{\pm(ij)}$ corresponds to the doublet of dips produced by the ij'th pair of spins and k is the 3rd interacting spin - contributing the higher-order correlation. The mean dip position exposes the value of $A_i - A_j$ and the splitting exposes the dipolar coupling strengths. In Fig. 3.10 we compare values from Eq.(3.37) with the full numerics and see a good fit.

3.5 Future Work

In this chapter we have demonstrated that dynamical decoupling based sensing experiments can be understood using Floquet theory. We discussed how the Si:Bi system is an effective sensor because of the delicate magnetic field strength dependence. The NV spin projections

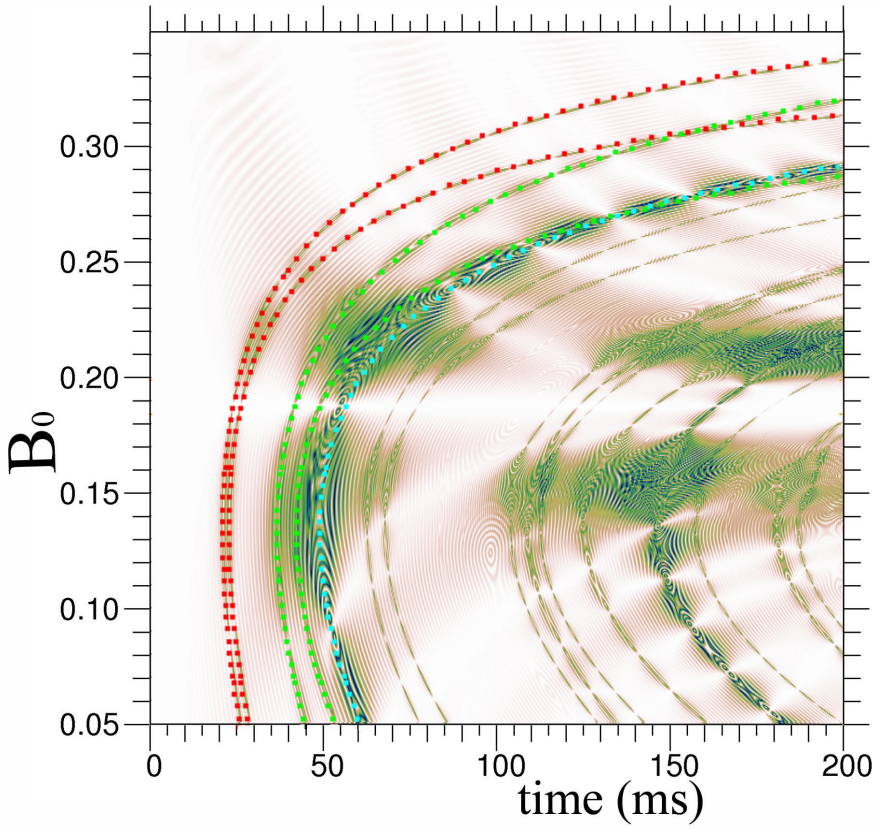

Figure 3.10: Coherence map for an interacting cluster of three spins (3-cluster). The coloured lines show comparisons with Eq. (3.37) showing excellent agreement with numerics obtained by diagonalisation of the full joint sensor-cluster Hamiltonian.

are not magnetic field dependent but it would be interesting to search for regimes where it is (for instance, at the ground state level anti-crossing [137]). It would be worthwhile seeking out optimal working points in the nitrogen vacancy center or other defect systems. This could offer the same controllability that benefits the Si:Bi system. We also discussed the detection of higher order clusters. It is an interesting problem in general to study the signature of larger clusters and this would be worthwhile studying for the NV sensor. In this chapter we have assumed that the microwave π-pulses are instantaneous but in the following chapters we model dynamical decoupling based sensing with finite-duration pulses.

4 Finite-Duration-Pulse Effects in Dynamical Decoupling Based Sensing

The work in this chapter is motivated by a recent study which demonstrated that the short, but finite, duration of microwave π-pulses in dynamical decoupling based sensing experiments can lead to the appearance of new so-called *spurious* coherence dips [42]. Typically, dynamical decoupling based sensing experiments are modelled by assuming that the microwave pulses occur instantaneously, taking infinitesimal time. In fact, it was shown that extra coherence dips can appear under certain dynamical decoupling control sequences due to the finite duration of the pulses. Importantly, the appearance of spurious signals can create ambiguities in spin classification. A simple argument based on Bloch sphere rotations was applied to predict the positions of the spurious signals under the XY family of DD sequences but this did not predict the signal contrast and was limited to XY family sequences. Later, a semi-classical study [43] demonstrated that spurious dips can be identified by the delicate dependence of their contrast (depth) on a global phase added to all pulses within the DD pulse sequence. As the system is still periodic, we apply Floquet theory to derive the first quantum model of the dynamics at these spurious resonances. We obtain an analytic expression that accurately models the position and shape of these spurious dips (as well as the expected DD response). The arrival of new coherence dips is understood as the activation (opening) of previously inactive (closed) avoided crossings in the Floquet quasienergy spectrum. The width of the avoided crossing determines the sharpness and contrast of the coherence dip.

Finite-duration-pulse effects were observed in standard NMR [150, 151] and were shown to affect the decay of nuclear spin echoes. This is a many-body effect relying on the dipolar

coupling between nuclei. Also, in the context of optimising qubit control, DD sequences were designed to extend coherence times under realistic pulse control [45]. Our work here, based in nanoscale NMR, is separate as it is not a many body effect and we do not study the coherence decay of the NV. We analyse the finite pulse effect on the resonant oscillations in the coherence profile due to coherently coupled nuclear spins. Spurious signals are a feature of DD based sensing experiments - where characteristic dips appear in sensor coherence traces. Spurious coherence dips were not reported in initial studies [1, 2, 3] as they are much weaker than the expected signals. This is because the spurious signal only accumulates within each pulse rather than between the pulses. Only in later experiments which required many more control pulses (for more sensitive detection [42] or optimised control [73]) were the spurious dips observed.

In the previous chapter we modelled the experiments with a common assumption [143] - that the microwave π-pulses are infinitely fast and take zero time to invert the state of the qubit sensor. We now introduce some finite pulse duration into our model but the dynamical decoupling protocol remains periodic and we can continue to apply Floquet theory and we seek the system Floquet modes and quasienergies to express the sensor response. In the previous chapter, the Floquet modes and quasienergies were obtained by first directly concatenating sections of free evolution to construct the one-period evolution operator and then directly diagonalising it. Whilst this method is still valid for numerics it is no longer analytically efficient as the finite pulse propagators introduced between sections of free evolution make the construction of the one-period evolution operator cumbersome. Instead, we apply a more powerful technique from Floquet theory - a periodic Hamiltonian can be represented as a time-independent (but infinite) Floquet Hamiltonian in a larger Floquet space (Sec. 2.4.3). An effective Hamiltonian governing the stroboscopic evolution can also be represented in this new Floquet space. Comparing the Floquet Hamiltonian and the effective Floquet Hamiltonian then reveals the effective Hamiltonian in the original Hilbert space with eigenenergies and eigenstates that *are* the Floquet quasienergies and Floquet modes of the periodic system.

We model the NV detection of a single nuclear spin-1/2 (e.g a ^{13}C or ^{1}H) and begin by preparing the Hamiltonian in the "toggling-frame" where it is periodic and perturbative. We find a set of modulation functions that generalise the single modulation function used in many semi-classical and quantum analyses [35, 1, 36, 37, 38, 39]. We then use Floquet theory to construct the Floquet space Hamiltonian. Due to the perturbative coupling the

Floquet Hamiltonian takes on a block diagonal form with the blocks connected to an effective Hamiltonian that describes the stroboscopic evolution. Diagonalising the effective Hamiltonian yields the Floquet quasienergies and modes which we then use to analytically express the new spurious dips, caused by the finite duration of control pulses, as well as the expected DD coherence dips. We find, as in the last chapter, that the characteristic coherence dips are associated with avoided crossings in the quasienergy spectra. The appearance of the spurious dips is associated with the opening of, previously closed, avoided crossings. The new analysis can model dynamical decoupling protocols where the microwave pulses are applied at any phase. We specifically discuss the effect of finite duration pulses on the XY8 and CPMG sequences and show that our analytic expressions fit well to numeric simulations. Whilst spurious dips were first observed in the robust XY8 sequence [152, 141, 42] and have since been shown to appear in other robust sequences [39] we demonstrate that the finite-pulse can produce effects in less robust pulses i.e. the CPMG sequence. We propose a simple test for determining the nature of coherence dips and explain the effect of the pulse *shape* on the sensor response. In the following chapter we exploit our new understanding to propose new experimental protocols for enhanced sensing that are designed to mitigate or exploit the finite pulse effects elucidated in this chapter. This chapter covers work published in Lang et al. (2017) [50].

4.1 The Toggling Frame and Generalised Modulation Functions

For a nitrogen vacancy center coupled to a single nuclear spin-1/2 under dynamical decoupling control the Hamiltonian can be written as

$$\hat{H}_0(t) = -\gamma_{\mathrm{n}}\mathbf{B}\cdot\hat{\mathbf{I}} + \hat{S}_z\mathbf{A}\cdot\hat{\mathbf{I}} + \hat{H}_p(t), \tag{4.1}$$

where $\hat{S}_z = m_u|m_u\rangle\langle m_u|$ represents the NV spin qubit between the lower $m_s = 0 \equiv m_d$ level and the selected upper $m_s = \pm 1 \equiv m_u$ level. In the following we will select $m_u = +1$ for simplicity but the analysis is equivalent for a choice of $m_u = -1$. $\hat{\mathbf{I}}$ represents the nuclear spin and γ_{n} is the nuclear gyromagnetic ratio. $\mathbf{B}$ is an applied magnetic field so that $|\gamma_{\mathrm{n}}\mathbf{B}|$ is the nuclear Larmor frequency. The hyperfine field at the nucleus position $\mathbf{r}$ is $\mathbf{A}(\mathbf{r}) \equiv \mathbf{A}$. The above Hamiltonian is already presented in the frame rotating with the microwave drive frequency so that the dynamical decoupling control is described by the

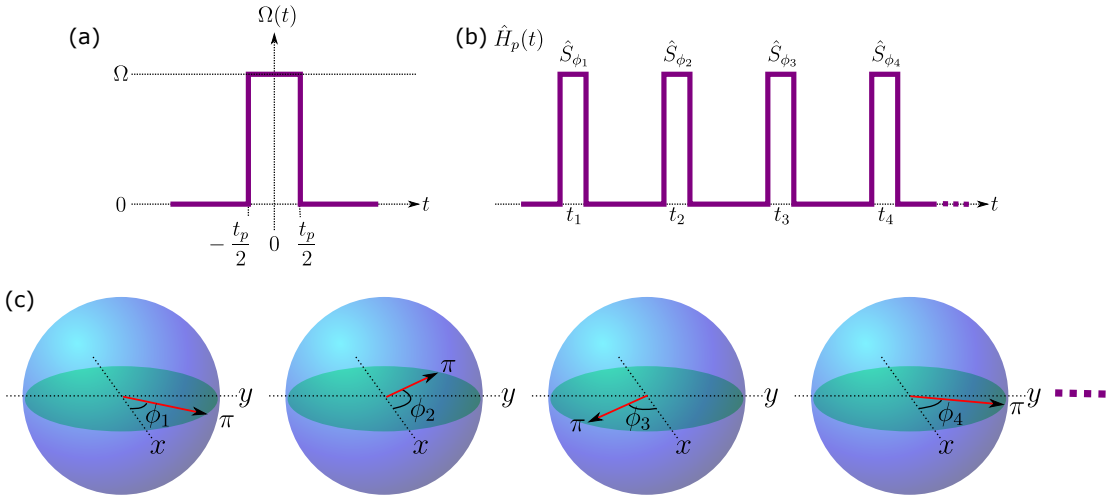

Figure 4.1: (a) Shows a square π-pulse where the pulse shape, $\Omega(t)$, is defined at the origin. For square pulses $\Omega(t) \equiv \Omega$ for $t \in [-t_p/2, t_p/2]$ and $\Omega(t) = 0$ elsewhere. For the pulse to be a π-pulse we require that $\Omega t_p = \pi$. (b) Shows the first few pulses of a sequence constructed of identical square pulses at arbitrary phases. (c) Shows the Bloch sphere representation of the applied π-pulses, illustrating the effect of the pulse phase, ϕ_m.

microwave amplitude only,

$$\hat{H}_p(t) = \sum_m^N \Omega(t - t_m)\hat{S}_{\phi_m}, \tag{4.2}$$

which consists of N pulses applied at times t_m and with phase ϕ_m for $m = 1, ..., N$. The pulse shape, assumed to be the same for all the pulses, is given by $\Omega(t)$ defined at the origin. Typically the pulse shape is modelled as an infinitesimally narrow delta-spike, $\Omega(t) = \delta(t)$. However, here we allow some finite pulse duration, t_p, and define the pulse shape $\Omega(t)$ to exist within the domain $[-t_p/2, t_p/2]$. We only require that $\int_{-t_p/2}^{t_p/2} \Omega(t)dt = \pi$ so that a complete π rotation is achieved. Figure 4.1 shows an example square pulse and how an arbitrary sequence of square pulses is constructed. We assume that all pulses in the sequence have the same shape but they rotate the sensor state about an arbitrary axis $\cos\phi\hat{\mathbf{x}} + \sin\phi\hat{\mathbf{y}}$ on the xy-plane as shown in Figure 4.1(c).

We reframe the Hamiltonian in terms of the nuclear average Hamiltonian, $\hat{H}_{\text{av}}$, and the nuclear interaction Hamiltonian, $\hat{V}$, defined below. This is to symmetrise the perturbation term as for the NV (ignoring the $m_s = -1$ state), $\hat{S}_z = |+1\rangle\langle+1| = \frac{1}{2}(\hat{\mathbb{I}} + \hat{\sigma}_z) \neq \frac{1}{2}\hat{\sigma}_z$ where $\hat{\sigma}_z$ is the usual z-Pauli matrix.

$$\hat{H}_0(t) = \left(-\gamma_{\text{n}}\mathbf{B} + \frac{1}{2}\mathbf{A}\cdot\hat{\mathbf{I}}\right) + \hat{\sigma}_z\frac{1}{2}\mathbf{A}\cdot\hat{\mathbf{I}} + \hat{H}_p(t), \tag{4.3}$$

$$\equiv \hat{H}_{\text{av}} + \hat{\sigma}_z\hat{V} + \hat{H}_p(t). \tag{4.4}$$

The average Hamiltonian is the average of the bifurcated free nuclear evolution, $\hat{H}_{\text{av}} =$

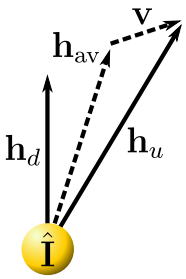

Figure 4.2: The nuclear spin-1/2, $\hat{\mathbf{I}}$, feels a magnetic field conditional on the state of the NV sensor, $\mathbf{h}_d = -\gamma_{\rm n}\mathbf{B}$ or $\mathbf{h}_u = -\gamma_{\rm n}\mathbf{B} + \mathbf{A}$. In the average Hamiltonian frame we consider the average field $\mathbf{h}_{\rm av} = -\gamma_{\rm n}\mathbf{B} + \frac{1}{2}\mathbf{A}$ and the interaction field $\mathbf{v} = \frac{1}{2}\mathbf{A}$.

$(\hat{H}_u + \hat{H}_d)/2$, and the nuclear interaction is the difference, $\hat{V} = (\hat{H}_u - \hat{H}_d)/2$, where $\hat{H}_{u,d} = (-\gamma_{\rm n}\mathbf{B} + m_{u,d}\mathbf{A}) \cdot \hat{\mathbf{I}}$ is the free nuclear Hamiltonian conditioned on the NV spin state. Fig. 4.2 shows how the conditional magnetic field felt by the nuclear spin $\mathbf{h}_{u,d}$ can represented by an average field $\mathbf{h}_{\rm av}$ and interaction field $\mathbf{v}$.

We then move to the frame rotating under $\hat{H}_p(t)$, called the toggling frame, which will produce generalised modulation functions that are extensions of the single step-modulation function used in many semi-classical models of DD [143, 36, 134] and in more recent quantum models [37]. Appendix B details a general transformation to a rotating frame. The toggling frame Hamiltonian is given by

$$\hat{H}(t) = \hat{H}_{\rm av} + \sum_{i=x,y,z} f_i(t)\hat{\sigma}_i\hat{V}, \tag{4.5}$$

where the modulation functions, $f_i(t)$, are obtained by calculating $\hat{U}_p^\dagger(t)\hat{\sigma}_z\hat{U}_p(t) \equiv \sum_{i=x,y,z} f_i(t)\hat{\sigma}_i$ with the *pulse propagator* $\hat{U}_p(t) = \hat{\mathcal{T}}\exp\left(-i\int_0^t dt'\hat{H}_p(t')\right)$. For periodic pulse sequences the move to this rotating frame does not affect our measurement outcomes as the two frames coincide at stroboscopic times, $\hat{U}_p(N_pT) = \hat{\mathbb{I}}$ so $|\psi_{\hat{H}_0(t)}(N_pT)\rangle = |\psi_{\hat{H}(t)}(N_pT)\rangle$.

Presently, will we consider square microwave pulses of width t_p and height $\Omega = \pi/t_p$. (See Section 4.5 for the effect of different pulse shapes.) We require the pulse propagator for square pulses to obtain the generalised modulation functions. Outside of the pulses $\hat{H}_p(t) = 0$ so the dynamics is trivial. During a square pulse the Hamiltonian is non-zero but still static so we can easily construct the pulse propagator. During the m-th pulse say, i.e at $t = t_m + t'$ for $t' \in [-t_p/2, t_p/2]$, the pulse propagator is given by

$$\hat{U}_p(t') = \exp(-i\Omega\hat{S}_{\phi_m}(t' + t_p/2))(-i\hat{\sigma}_{\phi_{m-1}})(-i\hat{\sigma}_{\phi_{m-2}})...(-i\hat{\sigma}_{\phi_1})(-i\hat{\sigma}_{\phi_1}), \tag{4.6}$$

where the $(-i\hat{\sigma}_{\phi_{m'<m}}) \equiv \exp(-i\Omega\hat{S}_{\phi_{m'<m}}t_p)$ terms account for the completed π-pulses that

precede the m-th pulse. Rotating to the toggling frame using $\hat{U}_p(t')$ then gives

$$\hat{U}_p^\dagger(t')\hat{\sigma}_z\hat{U}_p(t') = (-1)^m \sin\Omega t'\hat{\sigma}_z + \cos\Omega t'\hat{\sigma}_{\varphi_m}. \tag{4.7}$$

Note that a new phase, $\varphi_m = (-1)^{m+1}(\phi_m + \pi/2) + 2\sum_{m'<m}^{m-1}(-1)^{m'+1}\phi_{m'}$ has been introduced in Eq. (4.7) and results from the interplay between the different pulses and accounts for the specific pulse phase choices used in the DD sequence. Thus the modulation functions at $t' = t - t_m$ are

$$f_x(t') = \cos\Omega t' \cos\varphi_m, \tag{4.8}$$

$$f_y(t') = \cos\Omega t' \sin\varphi_m, \tag{4.9}$$

$$f_z(t') = (-1)^m \sin\Omega t'. \tag{4.10}$$

Between the pulses $f_{x,y}(t) = 0$ and $f_z(t) = \pm 1$ as a consequence of each pulse completing an exact π-rotation. These generalised modulation functions, published in Lang et al. 2017 [50], are a key result of this work and are essential for accurately modelling the full sensor coherence response under finite-duration-pulse control.

Figure 4.3(a,b)(i) shows the square-pulse CPMG and XY8 sequences and their generalised modulation functions. They both have the same parallel modulation function, $f_z(t)$, as this is determined by the pulse shape and spacing only. They differ in their perpendicular modulation functions, $f_{x,y}(t)$, as this encodes the pulse phase information. In the limit of infinitesimal pulse widths ($t_p \to 0$) the perpendicular modulation functions vanish and the parallel modulation function becomes the step-modulation function seen in many semi-classical studies [143, 36, 37, 134]. Our inclusion of the finite pulse duration smooths this step and introduces the perpendicular modulation functions which are essential for understanding finite-duration-pulse effects.

4.2 The Floquet Hamiltonian

For a DD sequence made up of N_p repetitions of a basic pulse unit with period T the toggling frame Hamiltonian, Eq. (4.5), is periodic so we can apply Floquet theory. From this periodic Hamiltonian we can construct the associated Floquet Hamiltonian that exists in the larger Floquet space (as described in Sec. 2.4.3). The Floquet space Hamiltonian,

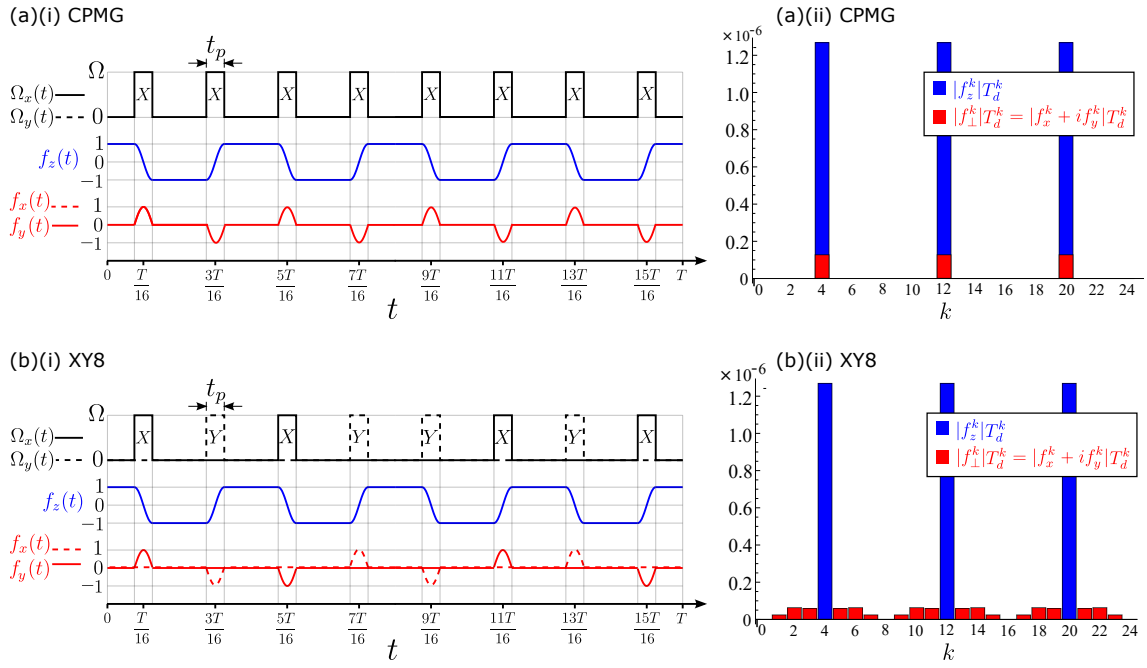

Figure 4.3: Parts (i) show the square pulse microwave amplitudes ($\Omega_x(t) = \sum_m \Omega(t - t_m)\cos\phi_m$, $\Omega_y(t) = \sum_m \Omega(t - t_m)\sin\phi_m$) and modulation functions ($f_i(t)$) for the (a) CPMG and (b) XY8 pulse sequences. They both share the same parallel modulation function, $f_z(t)$, but their difference in pulse phases is encoded into the perpendicular modulation functions, $f_{x,y}(t)$. Parts (ii) show the Fourier amplitudes of the modulation functions, $f_i^k = \frac{1}{T}\int_0^T f_i(t)\exp(-ik\omega t)dt$ where $\omega = 2\pi/T$, weighted by the resonant period, $T_d^k = k \times 2\pi/\omega_{\text{av}}$. The parallel Fourier amplitudes are f_z^k and the perpendicular Fourier amplitudes are represented as a single quantity, $f_\perp^k = f_x^k + if_y^k$. For $t_p = 0$ the perpendicular modulation functions vanish and thus so do the perpendicular Fourier amplitudes whilst the parallel modulation function becomes the singular stepped-modulation function common in DD analysis.

$\hat{H}^F$, has elements

$$\langle\langle m_s,\alpha,m|\hat{H}^F|m_s',\alpha',m'\rangle\rangle = \frac{1}{T}\int_0^T \langle m_s,\alpha|\hat{H}(t)|m_s',\alpha'\rangle\, e^{-i(m-m')\omega t}dt + m\omega\delta_{m_s m_s'}\delta_{\alpha\alpha'}\delta_{mm'}, \tag{4.11}$$

$$= \langle m_s,\alpha|\hat{H}_{\rm av}|m_s',\alpha'\rangle + \sum_i f_i^{m-m'}\langle m_s,\alpha|\sigma_i\hat{V}|m_s',\alpha'\rangle + m\omega\delta_{m_s m_s'}\delta_{\alpha\alpha'}\delta_{mm'}, \tag{4.12}$$

where $\omega = 2\pi/T$ is the DD frequency and double angle brackets are used to distinguish Floquet space from the original Hilbert space. The original spin Hilbert space is spanned by the NV qubit states $|m_s = 0, +1\rangle$ and the nuclear average Hamiltonian states $|\alpha = \uparrow,\downarrow\rangle$. Floquet space is the product space of the original spin Hilbert space and a Fourier space spanned by $|m\rangle$ for $m \in \mathbb{Z}$ so that the Floquet space is spanned by $|m_s,\alpha,m\rangle\rangle$. (Fourier space is the space of all square integrable functions with period, T.) The Floquet space Hamiltonian is infinite but time-independent as the modulation functions have been replaced by their Fourier amplitudes, $f_i^k = \frac{1}{T}\int_0^T f_i(t)\exp(-ik\omega t)dt$. These Fourier amplitudes are shown for the CPMG and XY8 sequences in Fig. 4.3 parts (ii).

The Fourier amplitudes encode information about the specific sequence choice into the Floquet Hamiltonian. For instance see Fig. 4.3, for CPMG the perpendicular modulation functions share the same periodicity as the parallel modulation function and thus have the same resonances (although at these have different strengths, see Fig. 4.3(a)(ii)). For XY8 however, the perpendicular functions have a period four times longer than the parallel modulation function and thus contain new resonances at different frequencies (see Fig. 4.3(b)(ii)). As we will see the strength of these resonances (the Fourier amplitudes) determines the width of the quasienergy spectrum avoided crossings and thus the strength of the coherence dips. A simple Fourier analysis of the sequence modulation functions can thus be used to quickly estimate the relative strengths of the coherence dips. However, to obtain analytic expressions for the full coherence response, Floquet analysis is necessary.

The diagonal elements of $\hat{H}^F$ give the *unperturbed* quasienergy spectrum,

$$\epsilon_0 = \pm\omega_{\rm av}/2 + m\omega, \tag{4.13}$$

for $m \in \mathbb{Z}$. We have used here that $\hat{H}_{\rm av} = \omega_{\rm av}\hat{I}_z$ in the average Hamiltonian basis and $f_z^0 = \frac{1}{T}\int_0^T f_z(t)dt = 0$ as expected for an effective dynamical decoupling sequence. As seen in Fig. 4.4 the unperturbed quasienergy spectrum has level crossings between the

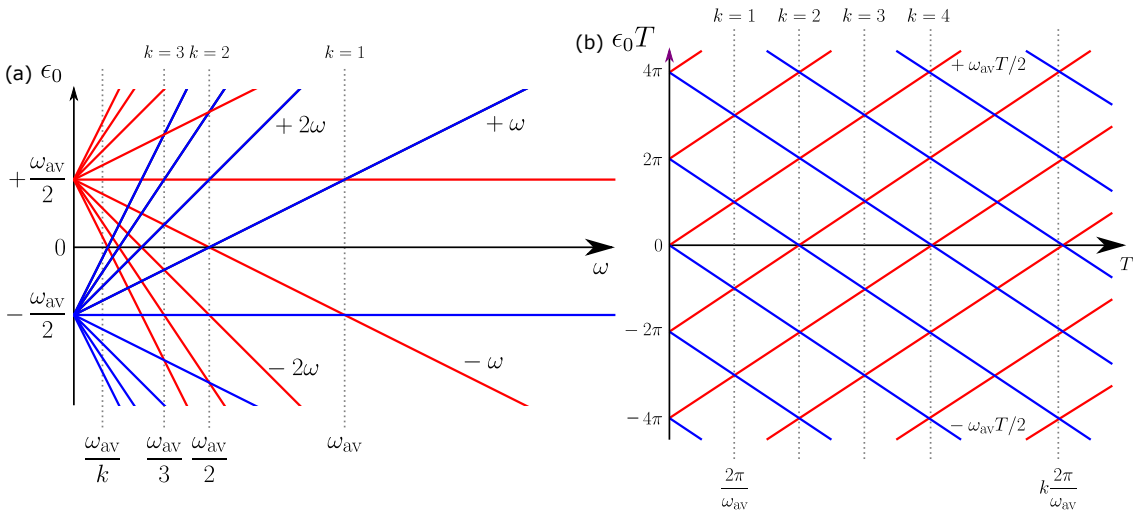

Figure 4.4: (a) The unperturbed Floquet spectrum, $\epsilon_0 = \pm\omega_{\rm av} + m\omega$, has level crossings when the DD frequency $\omega = \omega_{\rm av}/k$. (b) It is also possible to represent the spectrum under a scan of the DD period, $T = 2\pi/\omega$, where the spectrum $\epsilon_0 T = \pm\omega_{\rm av}T/2 + m2\pi$ has crossings at $T = k \times 2\pi/\omega_{\rm av}$. We study the off-diagonal elements of the Floquet Hamiltonian to see if the level crossing degeneracies will be lifted to form avoided crossings.

$\epsilon_0 = \omega_{\rm av}/2 + m\omega$ and $\epsilon_0 = -\omega_{\rm av}/2 + (m+k)\omega$ levels when $\omega = \omega_{\rm av}/k$ for $k \in \mathbb{Z}$ (or equivalently $T = k \times 2\pi/\omega_{\rm av}$). These level crossings reduce the effective energy gap between the average Hamiltonian states allowing the weak perturbation, $A_\perp$, to induce mixing in the energy levels. This is manifested as the level crossings of the unperturbed system becoming avoided crossings when the perturbation is introduced.

When $\omega \approx \omega_{\rm av}/k$ for $k \in \mathbb{Z}$ there is a level crossing between the unperturbed states $|m_u, \uparrow, m\rangle\rangle, |m_u, \downarrow, m+k\rangle\rangle, |m_d, \uparrow, m\rangle\rangle, |m_d, \downarrow, m+k\rangle\rangle$, $\forall m$. At the level crossings we consider only the off-diagonal terms that couple these levels to each other - in the weak coupling regime ($|\mathbf{A}| \ll \omega_{\rm av}$) the perturbation coupling these states to other states is ignored as the energy gap is too large for the small perturbation to have an effect. The Floquet Hamiltonian can thus be collected into a block diagonal form, $\hat{H}^F = \bigoplus_{m=-\infty}^{\infty} \hat{H}_{\rm B}^m$, with blocks

$$\hat{H}_{\rm B}^m = \begin{bmatrix} \omega_{\rm av}/2 + m\omega & f_z^{-k}A_\perp/2 & 0 & (f_x^{-k} - if_y^{-k})A_\perp/2 \\ f_z^k A_\perp/2 & -\omega_{\rm av}/2 + (m+k)\omega & (f_x^k - if_y^k)A_\perp/2 & 0 \\ 0 & (f_x^{-k} + if_y^{-k})A_\perp/2 & \omega_{\rm av}/2 + m\omega & -f_z^{-k}A_\perp/2 \\ (f_x^k + if_y^k)A_\perp/2 & 0 & -f_z^k A_\perp/2 & -\omega_{\rm av}/2 + (m+k)\omega \end{bmatrix}, \tag{4.14}$$

where we have used that $\hat{V} = A_\perp \hat{I}_x + A_\parallel \hat{I}_z$ in the nuclear average Hamiltonian frame and that $f_i^0 = 0$ as seen in Fig. 4.3. Figure 4.5 presents a schematic of how the Floquet Hamiltonian is constructed from a periodic Hamiltonian and how it can be collected into

block diagonal form. Formally, this collection into block diagonal form involves a unitary transformation in Floquet space that swaps pairs of states into the desired blocks. The transformation only affects the Fourier index, e.g. $|m_s, \alpha, m\rangle\rangle \rightarrow |m_s, \alpha, m+k\rangle\rangle$, and not the original Hilbert space states. Transformations like this are equivalent to transforming to a rotating frame in the original Hilbert space using an associated *periodic* unitary operator [146]. We are free to make this transformation as this periodic unitary operator equals the identity at stroboscopic times and thus does not affect our experimental measurement. This justifies our collection of the Floquet Hamiltonian into block diagonal form.

Now consider a static effective Hamiltonian that correctly describes the evolution at stroboscopic times, $\hat{U}(N_p T) = \exp(-i\hat{H}_{\text{eff}} N_p T)$. This effective Hamiltonian is static but can still be considered to be periodic, with period T. Thus, we can construct a second Floquet Hamiltonian associated with this static effective Hamiltonian. This effective Floquet Hamiltonian also has a block-diagonal form, as illustrated in Fig. 4.5,

$$\hat{H}^F_{\text{eff}} = \bigoplus_{m=-\infty}^{\infty} \hat{H}_{\text{eff}} + m\omega\hat{\mathbb{I}}, \tag{4.15}$$

which upon comparison with Eq. 4.14 reveals the effective Hamiltonian $\hat{H}_{\text{eff}} \equiv \hat{H}^0_{\text{B}}$ (valid when $T \approx k \times 2\pi/\omega_{\text{av}}$).

$$\hat{H}_{\text{eff}} = \begin{bmatrix} \omega_{\text{av}}/2 & f_z^{-k}A_\perp/2 & 0 & (f_x^{-k} - if_y^{-k})A_\perp/2 \\ f_z^k A_\perp/2 & -\omega_{\text{av}}/2 + k\omega & (f_x^k - if_y^k)A_\perp/2 & 0 \\ 0 & (f_x^{-k} + if_y^{-k})A_\perp/2 & \omega_{\text{av}}/2 & -f_z^{-k}A_\perp/2 \\ (f_x^k + if_y^k)A_\perp/2 & 0 & -f_z^k A_\perp/2 & -\omega_{\text{av}}/2 + k\omega \end{bmatrix}. \tag{4.16}$$

The derivation of this effective Hamiltonian is a key result of this chapter and is valid for any pulse sequence choice. It is later used to derive the full coherence response under finite-duration-pulse control.

For sequences like CPMG and XY8 the parallel modulation function is even on T meaning $f_z^{-k} = f_z^k$ and the perpendicular modulation functions are odd on T meaning $f_{x,y}^{-k} = -f_{x,y}^k$. Using these properties, and defining $f_\perp^k = f_x^k + if_y^k$ the effective Hamiltonian can be written in the form

$$\hat{H}_{\text{eff}} = (\omega_{\text{av}} - k\omega)\hat{I}_z + f_z^k \hat{\sigma}_z A_\perp \hat{I}_x + |f_\perp^k|\hat{\sigma}_{(\phi_\perp^k - \frac{\pi}{2})} A_\perp \hat{I}_y, \tag{4.17}$$

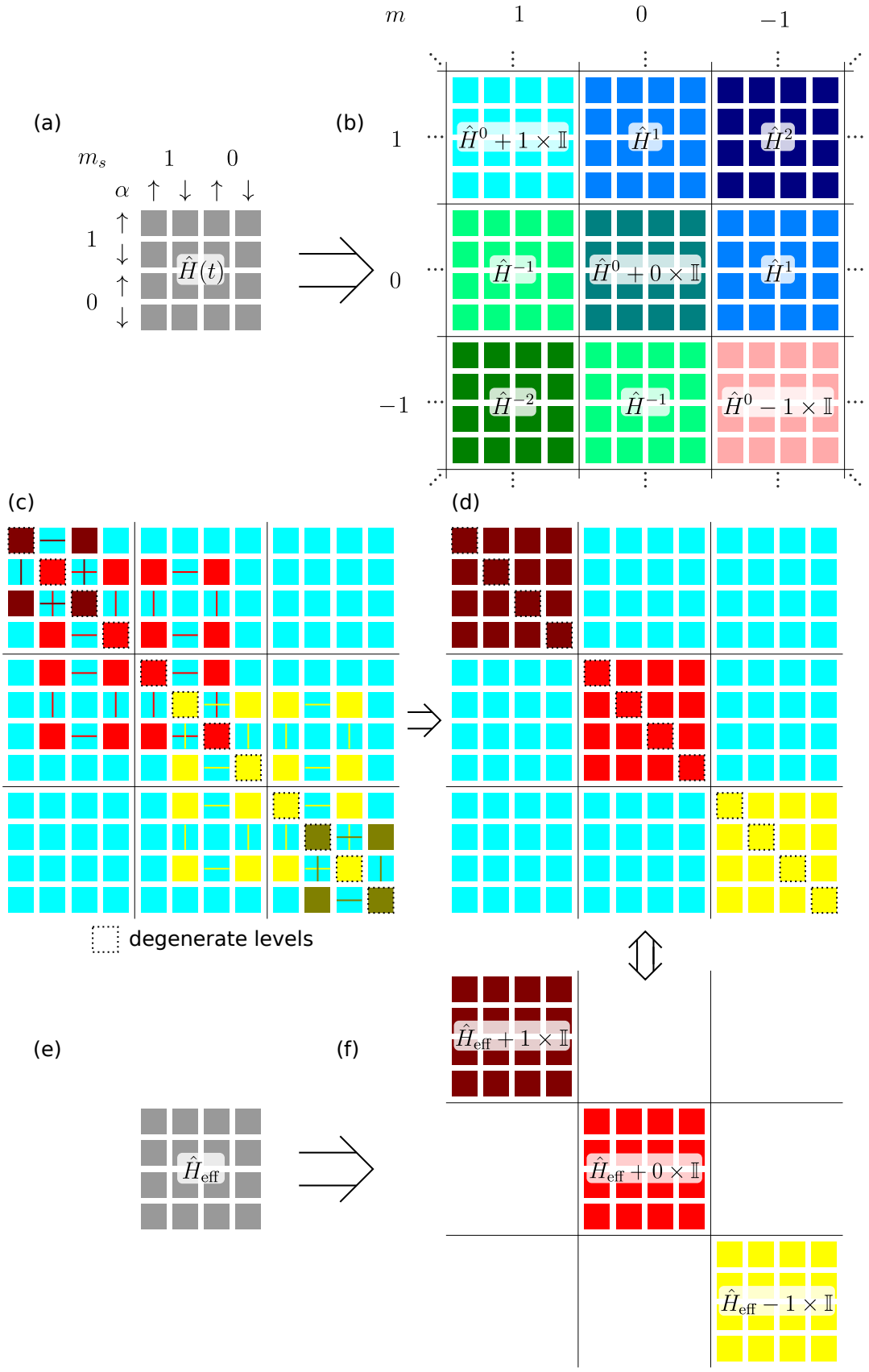

Figure 4.5: Schematic illustrating the Floquet Hamiltonian method. (a) A periodic Hamiltonian in a Hilbert space with basis $|m_s, \alpha\rangle$. (b) The corresponding Floquet Hamiltonian with the basis $|m_s, \alpha, m\rangle\rangle$. (c) and (d) At degeneracies in the unperturbed quasienergy spectrum the Floquet Hamiltonian can be rearranged into block form as only the off-diagonal terms connecting degenerate levels are significant. (e) A static effective Hamiltonian can also be expressed in Floquet space as shown in (f). The effective Hamiltonian is revealed by comparing (d) and (f).

where we have omitted a trivial $\frac{k\omega}{2}\hat{\mathbb{I}}$ term. It is interesting to compare the effective Hamiltonian against the original time dependent Hamiltonian, $\hat{H}(t) = \omega_{\text{av}}\hat{I}_z + \sum_i f_i(t)\hat{\sigma}_i(A_\perp\hat{I}_x + A_\parallel\hat{I}_z)$. The average Hamiltonian energy splitting ω_{av} is replaced by a rescaled $\omega_{\text{av}} - k\omega$ which vanishes when $\omega = \omega_{\text{av}}/k$ allowing the small interaction, $A_\perp$, to introduce mixing of the average Hamiltonian states. This mixing is heralded by an avoided crossing in the Floquet quasienergy spectrum. The level crossings in the unperturbed Floquet quasienergy spectra become avoided crossing wherever f_z^k or $f_\perp^k$ are non-zero. If $f_z^k \neq 0$ there is mixing between the states $|m_s = 0, \uparrow\rangle \leftrightarrow |m_s = 0, \downarrow\rangle$ and $|m_s = +1, \uparrow\rangle \leftrightarrow |m_s = +1, \downarrow\rangle$, i.e. the NV levels are not directly mixed, only dephased as expected in DD and the dips associated with these avoided crossings are the expected dips from DD based sensing. If $f_\perp^k \neq 0$ there is mixing between the states $|m_s = 0, \uparrow\rangle \leftrightarrow |m_s = +1, \downarrow\rangle$ and $|m_s = +1, \uparrow\rangle \leftrightarrow |m_s = 0, \downarrow\rangle$ which directly mixes the NV spin states. This behaviour is not expected from DD protocols and the mixing is introduced during the short duration of each pulse. The new dips associated with these avoided crossings are the so-called spurious dips caused by the finite pulse duration. Note that when $t_p = 0$, the perpendicular Fourier series, $f_\perp^k$, vanishes removing all spurious effects, whereas the parallel Fourier series, f_z^k, does not, recovering the DD response under ideal delta-spike pulses. Figure 4.6 shows how to model spurious dips for the XY8 sequence and how including a finite pulse duration opens new avoided crossings in the Floquet spectrum.

Here we have described the source of finite-duration-pulse effects and presented an effective Hamiltonian that governs the stroboscopic evolution however we still seek to obtain an analytic expression for the spurious (and expected) dips in the sensor coherence profile. The coherence response of the sensor is modelled by calculating the expectation value of the measurement, $\langle\hat{\sigma}_x\rangle$. As the nuclear spin is initially assumed to be in a mixed state we will work with the density matrix formalism. The initial state of the system can be represented as $\rho_0 = \frac{1}{2}(\hat{\mathbb{I}} + \hat{\sigma}_x) \otimes \frac{1}{2}\hat{\mathbb{I}}$ which gives the NV in the initial pure state $|\psi_0\rangle = \frac{1}{\sqrt{2}}(|u\rangle + |d\rangle)$ and the nuclear spin in a thermally mixed state $\rho_{\text{n}} = \frac{1}{2}\hat{\mathbb{I}}$. This density matrix evolves under the stroboscopic evolution to $\rho(N_pT) = \hat{U}(N_pT)\rho_0\hat{U}^\dagger(N_pT)$ which then gives the coherence response via $\mathcal{L}(N_pT) = \text{Tr}\{\hat{\sigma}_x\rho(t)\}$. By diagonalising the effective Hamiltonian we can express the coherence response in terms of the Floquet quasienergies and modes.

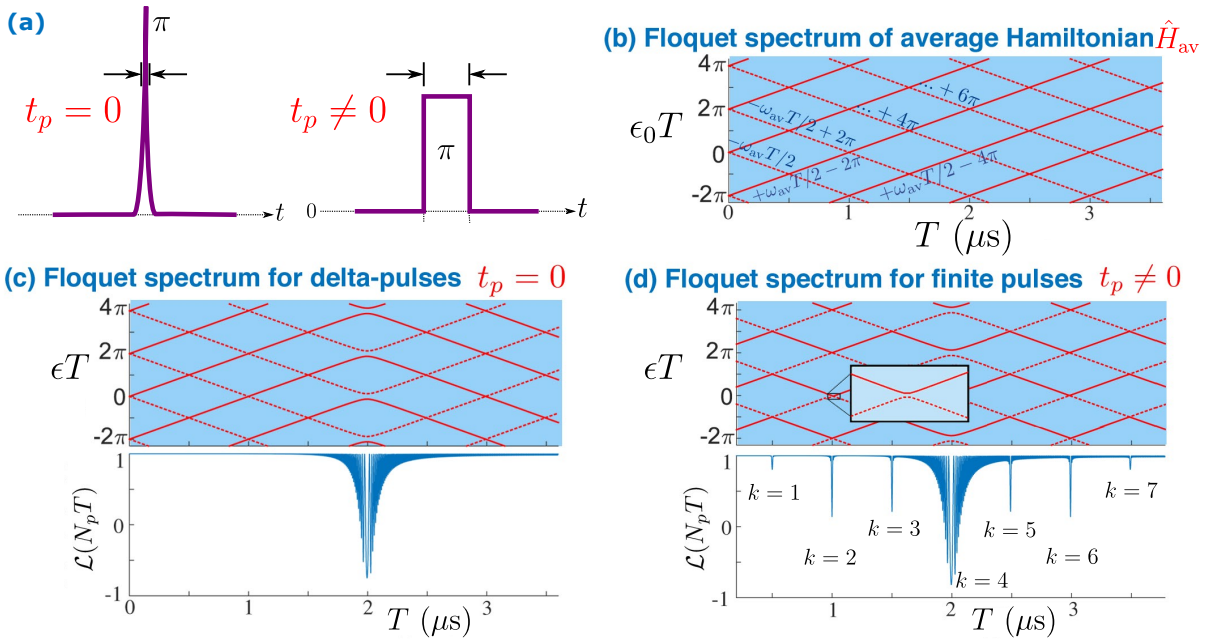

Figure 4.6: **(a)** Typically microwave pulses are modelled as delta-spikes with zero duration. Allowing the pulse to have some finite width, t_p, opens new avoided crossings in the Floquet quasienergy spectrum and creates spurious signals as demonstrated here. **(b)** The unperturbed Floquet eigenspectrum is given by the nuclear average Hamiltonian: $\pm\omega_{\rm av}$, but shows the characteristic Floquet structure of dressed states shifted by integer multiples of $\omega = 2\pi/T$. There are level crossings when $T = k \times 2\pi/\omega_{\rm av}$. In this case, the level degeneracies correspond to true crossings. **(c)** The effect of the DD pulses, for the ideal $t_p = 0$ case, is to turn some crossings into avoided crossings. A coherence dip, with its strength determined by the width of the crossing, can then be seen. **(d)** For the general $t_p \neq 0$ case, all remaining crossings can potentially become avoided crossings: these are typically narrow, and yield sharp weaker dips. For numerical simulations here: $\omega_{\rm av} = 2$ MHz$\times 2\pi$ and $A_\perp = 200$ kHz$\times 2\pi$. The pulse sequence is XY8 with $N_p = N/8 = 60$ repetitions. The finite pulses have height $\Omega = 20$ MHz $\times\, 2\pi$ and duration $t_p = \pi/\Omega$.

4.3 The XY8 Sequence

First let us study the XY8 dynamical decoupling sequence where spurious dips were first observed [42] and where the spurious and expected signals appear separately (a consequence of the parallel and perpendicular Fourier amplitudes appearing separately, see Fig. 4.3). Figure. 4.6(d) shows the NV detection of ^{13}C under XY8 control. This has been simulated numerically by directly propagating the time-dependent Hamiltonian, Eq. (4.1). Spurious dips appear before and after the stronger expected signal. We will derive analytic expressions for the coherence response at expected and spurious dips.

The XY8 sequence is designed to be robust against pulse errors [152, 141, 48]. After initialising the sensor state to the superposition $|\psi_0\rangle = (|u\rangle + |d\rangle)/\sqrt{2}$ the XY8 sequence is described by: $\tau - \pi_x - 2\tau - \pi_y - 2\tau - \pi_x - 2\tau - \pi_y - 2\tau - \pi_y - 2\tau - \pi_x - 2\tau - \pi_y - 2\tau - \pi_x - \tau$, with a sequence period $T = 16\tau + 8t_p$. The final coherence measurement is taken along the x-axis. The pulse sequence, modulation functions and Fourier amplitudes are shown in Fig. 4.3(b)(i) and (ii). The characteristic coherence dips appear when the DD period $T = T^k_{\text{dip}} = k \times 2\pi/\omega_{\text{av}}$ with the expected and spurious signals appearing at distinct values of k.

4.3.1 XY8 Expected Coherence Dips: $f_z^k \neq 0$

When $T \approx k \times 2\pi/\omega_{\text{av}}$, with k such that $f_z^k \neq 0$ but $f_\perp^k = 0$ (from Fig. 4.3(b)(ii) we see this is $k = 4, 12, 20, ...$) the effective Hamiltonian is formed of two 2-D subspaces and can be diagonalised analytically,

$$\hat{H}_{\text{eff}} = \begin{bmatrix} \omega_{\text{av}}/2 & f_z^k A_\perp/2 & 0 & 0 \\ f_z^k A_\perp/2 & -\omega_{\text{av}}/2 + k\omega & 0 & 0 \\ 0 & 0 & \omega_{\text{av}}/2 & -f_z^k A_\perp/2 \\ 0 & 0 & -f_z^k A_\perp/2 & -\omega_{\text{av}}/2 + k\omega \end{bmatrix} = \hat{D}\hat{\Lambda}\hat{D}^{-1}, \tag{4.18}$$

$$\hat{D} = \begin{bmatrix} \cos\frac{\theta^F}{2} & -\sin\frac{\theta^F}{2} & 0 & 0 \\ \sin\frac{\theta^F}{2} & \cos\frac{\theta^F}{2} & 0 & 0 \\ 0 & 0 & \cos\frac{\theta^F}{2} & \sin\frac{\theta^F}{2} \\ 0 & 0 & -\sin\frac{\theta^F}{2} & \cos\frac{\theta^F}{2} \end{bmatrix}, \quad \hat{\Lambda} = \begin{bmatrix} \epsilon & 0 & 0 & 0 \\ 0 & -\epsilon & 0 & 0 \\ 0 & 0 & \epsilon & 0 \\ 0 & 0 & 0 & -\epsilon \end{bmatrix}, \tag{4.19}$$

where $\epsilon = \frac{1}{2}\sqrt{(\omega_{\text{av}} - k\omega)^2 + (f_z^k A_\perp)^2}$ and $\theta^F = \arctan(f_z^k A_\perp/(\omega_{\text{av}} - k\omega))$. The system Floquet quasienergies and Floquet modes *are* the eigenenergies and eigenstates of the

effective Hamiltonian and can be read directly from $\hat{\Lambda}$ and $\hat{D}$. It is important to remember that although, for a particular DD period, T, the Floquet quasienergies and modes are time independent, they are still parametrised by the period through $\omega = 2\pi/T$.

The effective Hamiltonian here has a pure-dephasing form $\hat{H}_{\text{eff}} = |u\rangle\langle u| \otimes \hat{H}_u^{\text{eff}} + |d\rangle\langle d| \otimes \hat{H}_d^{\text{eff}}$ where the conditional nuclear Hamiltonian, $\hat{H}_{u,d}^{\text{eff}} = \mathbf{h}_{u,d}^{\text{eff}} \cdot \hat{\mathbf{I}}$, is governed by an effective field $\mathbf{h}_{u,d}^{\text{eff}} = 2\epsilon(\pm \sin\theta^F, 0, \cos\theta^F)$. This is the same as in the case of delta-spike pulses described in Section 3.2.

The Floquet modes and quasienergies can be used to express the stroboscopic evolution, $\hat{U}(N_pT) = \hat{D}\exp(-i\hat{\Lambda}N_pT)\hat{D}^{-1}$, and thus the density matrix $\rho(N_pT) = \hat{U}(N_pT)\rho_0\hat{U}^\dagger(N_pT)$ where $\rho_0 = \frac{1}{2}(\hat{\mathbb{I}} + \sigma_x) \otimes \frac{1}{2}\hat{\mathbb{I}}$. An analytic expression for the coherence is then obtained by evaluating $\mathcal{L}(N_pT) = \text{Tr}\{\hat{\sigma}_x\rho(N_pT)\}$:

$$\mathcal{L}(N_pT) = 1 - 2\sin^2(\epsilon N_pT)\sin^2(\theta^F), \tag{4.20}$$

which has the same form as the expression previously derived, Eq. (3.22).

Figure 4.7(b) shows a zoom of an XY8, $k = 4$, expected coherence dip similar to that seen in Fig. 4.6 and the associated quasienergy avoided crossing. This dip appears at $T = 4 \times 2\pi/\omega_{\text{av}}$ where $f_z^4 \neq 0$ as seen in Fig. 4.3(b)(ii). The analytic expression derived above, Eq. (4.20) is tested against a numerical simulation of the coherence profile obtained by directly propagating the time-dependent Hamiltonian, Eq. (4.1). The analytic expression shows a good fit to numerics.

The derived expression, Eq. (4.20), can be split into a pulse-number independent coherence envelope $\mathcal{L}_{\text{env}}(T) = 1 - 2\sin^2(\theta^F)$ and the superimposed oscillations. The full coherence is bound by $\mathcal{L}_{\text{env}}(T) \leq \mathcal{L}(N_pT) \leq 1$. At the dip, where $T = T_{\text{dip}}^k = k \times 2\pi/\omega_{\text{av}}$ or equivalently $\omega = \omega_{\text{av}}/k$, the conditional effective fields, $\mathbf{h}_{u,d}^{\text{eff}}$, are anti-parallel, with $\theta^F = \pm\pi/2$. Here, the envelope reaches its minimal value of $\mathcal{L}_{\text{env}}(T) = -1$. The quasienergy at the dip is given by $\epsilon = \pm\frac{1}{2}|f_z^k A_\perp|$ so the avoided crossing width is $\delta_\epsilon = |f_z^k A_\perp|$. This avoided crossing width, along with the the number of applied pulses, determines the depth of the coherence dip, $\mathcal{L}_{\text{dip}} = 1 - 2\sin^2(\frac{1}{2}N_p\delta_\epsilon T_{\text{dip}}^k)$.

As the coherence dip only appears when the average Hamiltonian states are mixed, i.e. at the avoided crossing, the resolution or width of the coherence dip is also delicately determined by the avoided crossing width. Narrower avoided crossings produce sharper coherence dips. Recent theory proposals and experiments make use of tunable decoupling sequences to gain control over the effective coupling to nuclear spins [39, 93, 94, 95]. This

involves the application of sequences made of composite pulses with adjustable inter-pulse spacing (i.e. not the standard regular spacing we discuss here) so that one can tune the effective coupling to nuclear spins for increased resolution or to isolate nuclear spins. In the Floquet picture this amounts to tuning $|f_z^k|$ to open or close avoided crossings, i.e. augmenting or diminishing the effective coupling to nuclear spins and thus the width of experimental signals. By choosing $|f_z^k|$ to be small one can sharpen a selected coherence dip allowing for better resolution between isolated nuclear spins. The number of pulses that can be applied is constrained by the T_2 coherence time so the minimal limit for $|f_z^k|$ is determined by the requirement that the dip still obtain a visible contrast after the maximum number of pulses.

4.3.2 XY8 Spurious Coherence Dips: $f_\perp^k \neq 0$

When $T \approx k \times 2\pi/\omega_{\text{av}}$, with k such that $f_\perp^k = |f_\perp^k| e^{i\phi_\perp^k} \neq 0$ but $f_z^k = 0$, the effective Hamiltonian separates into a different pair of 2-D subspaces and can again be diagonalised analytically to find the Floquet quasienergies and modes,

$$\hat{H}_{\text{eff}} = \begin{bmatrix} \omega_{\text{av}}/2 & 0 & 0 & (f_\perp^k)^* A_\perp/2 \\ 0 & -\omega_{\text{av}}/2 + k\omega & -(f_\perp^k)^* A_\perp/2 & 0 \\ 0 & -f_\perp^k A_\perp/2 & \omega_{\text{av}}/2 & 0 \\ f_\perp^k A_\perp/2 & 0 & 0 & -\omega_{\text{av}}/2 + k\omega \end{bmatrix} = \hat{D}\hat{\Lambda}\hat{D}^{-1} \tag{4.21}$$

$$\hat{D} = \begin{bmatrix} \cos\frac{\theta_s^F}{2} & 0 & 0 & -\sin\frac{\theta_s^F}{2} e^{-i\phi_s^F} \\ 0 & \cos\frac{\theta_s^F}{2} & -\sin\frac{\theta_s^F}{2} e^{-i\phi_s^F} & 0 \\ 0 & \sin\frac{\theta_s^F}{2} e^{i\phi_s^F} & \cos\frac{\theta_s^F}{2} & 0 \\ \sin\frac{\theta_s^F}{2} e^{i\phi_s^F} & 0 & 0 & \cos\frac{\theta_s^F}{2} \end{bmatrix}, \quad \hat{\Lambda} = \begin{bmatrix} \epsilon_s & 0 & 0 & 0 \\ 0 & -\epsilon_s & 0 & 0 \\ 0 & 0 & \epsilon_s & 0 \\ 0 & 0 & 0 & -\epsilon_s \end{bmatrix}, \tag{4.22}$$

where $\epsilon_s = \frac{1}{2}\sqrt{(\omega_{\text{av}} - k\omega)^2 + (|f_\perp^k| A_\perp)^2}$, $\theta_s^F = \arctan(|f_\perp^k| A_\perp/(\omega_{\text{av}} - k\omega))$ and $\phi_s^F = \phi_\perp^k$. The Floquet quasienergies and modes can, again, be read directly out of $\hat{D}$ and $\hat{\Lambda}$. It is interesting here that Floquet modes directly mix the sensor u and d states and the effective Hamiltonian is not in a pure dephasing form. This is perhaps the key qualitative difference between the spurious and expected dynamics.

These Floquet parameters are used to express the coherence profile of a spurious dip

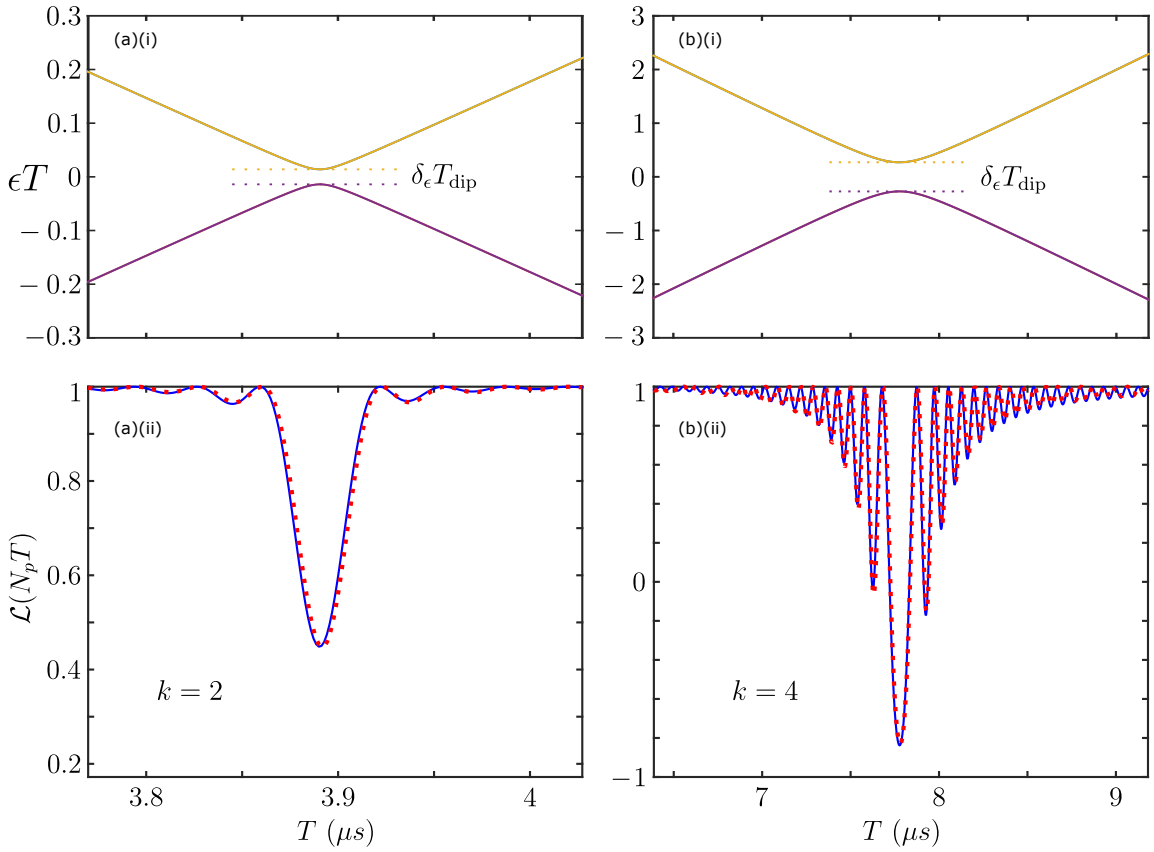

Figure 4.7: Simulations of the NV detection of a single ^{13}C with XY8. Parts (i) show the avoided crossings in the Floquet spectrum associated with the (a) $k = 2$ spurious dip and (b) $k = 4$ expected dip. Notice, due to the different axis scaling that the spurious avoided crossing is $\sim 20\times$ narrower than the expected avoided crossing. Parts (ii) shows a good fit between the NV coherence trace computed by direct numeric propagation of the time-dependent Hamiltonian, Eq. (4.1), (red dots) and our derived analytic expressions for the coherence (blue lines) (a) the $k = 2$ spurious dip with Eq. (4.23) and (b) the $k = 4$ expected dip with Eq. (4.20). Notice that the spurious dip is much narrower than the expected dip, in conjunction with its narrower avoided crossing. (Again note the different axis scaling.) For numerical simulations here a magnetic field, $B_z = 480$ G, is applied along the crystal axis whilst the carbon spin is hyperfine coupled to the NV with strength $[A_x, A_z] = [35, 0]$ kHz$\times 2\pi$. The square pulses applied have width $t_p = 100$ ns and for the spurious signal $N_p = N/8 = 60$ sequence repetitions were applied whilst for the expected signal $N_p = 30$.

by evaluating $\mathcal{L}(N_pT) = \mathrm{Tr}\{\hat{\sigma}_x\rho(N_pT)\}$ as before:

$$\mathcal{L}_s(N_pT) = 1 - 2\sin^2(N_p\epsilon_s T)\sin^2(\theta_s^F)\cos^2(\phi_s^F), \tag{4.23}$$

which is shown, in Fig. 4.7(a), to fit well to numerics. This expression is qualitatively similar to that of the expected coherence dips, Eq. (4.20), except for the dependence on $\phi_s^F = \phi_\perp^k$. This dependence arises due to the direct mixing, not dephasing, of the sensor spin levels. This expression represents the first accurate model of spurious coherence dips.

Figure 4.7(a) shows a zoom of an XY8, $k = 2$, spurious coherence dip similar to that seen in Fig. 4.6 and the associated quasienergy avoided crossing. This dip appears at $T = 2 \times 2\pi/\omega_{\mathrm{av}}$ where $f_\perp^2 \neq 0$ as seen in Fig. 4.3(b)(ii). The analytic expression derived above, Eq. (4.23) is tested against a numerical simulation of the coherence profile obtained by directly propagating the time-dependent Hamiltonian, Eq. (4.1), and shows a good fit to numerics. We see that the spurious avoided crossing is much narrower than the expected avoided crossing resulting in a much sharper coherence dip.

The coherence profile is again bounded by a coherence envelope $\mathcal{L}_s^{\mathrm{env}}(T) = 1-2\sin^2(\theta_s^F)\cos^2(\phi_s^F)$ and has superimposed oscillations determined by N_p. The key difference between the spurious and expected dips is the dependence on the phase $\phi_s^F = \phi_\perp^k$. At the dip the envelope only reaches a minimum of $\mathcal{L}_s^{\mathrm{env}}(T_{\mathrm{dip}}^k) = 1 - 2\cos^2(\phi_\perp^k)$ which lies between -1 and $+1$. This dependence on the Fourier amplitude phase can be understood by studying the effective Hamiltonian, $\hat{H}_{\mathrm{eff}} = (\omega_{\mathrm{av}} - k\omega)\hat{I}_z + |f_\perp^k|\hat{\sigma}_{\phi_\perp^k - \frac{\pi}{2}} A_\perp \hat{I}_y$. Clearly the sensor state $|\psi\rangle = (|u\rangle + \exp(i(\phi_\perp^k - \pi/2))\,|d\rangle)/\sqrt{2}$ is an eigenstate of the stroboscopic dynamics. The maximal contrast of the coherence dip will depend on how much this eigenstate overlaps with the initial sensor state $|\psi_0\rangle = (|u\rangle + |d\rangle)/\sqrt{2}$. When $\phi_\perp^k = \pm\pi/2$ the initial state of the NV *is* an eigenstate of $\hat{H}_{\mathrm{eff}}$ so measurement of the coherence will return $\mathcal{L} = 1$. If $\phi_\perp^k = 0, \pi$ the spurious signal can be maximised. This is manifest in our analytic expression, Eq. (4.23), as the bounding envelope $\mathcal{L}_s^{\mathrm{env}}(T_{\mathrm{dip}}^k) = 1$ when $\phi_s^F = \pm\pi/2$ and $\mathcal{L}_s^{\mathrm{env}}(T_{\mathrm{dip}}^k) = -1$ when $\phi_k^F = 0, \pi$. This Fourier amplitude phase dependence observed via the quantum Floquet theory is corroborated by the pulse-phase control protocol for identifying spurious signals [43] proposed via a semi-classical analysis. In the next chapter we show how this Fourier amplitude phase dependence can be used to selectively enhance or suppress spurious signals.

At the dip $\epsilon_s = \frac{1}{2}|f_\perp^k A_\perp|$ so that the avoided crossing width is $\delta_{\epsilon_s} = |f_\perp^k A_\perp|$. The dip contrast is determined by $\mathcal{L}_s(N_pT_{\mathrm{dip}}) = 1 - 2\sin^2(\frac{1}{2}N_p\delta_\epsilon T_{\mathrm{dip}}^k)\cos^2(\phi_s^F)$ and, as with the

expected signals, the avoided crossing width also governs the sharpness of the spurious dip. We note that the perpendicular Fourier amplitude is naturally much smaller than the parallel Fourier amplitude, $|f_\perp^k| \ll |f_z^k|$ (see Figs. 4.3(b)(ii) and 4.7), so that the spurious signals are naturally much sharper than the expected signals. In the following chapter we discuss how this can be exploited to gain enhanced resolution in sensing experiments.

4.3.3 The CPMG Sequence

The Carr-Purcell-Meiboom-Gill (CPMG) sequence [139, 140] is possibly the simplest dynamical decoupling sequence (after the single pulse Hahn echo [138]). After initialising the sensor spin state to $|\psi_0\rangle = (|u\rangle + |d\rangle)/\sqrt{2}$ the sequence consists of two π-pulses along the x-axis before finally measuring the state along the x-axis. Whilst the sequence is well defined by two pulses, here we choose a basic eight pulse unit to make for easier comparison with the XY8 sequence. Our CPMG sequence is defined by: $\tau - \pi_x - 2\tau - \pi_x - 2\tau - \pi_x - 2\tau - \pi_x - 2\tau - \pi_x - 2\tau - \pi_x - 2\tau - \pi_x - 2\tau - \pi_x - \tau$, with a sequence period $T = 16\tau + 8t_p$.

Figure 4.8(b) shows the NV detection of a single ^{13}C nuclear spin under CPMG control. In contrast to the XY8 sequence (see Fig. 4.8(a)) the coherence trace shows no spurious dips, only the expected signal at $T = 4 \times 2\pi/\omega_{\text{av}}$. However, comparing the finite pulse, $t_p \neq 0$, signal with the ideal pulse, $t_p = 0$, signal we still see that there is a finite pulse effect on the expected dip. The reason for this difference between XY8 and CPMG is clear from studying the modulation function Fourier amplitudes, Fig. 4.3. For XY8 the perpendicular Fourier amplitudes, $f_\perp^k$, appear distinctly from the parallel Fourier amplitudes, f_z^k, opening new avoided crossings and creating the distinct spurious dips. For CPMG the perpendicular and parallel Fourier amplitudes coincide so no new avoided crossings are opened and no spurious dips appear.

As the perpendicular Fourier amplitudes are typically much smaller than the parallel Fourier amplitudes, $|f_\perp^k| \ll |f_z^k|$, the coherence profile is often well approximated by Eq. (4.20). However, in cases were this is not sufficiently accurate one must consider the entire effective Hamiltonian, Eq. (4.17). Obtaining an analytical expression for the coherence in this case is possible but hard as the effective Hamiltonian no longer separates into two 2-D subspaces. A satisfactory alternative is to use $\hat{H}_{\text{eff}}$ directly (Eq. (4.17)) to numerically approximate the signal, via $\hat{U}(N_p T) = \exp(-i\hat{H}_{\text{eff}} N_p T)$. This is shown in Fig. 4.8(c) to fit well with the numerical simulation obtained via directly propagating the time-dependent Hamiltonian, Eq. (4.1).

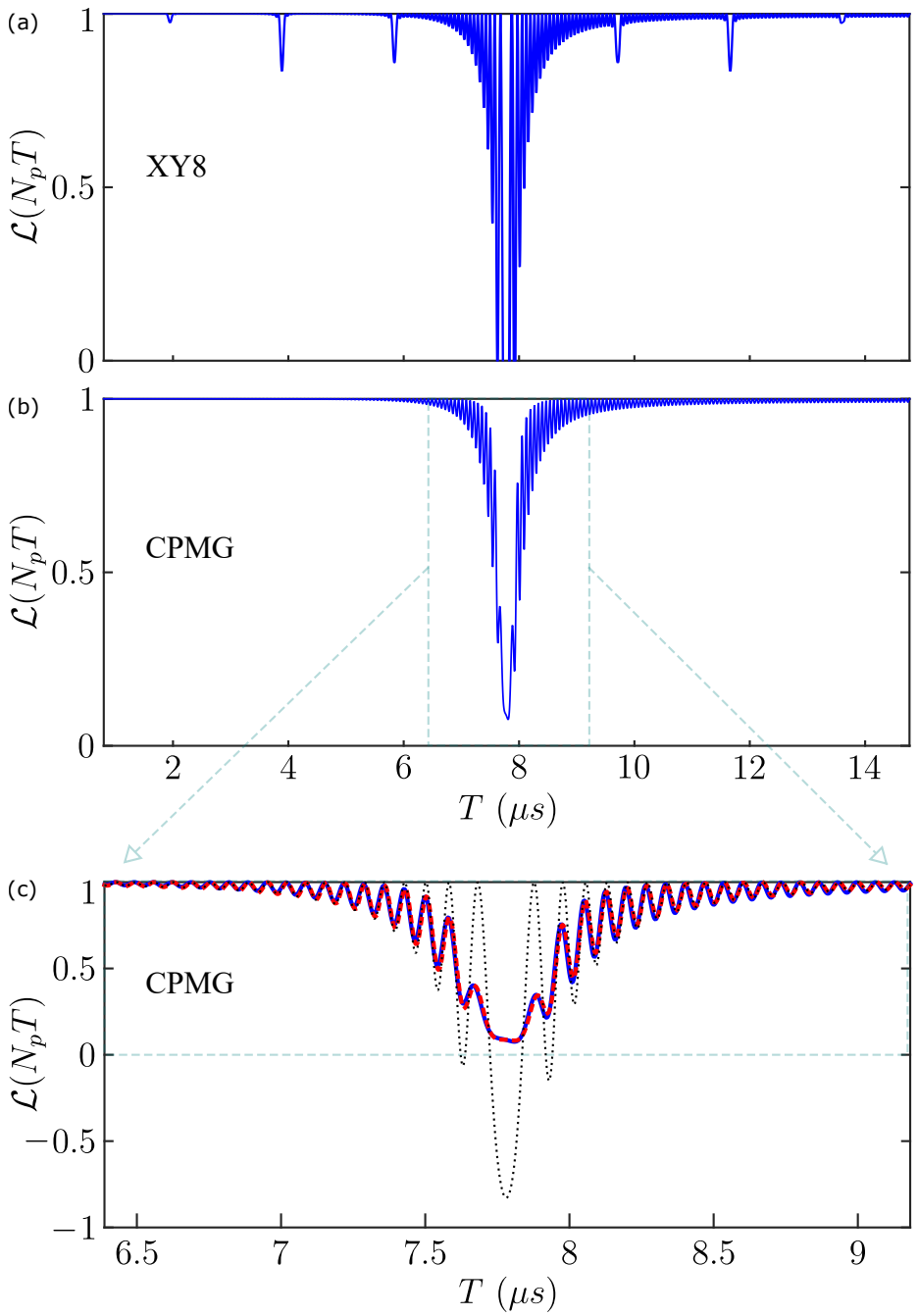

Figure 4.8: Comparison of the finite pulse duration XY8 and CPMG coherence response. All three panels here simulate the NV detection of a single ^{13}C. (a) shows the XY8 response which has spurious dips. (b) shows the CPMG response which has no spurious dips. (c) shows a zoom of the CPMG dip which shows that although there are no distinct spurious dips the finite-pulse durations still have some effect on the expected signal. In all 3 panels the blue solid line is numerically obtained by directly propagating the time-dependent Hamiltonian, Eq. (4.1). The black dotted line is a numerical simulation of the ideal, $t_p = 0$, signal which does not match the actual CPMG signal. A better fit (red dashed line) can be calculated from the effective Hamiltonian as discussed in the text. The numerical simulations include a magnetic field, $B_z = 480$ G, applied along the crystal axis whilst the carbon spin is hyperfine coupled to the NV with strength $[A_x, A_z] = [35, 0]$ kHz$\times 2\pi$. The square pulses applied have width $t_p = 100$ ns and $N_p = N/8 = 30$ repetitions of the sequence were applied.

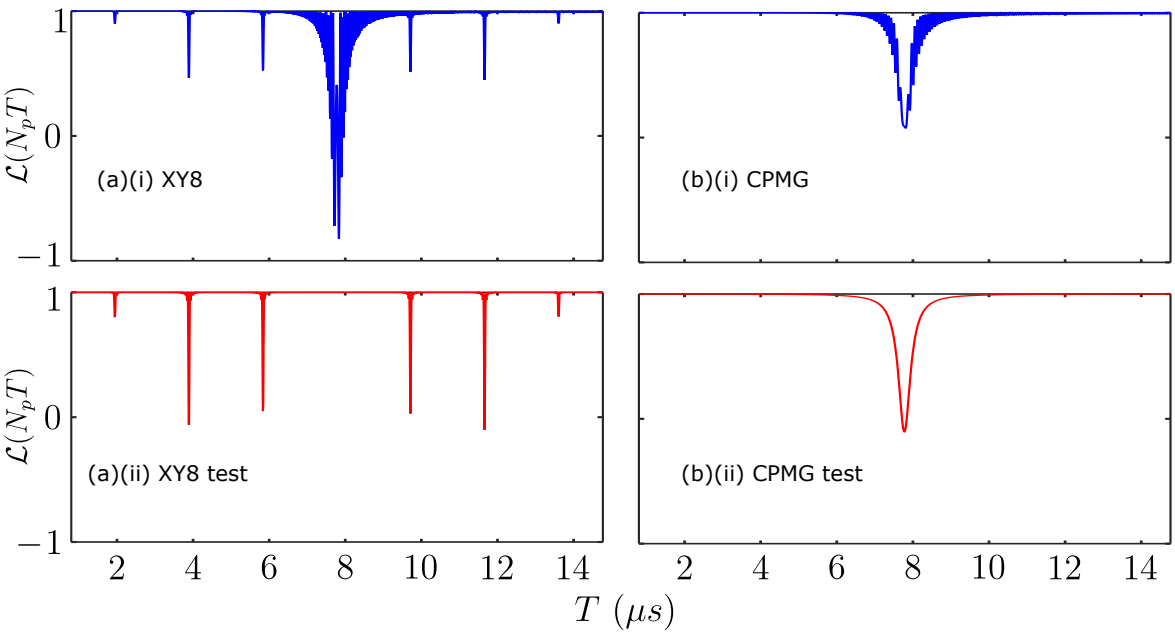

Figure 4.9: Figure showing a simple test to determine the origin of coherence signals. Parts (i) show the usual DD based detection of a ^{13}C using (a) XY8 and (b) CPMG. Parts (ii) show our suggested test protocol described in the text. The signals that remain in the test protocol indicate that those signals are associated with some sensor state mixing, i.e there is a non-negligible finite-pulse effect. The CPMG sequence is included to show that, although the sequence does not present distinct spurious dips, a finite-pulse effect is still present.

The co-occurrence of the expected and spurious signals for CPMG detection explains why finite pulse effects have not been reported in CPMG based experiments. In Chapter 6 we show that in the presence of static microwave detunings the finite pulse duration can have significant effects on the CPMG signal.

4.4 Identifying the Character of Coherence Dips

It will often be desirable to distinguish between coherence signals that are spurious in nature and those that are not. Whether to correctly classify the detected nuclear spin species [42] or possibly for the design of quantum gates [30]. (The spurious and expected dips swap different pairs of states.) If many spins are present in the environment their signals may overlap making it hard to determine which signals are real and which are spurious so we propose in this thesis a simple test to differentiate them.

The test protocol involves repeating the same DD experiment as usual except starting with the initial state $|m_s = 0\rangle$ (instead of the superposition state) and after the DD taking measurements of $\langle\hat{\sigma}_z\rangle$ (instead of $\langle\hat{\sigma}_x\rangle$). The expected coherence dips are associated with a sensor state *dephasing*. Thus, if there is no spurious effect present (i.e. $|f_\perp^k| = 0$

in Eq. (4.17)) then the initial test state, $|m_s = 0\rangle$, is an eigenstate of the DD effective Hamiltonian and will not evolve. The experiment will record no signal so the expected DD signal is removed in the test protocol. In contrast, the spurious coherence dips are associated with sensor state *mixing* and thus (if $|f_\perp^k| \neq 0$) the initial test state will never be an eigenstate of the effective Hamiltonian. Comparing the standard DD protocol with the test protocol we can identify spurious effects with those that do not vanish when the initial state is altered.

Figure 4.9 simulates the application of this test protocol. For the XY8 sequence the expected signal is removed but signals remain at the spurious resonances. For the CPMG sequence, a signal still remains at the expected dip position indicating that the dip here is not well approximated by the instantaneous-pulse DD response.

4.5 Pulse Shaping

Up until now we have assumed that the microwave pulses were square in shape with duration t_p and height $\Omega = \pi/t_p$. This simplified the construction of the pulse propagator, $\hat{U}_p(t)$, for the transformation to the toggling frame. Whilst other pulse shapes are available and have been explored in standard NMR [153, 154, 155] it is clearly interesting to understand how the pulse shape alters the finite-pulse effect. Pulse shaping has also been used to mitigate detuning errors [73], increase frequency sampling [156] and sensitivity in high-field nanoscale NMR [157] but these studies do not consider the spurious response.

We now start with a general pulse shape, $\Omega(t)$, defined within $[-t_p/2, t_p/2]$ and only require that $\int_{-t_p/2}^{t_p/2} \Omega(t)dt = \pi$ so that the a full π rotation is achieved. We assume all the pulses in the sequence have the same shape but they can be applied along arbitrary axes in the xy-plane, defined by the phase ϕ. The pulse Hamiltonian can thus be written as $\hat{H}_p(t) = \sum_m \Omega(t - t_m)\hat{S}_{\phi_m}$. We will define the quantity

$$\bar{\Omega}(t) = \int_{\frac{-t_p}{2}}^{t} \Omega(s)ds - \frac{\pi}{2} \tag{4.24}$$

so that during the m-th pulse, i.e. at $t = t_m + t'$ the pulse evolution operator is given by

$$\hat{U}_p(t') = \exp(-i(\bar{\Omega}(t') + \frac{\pi}{2})\hat{S}_{\phi_m})(-i\sigma_{\phi_{m-1}})(-i\sigma_{\phi_{m-2}})...(-i\sigma_{\phi_1})(-i\sigma_{\phi_1}). \tag{4.25}$$

Notice that for the square pulse $\bar{\Omega}(t) = \Omega t$ and the square pulse propagator, Eq. (4.6), is

recovered.

Using this general pulse propagator to transform to the toggling frame then proceeds as it did for the square pulse.

$$\hat{U}_p^\dagger(t)\hat{\sigma}_z\hat{U}_p(t) = (-1)^m \sin\bar{\Omega}(t')\sigma_z + \cos\bar{\Omega}(t')\sigma_{\varphi_m}, \tag{4.26}$$

where $\varphi_m = (-1)^{m+1}(\phi_m+\pi/2)+2\sum_{m'<m}^{m-1}(-1)^{m'+1}\phi_{m'}$, accounting for the specific phases chosen in the DD sequence. The modulation functions at $t' = t - t_m$ are

$$f_x(t') = \cos\bar{\Omega}(t')\cos\varphi_m, \tag{4.27}$$

$$f_y(t') = \cos\bar{\Omega}(t')\sin\varphi_m, \tag{4.28}$$

$$f_z(t') = (-1)^m \sin\bar{\Omega}(t') \tag{4.29}$$

and $f_{x,y}(t) = 0$ between pulses and $f_z(t) = \pm 1$.

It is also possible to obtain general expressions for the Fourier series of the modulation functions. We are interested in the perpendicular modulation functions, $f_\perp^k$, as these control the finite-pulse effects. Defining $f_\perp(t) = f_x(t) + if_y(t) = \sum_m \cos\bar{\Omega}(t-t_m)e^{i\varphi_m}$ we find

$$\begin{aligned} f_\perp^k &= \frac{1}{T}\int_0^T f_\perp(t)e^{-ik\omega t}dt \\ &= \frac{1}{T}\sum_m \int_{t_m-t_p/2}^{t_m+t_p/2} \cos\bar{\Omega}(t-t_m)e^{i\varphi_m}e^{-ik\omega t}dt \\ &= \frac{1}{T}\sum_m e^{i\varphi_m}e^{-ik\omega t_m}\int_{-t_p/2}^{t_p/2} \cos\bar{\Omega}(t')e^{-ik\omega t'}dt', \end{aligned} \tag{4.30}$$

where to get to the last line we have changed the integration variable to $t' = t - t_m$. We are interested in the size and phase of $f_\perp^k$ at the dip positions, where $\omega = \omega_{\rm av}/k$. At these positions the k-dependent behaviour is scaled by a *k-independent* functional of the pulse shape,

$$W[\bar{\Omega}(t)] = \int_{-t_p/2}^{t_p/2} \cos\bar{\Omega}(t')e^{-i\omega_{\rm av}t'}dt', \tag{4.31}$$

which encodes the information about the pulse shape. Thus we see that the pulse shape does not affect the relative sizes of the spurious signals but scales them all equally by some factor $W[\bar{\Omega}(t)]$.

As an example we study the effect of four different pulse shapes on an XY8 spurious dip, see Fig. 4.10. We compare square, triangle, Gaussian and Hermite [153, 154, 155] π-pulses that all have the same maximum height. The different perpendicular modulation functions

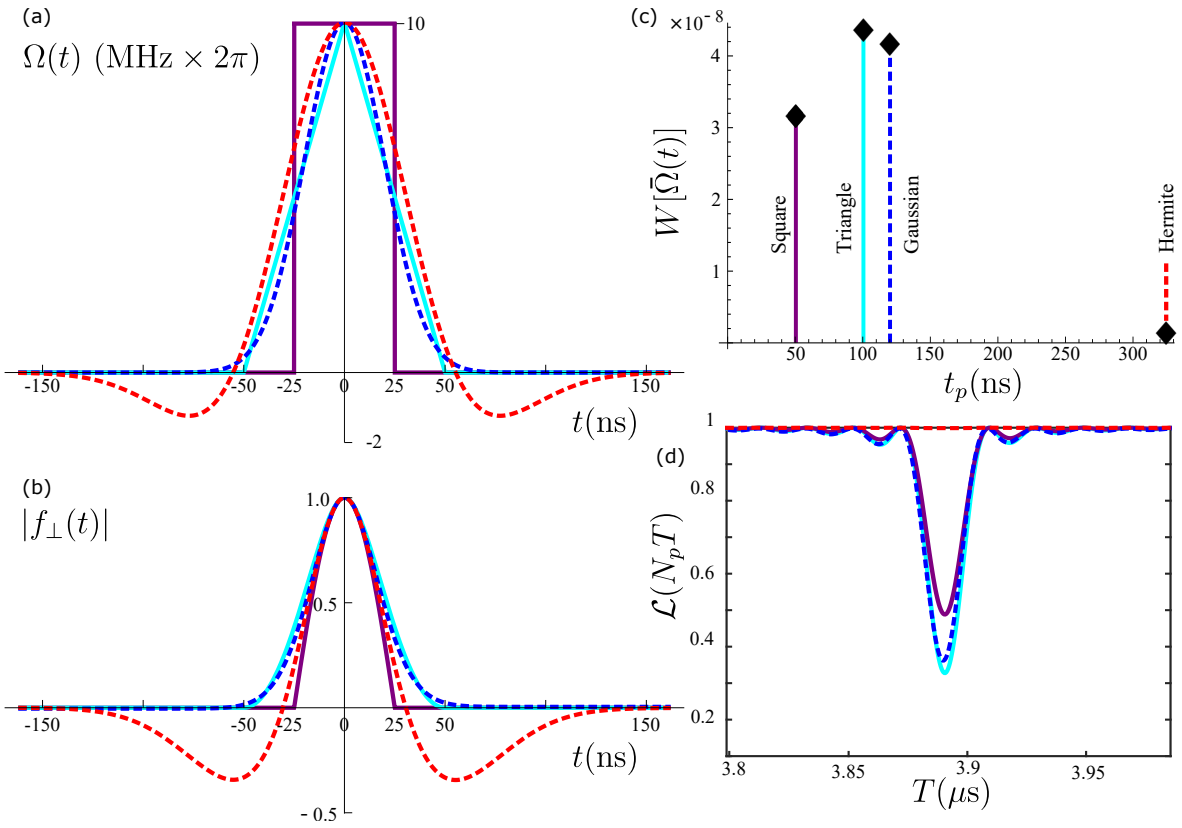

Figure 4.10: The microwave pulse shape directly affects the size of the spurious dips. We compare the effect of four different pulse shapes: square (purple solid line), triangle (cyan solid line), Gaussian (blue dashed line) and Hermite (red dashed line). (a) Shows the microwave pulse profile, $\Omega(t)$. (b) Shows the perpendicular modulation within a single pulse, $|f_\perp(t)| = |f_x(t)+if_y(t)| = |\cos\bar{\Omega}(t)|$. (c) Plots the scaling factor $W[\bar{\Omega}(t)]$ (Eq. (4.31) in the text) against the pulse duration. The black diamonds denote the scaling factor strength whist the dashed coloured lines are only added for easier referencing with the other plots. (d) Shows the $k = 2$ spurious dip under XY8 control with the different pulse shapes. Notice that the relative sizes of the spurious dip contrast mirrors the relative size of the scaling factors from part (c).

within one pulse are shown and we calculate the different scale factors $W[\bar{\Omega}(t)]$. The triangle and Gaussian pulses both have slightly larger scale factors than the square pulse thus slightly stronger spurious signals. This could be expected as they need a longer pulse duration (larger t_p) to achieve a π-rotation. However, the Gaussian pulse is marginally less susceptible to spurious effects than the triangle pulse even though the Gaussian pulse is wider. Remarkably, the widest pulse by far, the Hermite pulse, is incredibly effective at suppressing the finite-pulse effect possibly due to the negative lobes surrounding the central peak.

4.6 Future Work

In the previous section we saw that the Hermite pulse shape drastically suppresses the finite pulse effect and it would be useful to study the cause of this suppression. This understanding could then lead to the design of optimised pulse shapes. Whilst these pulse shapes were introduced to mitigate errors in standard NMR [153, 154] it is worthwhile understanding exactly how they affect the dynamics in nanoscale NMR.

Further desirable results include an extension of the correlated cluster expansion (CCE) [158] to include finite-pulse effects. CCE is a numerical method for simulating large spin baths, by progressively accounting for larger spin cluster sizes and only including up to a threshold cluster size. In the literature CCE has only been treated in the instantaneous pulse case where the spin bath effect on the sensor qubit is pure dephasing. As we have seen, finite duration pulses introduces sensor state mixing and this could have ramifications for higher order correlations between environmental spins. Ultimately, this could have an effect on the coherence decay of the sensor. In standard NMR it was shown that finite duration pulses can affect the coherence decay of nuclear samples [150, 151]. Alternatively, it would be interesting to understand the finite-duration-pulse effect on small clusters of nuclear spins (rather than the single spins treated here).

In the next chapter we use the new understanding of spurious dips, and finite-duration-pulse effects in general, gained in this chapter to propose new protocols that enhance the capabilities of current sensing experiments.

5 | Enhanced Sensing

Understanding the dynamics of the sensor-target system under applied dynamical decoupling allows for the design of new control protocols to mitigate errors [141, 45, 46, 47, 48, 39, 44], increase resolution and sensitivity [39, 93, 94, 95] and to manipulate nuclear spins to be exploited as quantum memories [98, 159, 32, 33]. In the previous chapter we expanded our understanding of the sensor-target dynamics, specifically in the presence of finite-duration control pulses, which expands our opportunities for control. In this chapter we propose protocols that exploit these new avenues of control to enhance our sensing capabilities.

Dynamical decoupling control parameters include the pulse phases [141, 44, 47, 46] and relative pulse positions within the sequence [45, 39, 93, 94, 95]. In the previous chapter we showed how the pulse *shape* affects the spurious dips and this is an interesting direction for future study. Some groups have already used pulse shaping to mitigate detuning errors [153, 154, 73], increase frequency sampling [156] and increase sensitivity in high-field nanoscale NMR [157]. Here we restrict our discussion to the choice of pulse phases as this offers an accessible method of control with significant results. Specifically, we seek to control or exploit the recently identified spurious signals.

One of the most pressing issues with spurious signals is that they can mimic the expected signal from other spin species [42]. For instance, spurious dips originating from a ^{13}C nuclear spin can coincide with expected DD signals from a ^{1}H nuclear spin, making it hard to classify which nuclear spin the signal originates from. It was subsequently shown that scanning an additional global phase, added to all pulses in the sequence equally, reveals the spurious dips due to their oscillating contrast [43]. That finding is corroborated by our analysis in Sec. 4.3.2 and in Sec. 4.4 we presented another method to determine the nature of coherence signals based on modifying the initialisation and measurement of the sensor. In this chapter we model the global-phase control and use it to prescribe the exact global phase required to selectively suppress spurious dips - removing the ambiguities in spin classification. This control can also be used to maximise the contrast of spurious dips

before exploiting their natural sharpness for enhanced resolution. Whilst tunable pulse sequences (that vary the relative pulse positions inside the basic pulse unit) have been designed to increase resolution [39, 93, 94, 95] we propose the use of spurious dips as a resource that does not involve the delicate positioning of control pulses. The spurious dips are naturally much narrower than the expected DD signals and are available as a resource in the widely used XY8 based sensing.

The addition of a global phase gives selective control over the spurious response but in general it is not able to suppress or enhance all spurious dips simultaneously. We propose a protocol to universally suppress the spurious dips which could be useful when many nuclear spins are present resulting in a busy spectrum with many dips. This universal suppression is achieved by randomising the additional global phase between repetitions of the sequence. This effectively averages out the finite-pulse effect whilst maintaining the expected DD signal. The use of a random variable may seem counter-intuitive but we show that other, deterministic schemes can produce extra unwanted spurious signals.

Finally, a newly introduced sequence, YY8 [44], was shown via a semi-classical analysis to prevent the appearance of spurious dips while maintaining the robustness of the XY8 sequence. We apply our quantum model to understand this removal of finite-pulse effects, demonstrate that detuning errors could still lead to the appearance of spurious dips and show that our randomisation protocol is still effective in this case. This chapter contains work published in Lang et al. (2017) [50] and work from a manuscript currently in preparation.

5.1 Selective Control of Spurious Dip Contrast

In the previous chapter we found the contrast of spurious coherence dips was sensitive to the phase of the sequence pulses. This was encoded into the phase of the perpendicular-modulation-function Fourier amplitude, $f_\perp^k = |f_\perp^k| e^{i\phi_\perp^k}$. This result is corroborated by the semi-classical study performed by Haase et al. [43] that showed the spurious dips are sensitive to a global phase, ϕ_g, added to all pulses within a pulse sequence i.e. $\phi_m \to \phi_m + \phi_g$, $\forall m$. We expand on the work by Haase et al. by providing an analytic expression for the global-phase dependence of the sensor coherence. We find that we can use this result to prescribe the exact global phase to either suppress or enhance spurious signals and show how this can be used to avoid ambiguities or enhance resolution.

5.1.1 Global Pulse Phases

A dynamical decoupling sequence of n_p pulses is defined by a set of pulse phases $\{\phi_1, ..., \phi_{n_p}\}$ (along with the pulse profile and relative pulse positions). The choice of pulse phases is designed to extend coherence or for robustness against pulse errors and many different sequences exist [139, 140, 141, 46, 44]. In the previous chapter we described how to model the coherence response under any choice of pulse phases.

Here we consider the effect of transforming an arbitrary pulse sequence to one where the pulse phases have all been shifted by some global phase, ϕ_g, so that the new DD sequence is defined by $\{\phi_1 + \phi_g, ..., \phi_{n_p} + \phi_g\}$. Note that we define the phase of all pulses relative to the x-axis which is set by the initial sensor superposition so the addition of a global phase is not inconsequential (We do not add the global phase to the initial superposition state or the measurement.) An equivalent experiment would be to initialise and readout the NV along the superposition state with the phase $\phi_0 = -\phi_g$ and leave the DD sequence unaltered. Later, however, we will change the additional phase within the sequence itself so this equivalence will disappear.

The experiment under the shifted DD sequence is described by the Hamiltonian, Eq. (4.1), where $\hat{H}_p(t;\phi_g) = \sum_m^N \Omega(t-t_m)\hat{S}_{\phi_m+\phi_g}$ and $N = N_p n_p$ is the total number of pulses applied after N_p repetitions of the sequence. We utilise the fact that the rotated pulses are equivalent to a non-rotated pulse viewed in a rotated frame, $\hat{S}_{\phi_m+\phi_g} = \exp(-i\phi_g\hat{S}_z)\hat{S}_{\phi_m}\exp(+i\phi_g\hat{S}_z)$. The Hamiltonian can then be written as

$$\hat{H}_0(t;\phi_g) = e^{-i\phi_g\hat{S}_z}\hat{H}_0(t;\phi_g=0)e^{+i\phi_g\hat{S}_z}. \tag{5.1}$$

In the previous chapter we showed that the true evolution due to the time-dependent $\hat{H}_0(t;\phi_g=0)$ matches the evolution due to a static effective Hamiltonian, $\hat{H}_{\text{eff}}(\phi_g=0)$, at stroboscopic times, $t = N_p T$. Thus, we can replace the time-dependent Hamiltonian in Eq. (5.1) and obtain an effective Hamiltonian for the rotated pulse sequence,

$$\hat{H}_{\text{eff}}(\phi_g) = e^{-i\phi_g\hat{S}_z}\hat{H}_{\text{eff}}(\phi_g=0)e^{+i\phi_g\hat{S}_z}, \tag{5.2}$$

$$= (\omega_{\text{av}} - k\omega)\hat{I}_z + f_z^k\hat{\sigma}_z A_\perp \hat{I}_x + |f_\perp^k|\hat{\sigma}_{(\phi_\perp^k - \frac{\pi}{2} + \phi_g)}A_\perp\hat{I}_y, \tag{5.3}$$

where for the last line we have used the form of the effective Hamiltonian given in Eq. (4.17). We see that the addition of a global phase to the pulse sequence only effects the spurious

dynamics (those weighted by $f_\perp^k$). The global phase rotates the axis about which the sensor states are mixed.

At spurious dips, where $f_\perp^k \neq 0$ but $f_z^k = 0$, the sensor coherence is given by

$$\mathcal{L}_s(N_pT;\phi_g) = 1 - 2\sin^2(\epsilon_s N_p T)\sin^2(\theta_s^F)\cos^2(\phi_s^F + \phi_g). \tag{5.4}$$

We see a sinusoidal dependence in dip contrast on the global phase which agrees with the semi-classical analysis from previous work [43]. We can also prescriptively set the global phase required to enhance (choose $\phi_s^F + \phi_g = 0, \pi$) or suppress (choose $\phi_s^F + \phi_g = \pm\pi/2$) the spurious dip contrast.

5.1.2 Unambiguous Classification of Nuclear Spin Species

In the first detection of spurious signals [42] it was noted that their presence leads to ambiguities in nuclear spin classification. This uncertainty occurs when the spurious signal from one nuclear spin species coincides with the expected signal from a different nuclear spin species. For instance in NV based sensing, when using the XY8 sequence, the first spurious coherence dip presented by a ^{13}C nuclear spin within the bulk of the diamond can mimic the signal expected from a ^{1}H nuclear spin on the diamond surface. This has implications for the desired on-surface detection of single molecules. In [42] a table is presented that lists nuclear spins with signals that can be mimicked by the spurious harmonic of another nuclear spin.

Scanning ϕ_g gives control over the spurious dip depths as we have shown above and in fact the k'th spurious resonance can be selectively removed, to avoid these ambiguities with other nuclear signals, by setting $\phi_g = -\phi_\perp^k \pm \pi/2$. Table 5.1 augments the table listed in [42] with the global phase required to suppress this spurious signal and is a key result of this work. These global phases are specific for the XY8 sequence but similar relations can be derived for any other DD sequence. By suppressing the spurious signal the ambiguity in nuclear spin classification can be removed.

5.1.3 Enhanced Resolution in DD Based Sensing

Recent theory proposals and experiments make use of tunable decoupling sequences to gain control over the effective coupling to nuclear spins [39, 93, 94, 95]. This involves the application of sequences made of composite pulses ("pulses" formed of several other pulses) with adjustable inter-pulse spacing so that one can tune $|f_z^k|$ and open or close avoided

Table 5.1: Isotopes susceptible to ambiguous characterisation due the presence of another isotope that mimics the signal at the listed harmonic. Applying the global phase, ϕ_g, to all pulses in the XY8 sequence suppresses the unwanted spurious signal for unambiguous nuclear species classification. (For XY8 the $n\times$ harmonic of the fundamental signal is at $T^k_{\text{dip}} = 2\pi k/\omega_{\text{av}}$ for $k = 4/n$.)

Isotope	Mimic	Harmonic	ϕ_g
^{1}H	^{13}C	$4\times$	$-\pi/4$
^{29}Si	^{13}C	$4/5\times$	$-\pi/4$
^{31}P	^{1}H	$2/5\times$	$+\pi/4$

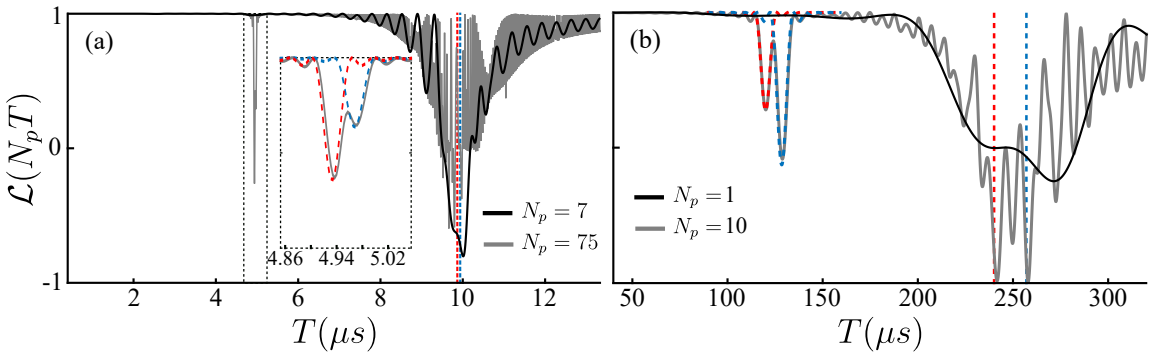

Figure 5.1: **(a)** Numerical simulation of the NV coherence coupled to two independent nuclear spins with $\omega^{(1)}_{\text{av}} = 2\pi \times 402.6$ kHz and $\omega^{(2)}_{\text{av}} = 2\pi \times 405.4$ kHz and hyperfine coupling strengths $A^{(1)}_{\perp} = 2\pi \times 21.6$ kHz and $A^{(2)}_{\perp} = 2\pi \times 31.0$ kHz. Solid black line: The coherence trace after $N_p = 7$ repetitions of the XY8 sequence. Solid grey line: The coherence trace after $N_p = 75$ repetitions. The finite pulses have height $\Omega = 2\pi \times 10$ MHz and width $t_p = \pi/\Omega$. The inset shows a magnification of the spurious dips with the analytic expression, Eq. (4.23), for each dip plotted also (dashed line). **(b)** Numerical simulation of the NV coherence coupled to two, more remote, independent nuclear spins with $\omega^{(1)}_{\text{av}} = 2\pi \times 16.67$ kHz and $\omega^{(2)}_{\text{av}} = 2\pi \times 15.56$ kHz and hyperfine coupling strengths $A^{(1)}_{\perp} = 2\pi \times 1.63$ kHz and $A^{(2)}_{\perp} = 2\pi \times 2.14$ kHz. Solid black line: The coherence trace after $N_p = 1$ repetitions of the XY8 sequence. Solid grey line: The coherence trace after $N_p = 10$ repetitions. The finite pulses have height $\Omega = 2\pi \times 100$ kHz and width $t_p = \pi/\Omega$. The analytic expression, Eq. (4.23), for the spurious dips is also plotted (dashed line). In each case the positions of the fundamental dip for each spin are denoted by the red and blue vertical dashed lines but these are unresolved because the frequency separation is less than the hyperfine coupling strength. By increasing the number of pulses the pairs of spins can be clearly resolved at the $k = 2$ spurious dip. A global phase of $\phi_g = -\pi/4$ has been applied to the pulse sequence to enhance the contrast at the spurious dip. This global phase also removes the $k = 1$ and $k = 3$ spurious dips.

crossings, i.e. augmenting or diminishing the effective coupling to nuclear spins and thus the width of experimental signals. By choosing $|f_z^k|$ to be small one can sharpen a selected coherence dip allowing for better resolution between isolated nuclear spins. The number of pulses that can be applied is constrained by the T_2 coherence time so that the minimal limit for $|f_z^k|$ is determined by the requirement that the dip still obtain a visible contrast after the maximum number of pulses.

One result of this work has been to see that spurious dips are naturally much narrower than the normal dips because $|f_\perp^k| \ll |f_z^k|$. Hence, if spurious signals are observed in the spectra one can increase the spectral resolution without complex pulse sequence design. One requires only that $|f_\perp^k|$ is not so small that the dips cannot obtain appreciable contrast after the maximum allowed number of pulses is applied (this is the same for tunable pulse sequences). From another point of view, the enhanced spectral resolution by spurious dips is realized by making the effective coupling smaller than the frequency separation.

This strategy has different benefits with respect to the use of more complex sequences. On the one hand, the use of sequences containing composite pulses requires one to apply a number of pulses larger than the one used by a standard sequence, such as XY8. In this respect, and even under moderate pulse error conditions, the applicability of composite sequences could be challenging because the error accumulates, damaging the signal. On the other hand, the use of a robust sequence of composite pulses requires an accurate control of each pulse phase [39, 93], i.e. each pulse has to rotate the NV state around a different axis on the xy-plane, and this is another experimental requirement to be addressed. Note that for a XY8 sequence just two phases are needed. Furthermore, the analytic expression, Eq. (5.4), indicates that one can also gain control over the spurious dips. By applying a global phase, ϕ_g, to all pulses or by carefully designing the pulse sequence to selectively control $f_\perp^k$.

A simple protocol for increasing resolution is demonstrated in Fig. 5.1, a key result of this chapter. Here an XY8 sequence drives an NV center coupled to two isolated nuclear spins (^{13}C in diamond for demonstration), in the first instance the spins are ≈ 0.6 nm from the NV whilst in the second instance the spins are more weakly coupled at ≈ 2 nm from the NV. In both cases initial attempts to resolve the spin with the fundamental dip fail because the hyperfine coupling strengths are greater than the signal separation. However, by judiciously increasing the number of pulses one obtains sharp spurious features where the signals can be resolved. One can also add a global phase to the pulse sequence to

enhance the contrast of the desired spurious dip (by choosing $\phi_g = -\phi_\perp^k$).

5.2 Randomising Global Phases for Universal Control of Spurious Dips

A key motivation for understanding and controlling spurious signals is that they can be erroneously characterised as signals from other spin species. For instance under XY8 control a ^{13}C spin will produce a spurious signal that mimics the expected signal from a ^{1}H spin leading to ambiguities in spin classification. Similarly, a natural abundance of ^{13}C in diamond could produce a forest of spurious signals that may shroud the ^{1}H signal altogether.

The previous sections of this chapter showed how to selectively control the contrast of individual spurious signals allowing one to remove ambiguities by "turning off" specific spurious resonances. However this does not address all spurious signals simultaneously. In Figure 5.1 we can see that as the XY8 $k = 1$ and $k = 3$ spurious dips have been suppressed the $k = 2$ spurious dip has been amplified. Universal control may be desirable in situations where spurious signals overlap, at high harmonics for example. We present a modification for DD sequences that suppresses spurious signals universally whilst maintaining the expected signal. This method is simple to implement, only requiring control of pulse phase and a random number generator, and is applicable to all DD sequence choices.

The key idea is to add a global phase to all pulses equally with one basic-pulse-unit (e.g. the 8 pulses defining XY8) and then to randomly change this phase each time the unit is repeated. As the expected signal is insensitive to pulse phases it is compounded as usual whilst the spurious signal does not accumulate. We note here that whilst the phase is randomised between each repetition it is not a global phase in the strictest sense - but we maintain the nomenclature to refer to the phase being added globally to all pulses *within each repetition*. We also note here that when the phase is randomised between repetitions there is *no longer* an equivalent experiment performed by changing the phase of the initial state and measurement and leaving the sequence untouched.

In Fig. 5.2 we demonstrate the method with the XY8 sequence. Fig. 5.2(a) shows the basic pulse unit for the XY8 sequence. The randomisation protocol is implemented whilst repeating the basic unit. A random global phase is added to all the pulses within each unit, as shown in Fig. 5.2(b). The result of this modification is shown in Figs. 5.2(c) and (d).

The usual DD sequence produces the expected signal but also produces several spurious dips due to the finite width of the microwave π-pulses. The randomised XY8 (RXY8) sequence maintains the expected signal but also suppresses the spurious signals achieving an excellent fit to the ideal signal (the signal produced by an equivalent DD sequence but with infinitesimal pulse width.) This is explained by the expected dips being insensitive to the phase of the pulses whilst the spurious dips are highly sensitive. Randomly changing the phase avoids the coherent accumulation of the spurious signals whilst still accumulating the expected signals. Adding the random phase globally within each repetition (instead of to every pulse individually) maintains the characteristic nature of that pulse sequence, e.g. it's robustness (XY sequences [141], KDD sequences [46, 47]). The original DD sequence is recovered by setting all the random phases to zero.

The evolution under the randomised DD sequence can be written as

$$\hat{U}(N_pT) = e^{-i\hat{H}_{\rm eff}(\Phi^r_{N_p})T} e^{-i\hat{H}_{\rm eff}(\Phi^r_{N_p-1})T} ... e^{-i\hat{H}_{\rm eff}(\Phi^r_2)T} e^{-i\hat{H}_{\rm eff}(\Phi^r_1)T}, \tag{5.5}$$

where $\hat{H}_{\rm eff}(\Phi^r)$ is the effective Hamiltonian for a DD sequence with the pulse phases shifted by a random global phase Φ^r. For weak signals, such as the spurious ones, we can approximate this evolution with another static Hamiltonian $\hat{U}(N_pT) \approx e^{-i\hat{H}_{\rm tot}N_pT}$ where

$$\hat{H}_{\rm tot} = \frac{1}{N_p}\sum_{n=1}^{N_p} \hat{H}_{\rm eff}(\Phi^r_n) \tag{5.6}$$

$$= (\omega_{\rm av} - k\omega)\hat{I}_z + f^k_z \hat{\sigma}_z A_\perp \hat{I}_x + |\eta||f^k_\perp|\hat{\sigma}_{\phi_\eta} A_\perp \hat{I}_y \tag{5.7}$$

and $\eta = |\eta|e^{i\phi_\eta} = \frac{1}{N_p}\sum_{n=1}^{N_p} \exp(i(\phi^k_\perp - \frac{\pi}{2} + \Phi^r_n))$. For the last line above we used the expression of the effective Hamiltonian given in Eq. (5.3). If Φ^r_n is an independent random variable chosen from $[0, 2\pi]$ then $\phi^k_\perp - \pi/2 + \Phi^r_n$ is also an independent random variable and η represents a 2-D random walk with an important property, $\langle|\eta|^2\rangle = \frac{1}{N_p}$.

In the previous chapter (Sec. 4.3.2) we showed that the contrast of coherence dips is dependent on the width of avoided crossings in the Floquet quasienergy spectrum. For spurious dips this width is $\delta_\epsilon = |f^k_\perp A_\perp|$. For the randomised sequence this factor is scaled by $|\eta|$ so that the new avoided crossing width is $\delta^R_\epsilon = |\eta||f^k_\perp A_\perp| = |\eta|\delta_\epsilon$.

Under usual DD control, the contrast of weak spurious signals can be approximated by

$$\mathcal{L}_s(N_pT_{\rm dip}) \approx 1 - \frac{1}{2}\delta^2_\epsilon N^2_p T^2_{\rm dip}\cos(\phi^F_s), \tag{5.8}$$

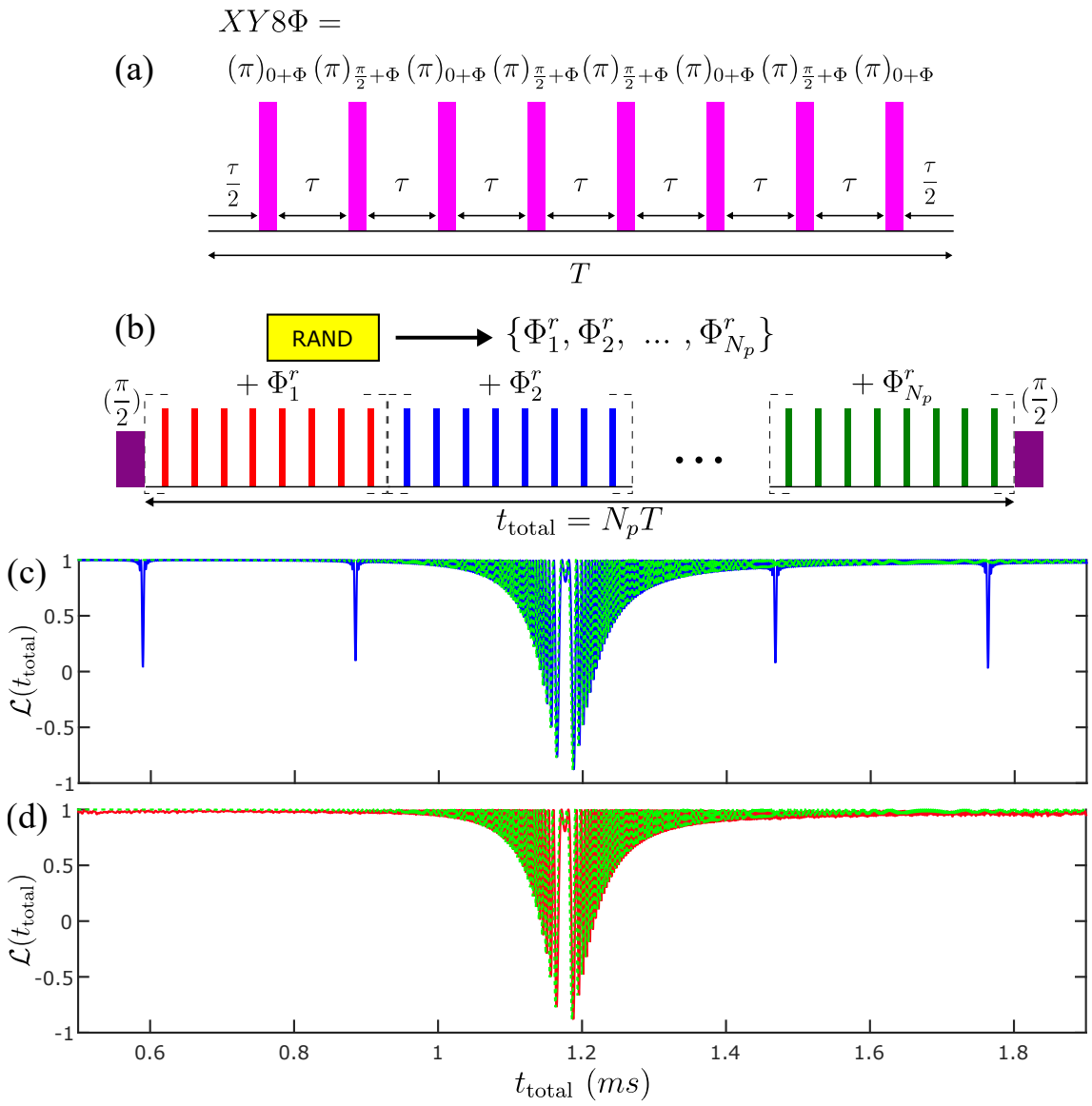

Figure 5.2: Randomisation scheme for removing spurious dips. Illustrated here with XY8. (a) The basic XY8 pulse unit. A basic pulse unit is defined by the pulse positions and phases. The pulse phases are measured relative to the initial superposition state of the quantum sensor (i.e. immediately after the initial $\pi/2$-pulse). The additional phase Φ denotes a global phase added to all pulses within the unit. (b) The randomised XY8 sequence. A larger dynamical decoupling sequence is built up by repeating the sequence N_p times. The randomisation protocol shifts all the pulses in each unit by a random global phase so that $RXY8\text{–}N_p = (XY8\Phi_1^r)(XY8\Phi_2^r)...(XY8\Phi_{N_p}^r)$. Setting $\Phi_n^r = 0, \forall n$ returns the usual XY8 sequence. (c) and (d) compare the NV coherence response under XY8–N_p ((c) blue solid line) and $RXY8$–N_p ((d) red solid line) whilst detecting a single nuclear spin-1/2. In both (c) and (d) the ideal sensor response is plotted (green dashed line), i.e. the sensor response when $t_p = 0$. Regular XY8–N_p produces spurious signals but the RXY8–N_p efficiently suppresses them, successfully reproducing the ideal signal. For the simulation $B_z = 300$ Gauss and the nuclear spin is a ^{13}C with $[A_x, A_z] = [36.5, 36.1]$ kHz$\times 2\pi$. A total of 800 square π-pulses are applied ($t_p = 100$ns) so that $N_p = 100$. The RXY8 sequence is averaged over 10 realisations of random phases.

which scales quadratically with N_p. When the random phases are introduced we can calculate the expectation value for the spurious dip contrast as

$$\langle \mathcal{L}_s^R(N_p T_{\rm dip})\rangle \approx 1 - \frac{1}{2}\langle (\delta_\epsilon^R)^2\rangle \, N_p^2 T_{\rm dip}^2 \, \langle \cos^2(\phi_\eta)\rangle \tag{5.9}$$

$$\approx 1 - \frac{1}{4}\delta_\epsilon^2 N_p T_{\rm dip}^2, \tag{5.10}$$

where we have used that $\langle (\delta_\epsilon^R)^2\rangle = \langle |\eta|^2\rangle \, \delta_\epsilon^2 = \frac{1}{N_p}\delta_\epsilon^2$ and $\langle \cos^2(\phi_\eta)\rangle = \frac{1}{2}$. Thus, we see that the randomised DD sequence suppresses the spurious dips by a factor of $\sim \frac{1}{N_p}$ and the randomised spurious dip only scales linearly with N_p as opposed to quadratically for the standard DD sequence.

The form of the factor η may suggest that one could specifically design a set of global phases to satisfy $\eta = 0$ thus completely suppressing the spurious dips. For instance, if N_p is even, one could simply set $\Phi_n^r = n\pi$. However, a numerical simulation shows that this does not work. Figure 5.3 shows the result of this method for an XY8 sequence. Although the *designed* global pulse phase does mitigate the spurious dips present in standard XY8, new spurious dips appear at different positions. This is because new resonances are being created on timescales longer than the XY8 period. The *randomised* sequence successfully suppresses all spurious dips.

It is worth stressing the universality of the protocol and this is demonstrated in Fig. 5.4 which shows that the randomisation protocol is applicable and effective for a range of pulse sequences including the XY family [141], Knill DD (KDD) sequences [46, 47] and the YY8 sequence [44]. The randomising protocol not only universally suppresses all spurious dips in the spectrum but it is universally applicable as well. The fact that the random phase is added globally within each basic unit means that the robustness of the sequences can be maintained. A further application for the protocol could be the recovery of the ideal CPMG signal seen in Fig. 4.8(c). The universality of this scheme is a key result of this chapter. This universality is evidenced in Eq. (5.7) where the spurious dynamics in the randomised protocol are weighted by the suppressing factor η. This factor is a feature of the randomisation and is independent of the particular pulse sequence chosen and is also independent of the particular spurious dip (independent of k). This results in the efficacy of the approach for all pulse sequences and all spurious dips.

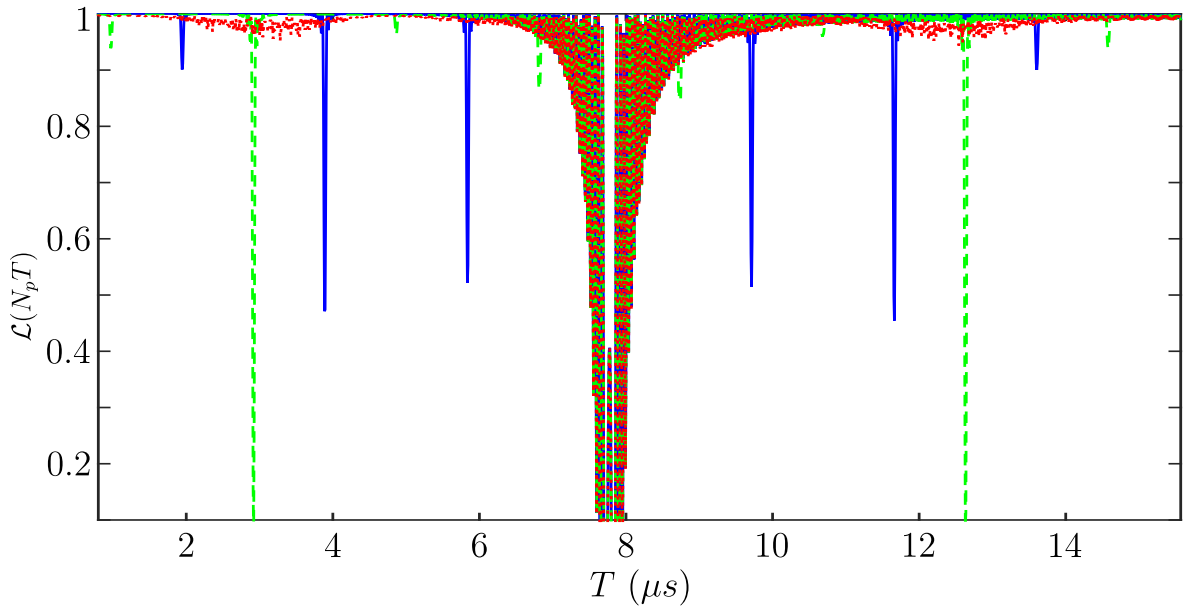

Figure 5.3: Comparison of XY8 detection (blue solid line), RXY8 detection (red dashed line) and XY8 detection with additional global phase $\Phi_n^r = n\pi$ as described in the text (green dashed line). The $\Phi_n^r = n\pi$ sequence suppresses the spurious signals that are present in the unmodified XY8 sequence but new spurious signals appear at different positions. The RXY8 sequence successfully suppresses all the spurious signals. Here we have simulated the NV detection of a single ^{13}C spin with hyperfine coupling $[35, 0]$ kHz $\times 2\pi$ at $B_z = 480$ G. A total of 480 pulses are applied with $t_p = 100$ ns and the RXY8 signal was averaged over 5 realisations.

5.3 The YY8 Sequence

The YY8 sequence [44] was recently introduced and is designed to be robust against pulse errors, similar to the XY8 sequence, but to remove the finite-pulse-effect spurious signals. The study used a semi-classical analysis based on the work of Haase et.al [43] to model the system response. Here we apply our quantum Floquet analysis to understand the YY8 sequence. We show why the YY8 sequence is successful at suppressing the spurious signals but can fail in the presence of microwave detunings.

The YY8 sequence is an 8 pulse sequence with the same pulse spacing and period as XY8 but with different pulse phases. The sequence is described by $\tau - \pi_{-y} - 2\tau - \pi_y - 2\tau - \pi_y - 2\tau - \pi_{-y} - 2\tau - \pi_{-y} - 2\tau - \pi_{-y} - 2\tau - \pi_y - 2\tau - \pi_y - \tau$, with a sequence period $T = 16\tau + 8t_p$.

The YY8 modulation functions and their Fourier amplitudes are plotted in Fig. 5.5 which can be compared with those for the CPMG and XY8 sequences in Fig. 4.3. The YY8 and XY8 sequence have the same parallel modulation functions, $f_z(t)$, because they share the same pulse spacing. The two sequences differ in their perpendicular modulation functions, $f_{x,y}(t)$, as these encode the pulse phase choices. Like the XY8 sequence, YY8

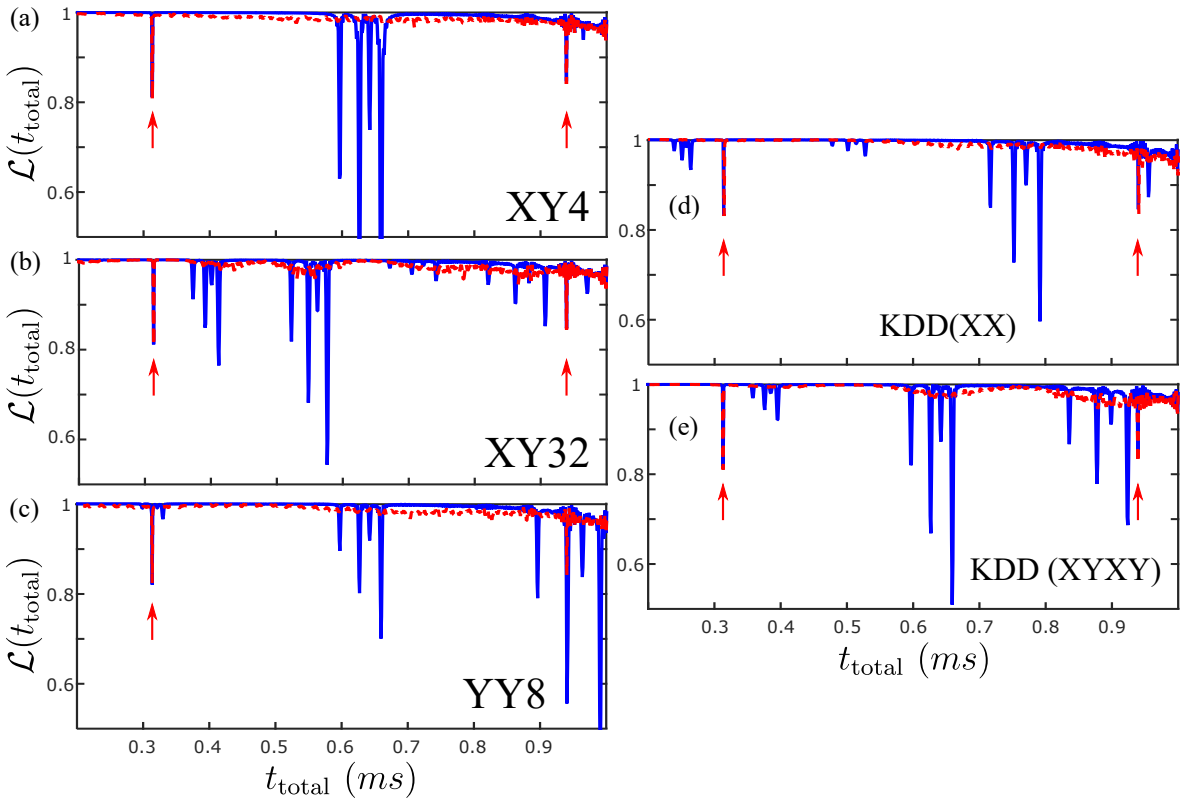

Figure 5.4: Randomisation protocol applied to five different pulse sequences. The randomisation protocol is universal and suppresses all spurious signals, here from four ^{13}C spins, whilst maintaining the ideal signal, here from a single ^{1}H spin (red arrows). (a) XY4 (blue solid) and RXY4 (red dashed). (b) XY32 (blue solid) and RXY32 (red dashed). (c) YY8 (blue solid) and RYY8 (red dashed) (d) KDD(XX) (blue solid) and RKDD(XX) (red dashed) (e) RKDD(XYXY) (blue solid) and RKDD(XYXY) (red dashed). In all cases, a total of 800 square π-pulses ($t_p = 50$ns) are applied, $B_z = 300$ Gauss and there are four ^{13}C spins: $[A_x, A_z] = \{[36.5, 36.1], [31.3, 4.25], [24.2, -27.7], [18.1, 19.3]\}$ kHz $\times 2\pi$ and a single ^{1}H spin $[A_x, A_z] = [1, 0]$ kHz $\times 2\pi$. The randomised simulations are averaged over 4 realisations. In (c) a microwave detuning of $\Delta = 0.5$MHz$\times 2\pi$ is included.

has perpendicular Fourier amplitudes, $f_\perp^k$, that are non-zero separately from the parallel Fourier amplitudes, f_z^k. Initially, this would suggest that the YY8 sequence will present spurious dips similarly to the XY8 sequence. However, for YY8, $f_{x,y}(t)$ are not odd on the interval $[0, T]$ meaning that one cannot write the effective Hamiltonian in the same manner as before (Eq. (4.17)), where we used the property $f_{x,y}^{-k} = -f_{x,y}^k$. Instead $f_y(t)$ is clearly zero (as there are only y-pulses) and thus $f_\perp^{-k} = f_\perp^{k*}$ where $f_\perp^k = f_x^k$. Thus, working from the general form of the effective Hamiltonian, Eq. (4.16), the YY8 effective Hamiltonian at spurious resonances can be written as

$$\hat{H}_{\text{eff}} = \frac{1}{2}\begin{pmatrix} (\omega_{\text{av}} - k\omega) & 0 & 0 & A_\perp f_\perp^{k*} \\ 0 & -(\omega_{\text{av}} - k\omega) & A_\perp f_\perp^k & 0 \\ 0 & A_\perp f_\perp^{k*} & (\omega_{\text{av}} - k\omega) & 0 \\ A_\perp f_\perp^k & 0 & 0 & -(\omega_{\text{av}} - k\omega) \end{pmatrix} \tag{5.11}$$

$$= (\omega_{\text{av}} - k\omega)\hat{I}_z + |f_\perp^k|\hat{\sigma}_x \otimes A_\perp \hat{I}_{\phi_\perp^k}\,. \tag{5.12}$$

We find that the Fourier amplitude phase, $\phi_\perp^k$, is imprinted onto the nuclear spin not the sensor and this is what prevents the appearance of spurious signals. The initial state of the sensor $|\psi_0\rangle = (|u\rangle + |d\rangle)/\sqrt{2} = |X_+\rangle$ is an eigenstate of the effective Hamiltonian. This initial state will not evolve under the effective Hamiltonian and no signal will be imprinted onto the coherence. (Note that the initial state is only an eigenstate of the stroboscopic evolution. It may still evolve within each period but returns to the initial state at stroboscopic times.) Fig. 5.6 compares the coherence response of the XY8 and YY8 sequences. The spurious dips are suppressed by YY8 but can be reinstated in the presence of a static detuning.

If we scan an additional global phase as described in Sec. 5.1.1 then the effective Hamiltonian becomes $\hat{H}_{\text{eff}} = (\omega_{\text{av}} - k\omega)\hat{I}_z + |f_\perp^k|\hat{\sigma}_{\phi_g} \otimes A_\perp \hat{I}_{\phi_\perp^k}$ and the coherence is given by

$$\mathcal{L}(N_p T) = 1 - 2\sin^2 \epsilon_s N_p T \sin^2 \theta_s^F \sin^2 \phi_g, \tag{5.13}$$

which clearly returns $\mathcal{L}(N_p T) = 1$ for $\phi_g = 0$. This also captures the behaviour presented in the YY8 paper. We note that spurious dips can still appear if detunings are present as shown in Fig. 5.4 but the randomisation protocol can assist to remove these. The issue of detuning errors in finite-duration-pulse experiments is discussed in the next chapter.

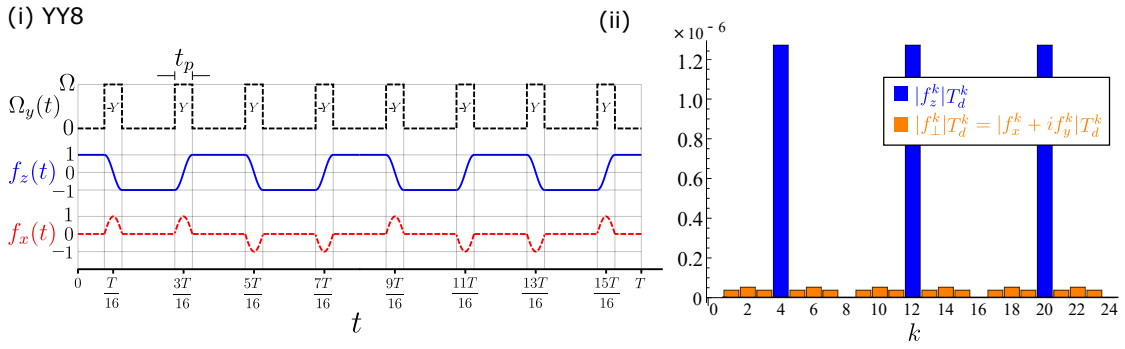

Figure 5.5: The YY8 sequence. (i) Shows the square pulse microwave amplitudes ($\Omega_x(t) = \sum_m \Omega(t - t_m)\cos\phi_m$, $\Omega_y(t) = \sum_m \Omega(t - t_m)\sin\phi_m$) and modulation functions ($f_i(t)$) for the YY8 pulse sequence. (ii) Shows the Fourier amplitudes of the modulation functions, $f_i^k = \frac{1}{T}\int_0^T f_i(t)\exp(-ik\omega t)dt$ where $\omega = 2\pi/T$, weighted by the resonant period $T_d^k = k \times 2\pi/\omega_{\text{av}}$. The parallel Fourier amplitudes are f_z^k and the perpendicular Fourier amplitudes are represented as a single quantity, $f_\perp^k = f_x^k + if_y^k$. These quantities can be compared with those for the XY8 and CPMG sequences as shown in Fig. 4.3

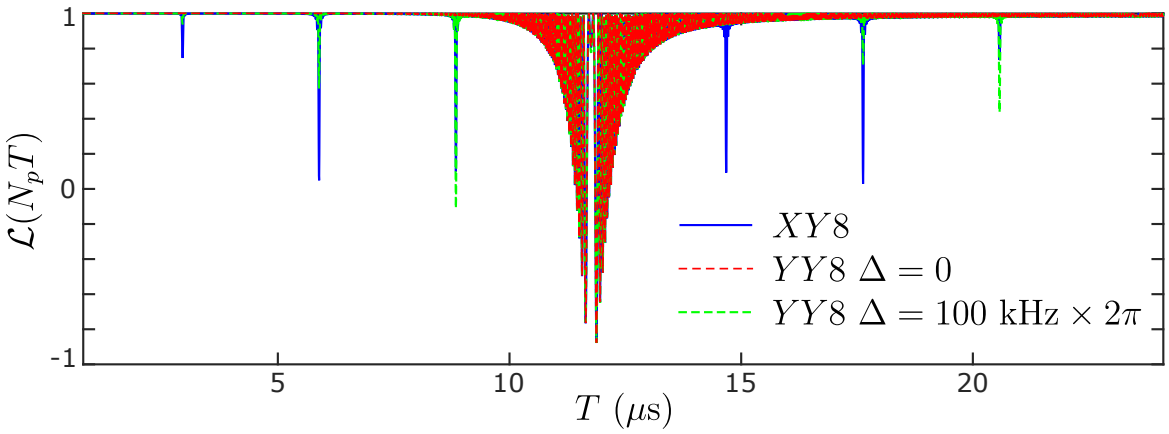

Figure 5.6: Comparison of the XY8 and YY8 coherence response. The YY8 sequence suppresses the spurious dips that appear in XY8 sequences. However, when a modest microwave detuning is present the spurious dips return, some even stronger than the original XY8 spurious dips. Here we simulated the NV detection of a ^{13}C with hyperfine coupling $[A_x, A_z] = [36.5, 36.1]$ kHz $\times 2\pi$ at 300 G. We apply 800 square pulses of duration 100 ns.

5.4 Future Work

In this chapter we introduced several protocols for enhancing the capabilities of dynamical decoupling based sensing. The protocols only require control of the pulse phases and exploit the appearance of spurious dips to obtain enhanced resolution without complex sequence design. More ambitious sequence designs could utilise pulse phases, shapes and positions in concert to control and exploit the finite-duration-pulse effects. One outstanding question relates to the noise introduced by the randomisation protocol. This noise can be seen most clearly in Fig. 5.3 (although the RDD response still outperforms the other two sequences). It would be useful to quantify the amount of noise one expects from this protocol to determine its limitations.

6 | Non-Vanishing Detuning Errors

Dynamical decoupling is designed to remove the effect of static and slowly oscillating fields. With instantaneous pulses ($t_p = 0$), the Hahn echo extends coherence times from the dephasing time T_2^* to the decoherence time T_2 by cancelling the quasistatic field created by the random configuration of nuclear spins in the bath (inhomogeneous broadening). Any phase acquired by the qubit sensor due to a static field is exactly cancelled after the π-pulse. Dynamical decoupling is thus insensitive to any detuning (detuning from the qubit frequency splitting) in the microwave field, which presents as a static field in the rotating frame, Eq. (2.8). Detunings can be introduced by errors in the microwave drive, by the host nitrogen spin (see Sec. 2.2.4) or by inhomogeneous broadening itself. Detunings are common in NV sensing experiments but are neglected because their effect is usually thought to vanish under DD control.

The finite pulse duration, however, introduces sensor state mixing ($\hat{S}_x, \hat{S}_y$ terms) into the Hamiltonian which does not commute with the static detuning field ($\hat{S}_z$) and thus the detuning can have appreciable effects. For instance, as shown in Fig. 6.1, a static detuning can amplify the contrast of spurious dips in XY8 based sensing and perhaps more strikingly, the static detuning causes the fundamental resonance in CPMG based sensing to split. Moreover, we see that this detuning effect completely vanishes under instantaneous pulse control, as expected. This indicates that this effect cannot be properly modelled using an instantaneous-pulse assumption and we are motivated to study this problem with a proper treatment of the finite pulse duration. The prevalence of detunings in NV based sensing makes this issue especially pressing.

The inclusion of a detuning breaks the periodicity in the toggling frame making it hard to apply Floquet theory. As the detuning is static, the periodicity is maintained in the original frame but here the Hamiltonian is not perturbative. To continue working in the toggling frame we follow an approach based on the Magnus expansion [38, 37] but augment it with the inclusion of the generalised modulation functions. We modify the generalised

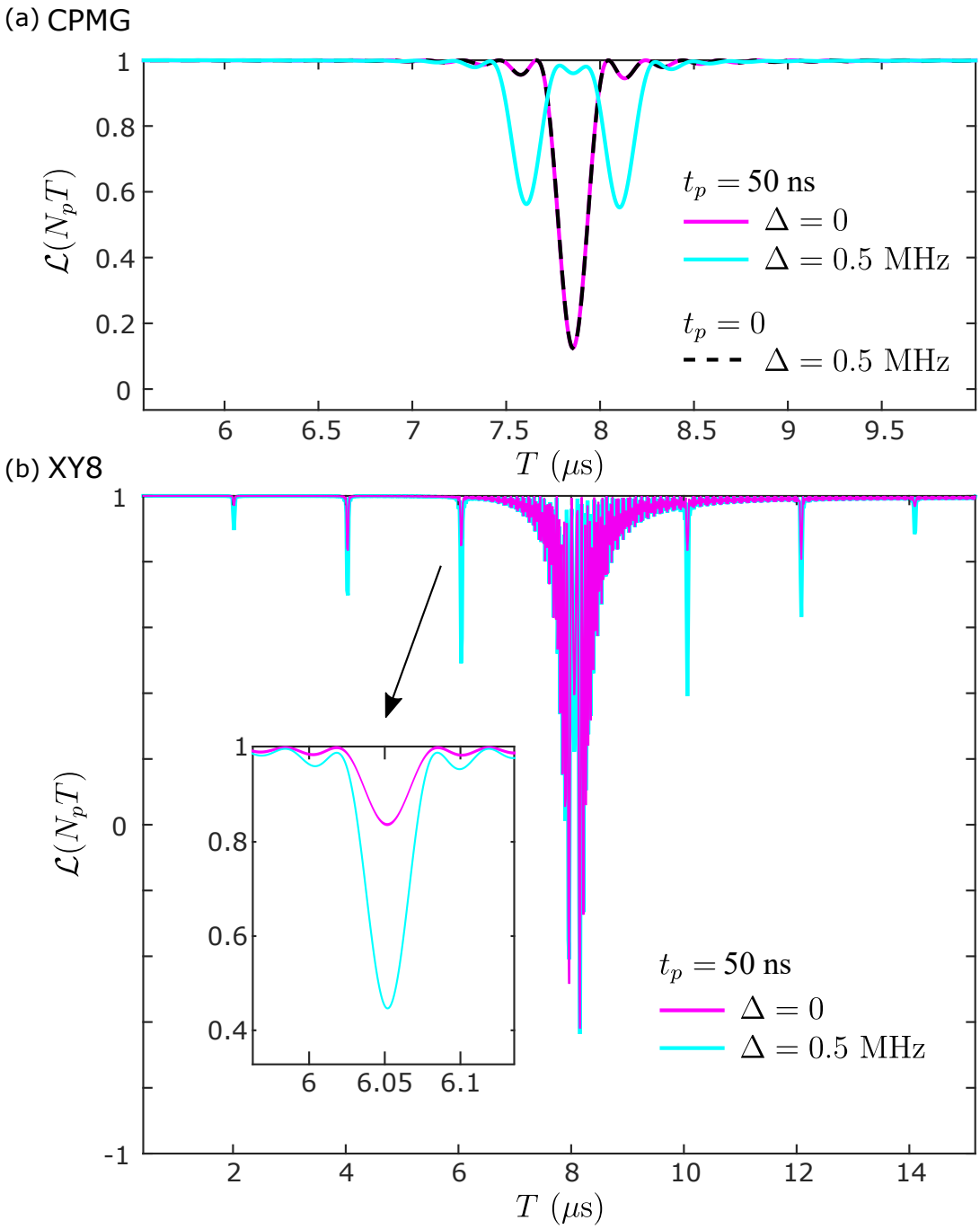

Figure 6.1: Numerical simulation of the detuning effect in finite pulse duration DD based sensing. Simulations are performed by directly propagating the time-dependent Hamiltonian. (a) Shows how the fundamental CPMG resonance is split when a static detuning is present. If the experiment is simulated with instantaneous pulses ($t_p = 0$) then this behaviour is not captured. Simulated here is the NV CPMG detection of a carbon spin at $B_z = 480$ G with hyperfine coupling $[A_x, A_z] = [9.13, 9.03]$ kHz $\times 2\pi$ and 80 total pulses. (b) Shows that a detuning in XY8 detection affects the contrast of spurious signals. Simulated here is the NV XY8 detection of a carbon spin at $B_z = 480$ G with hyperfine coupling $[A_x, A_z] = [36.50, 36.13]$ kHz$\times 2\pi$ and 480 total pulses.The detunings in the figure are listed in Hz to save space but in the text we use Hz$\times 2\pi$ units.

modulation functions, detailed in Sec. 4.1, to include the effect of a static detuning and use this to analytically model the detuning effect under finite pulses. We are able to derive a static effective Hamiltonian that approximates the dynamics and we find that the detuning modifies terms in the effective Hamiltonian that depend on the modulation functions. By studying the effect of the detuning on the generalised modulation functions (or more specifically, on their resonances) we can understand the detuning effect on the sensor response. The treatment is general, but for examples we specifically analyse the two cases illustrated in Fig. 6.1 - the splitting of the CPMG fundamental resonance and the increasing contrast of XY8 spurious dips.

An important source of detunings is inhomogeneous broadening. The random alignment of nuclear spins at the start of each experimental run creates a quasistatic field that causes the qubit to dephase under statistical averaging in a time T_2^*, the dephasing time. Typically, it is assumed that this dephasing is completely removed by the Hahn echo and other DD sequences extending the coherence time to T_2. However, due to the non-vanishing effect of detuning errors, inhomogeneous broadening *can* effect the sensor response. We demonstrate this by presenting the suppression of a CPMG coherence dip due to inhomogeneous broadening.

Other possible pulse errors are contained in the phase and rotation-angle and the motivation for many pulse sequence designs is to minimise their effects [141, 45, 46, 47, 48, 39]. However, we are specifically interested in the detuning error as this vanishes when $t_p = 0$ meaning the behaviour cannot be captured by most models which only consider instantaneous pulses.

First we show how to derive the generalised modulation functions in the presence of a static detuning and then use these to derive a static effective Hamiltonian that approximates the system dynamics. For weak signals we can give an approximate expression for the sensor coherence response. We then specifically explain the effects observed in Fig. 6.1 by studying how the detuning affects the generalised modulation functions for XY8 and CPMG. Finally, we present a case where inhomogeneous broadening alone is enough to suppress the signal from a single nuclear spin. The work presented in this chapter is currently being prepared for submission.

6.1 The Static Effective Hamiltonian and Coherence Response

A nitrogen vacancy center coupled to a nuclear spin cluster via a pure-dephasing hyperfine interaction can be modelled by the Hamiltonian $\hat{H}_0 = |u\rangle\langle u| \otimes \hat{H}_u + |d\rangle\langle d| \otimes \hat{H}_d$, where u and d represent the NV *up* and *down* states respectively and $\hat{H}_{u,d}$ is the nuclear Hamiltonian conditioned on the NV spin state. With the application of microwave control the Hamiltonian can be written as

$$\hat{H}_0(t) = \hat{H}_{\text{av}} + \hat{\sigma}_z \hat{V} + \hat{H}_p(t), \tag{6.1}$$

where $\hat{H}_{\text{av}} = (\hat{H}_u + \hat{H}_d)/2$ is the nuclear average Hamiltonian and $\hat{V} = (\hat{H}_u + \hat{H}_d)/2$ is the nuclear interaction Hamiltonian, $\hat{\sigma}_z = |u\rangle\langle u| - |d\rangle\langle d|$ and $\hat{H}_p(t)$ describes the microwave pulse control. The pulse Hamiltonian includes any static microwave detuning from the NV resonance and is given by $\hat{H}_p(t) = \sum_m \Omega(t - t_m)\hat{S}_{\phi_m} + \Delta \hat{S}_z$ where $\Omega(t)$ describes the pulse shape, ϕ_m is the phase of the m-th pulse and Δ is the detuning strength. The pulses are defined to be of width t_p and satisfy $\int_{-t_p/2}^{+t_p/2} \Omega(t)dt = \pi$ to obtain π-pulses.

We now move to the toggling frame. As described in Sec. 4.1 this is the frame rotating under the Hamiltonian $\hat{H}_p(t)$. In the present analysis we also make a second rotation under the nuclear average Hamiltonian, $\hat{H}_{\text{av}}$. As these Hamiltonians commute it is equivalent to moving to the frame rotating under $\hat{H}_p(t) + \hat{H}_{\text{av}}$. We obtain

$$\hat{H}(t) = \sum_{i=x,y,z} f_i(t)\hat{\sigma}_i \hat{\tilde{V}}(t), \tag{6.2}$$

where $\sum_{i=x,y,z} f_i(t)\hat{\sigma}_i = \hat{U}_p^\dagger(t)\hat{\sigma}_z\hat{U}_p(t)$ and $\hat{\tilde{V}}(t) = \exp(+i\hat{H}_{\text{av}}t)\hat{V}\exp(-i\hat{H}_{\text{av}}t)$. Here $\hat{U}_p(t) = \hat{\mathcal{T}}\exp(-i\int_0^t \hat{H}_p(s)ds)$ is the pulse propagator that contains the detuning.

The generalised modulation functions, $f_i(t)$, now include the effect of the detuning and the XY8 and CPMG sequences are shown in Fig. 6.2. We see that the periodicity of CPMG is immediately broken as a detuning is introduced. As CPMG is formed of π_x-pulses only we see that the $f_x(t)$ modulation function is only slightly perturbed whereas the $f_y(t)$ modulation function is strongly perturbed and begins to take on the character of $f_z(t)$. The XY8 sequence is designed to mitigate the accumulation of pulse errors and we can see this in the modulation functions. Even for larger detunings the sequence manages to recover the initial conditions at $t = T$. The parallel modulation function, $f_z(t)$, is largely unaffected whereas the perpendicular modulation functions, $f_{x,y}(t)$, are perturbed

but maintain the same periodicity.

We seek to propagate the density matrix in the toggling frame, $\rho(t) = \hat{U}(t)\rho_0\hat{U}^\dagger(t)$ where we will derive $\hat{U}(t) = \hat{\mathcal{T}}\exp(-i\int_0^t \hat{H}(s)ds)$ shortly. However, measurements of the NV are made in the original frame so we must transform back before evaluating the coherence. We only take measurements of the NV state so the transformation to the frame rotating under the nuclear average Hamiltonian has no effect on the measurement. When $\Delta = 0$, the pulse sequence is periodic by design, $\hat{U}_p(N_pT) = \hat{\mathbb{I}}$, and the transformation to the toggling frame does not affect the measurement. When $\Delta \neq 0$, the periodicity can fail and the coherence is given by

$$\mathcal{L}(N_pT) = \mathrm{Tr}\{\hat{\sigma}_x\hat{U}_p(N_pT)\hat{U}(N_pT)\rho_0\hat{U}^\dagger(N_pT)\hat{U}_p^\dagger(N_pT)\} \tag{6.3}$$

$$= \mathrm{Tr}\{\hat{U}_p^\dagger(N_pT)\hat{\sigma}_x\hat{U}_p(N_pT)\hat{U}(N_pT)\rho_0\hat{U}^\dagger(N_pT)\} \tag{6.4}$$

where we have used the cyclic property of the trace operator. The imperfect pulse propagator effectively shifts the measurement of $\hat{\sigma}_x$ to $\hat{\sigma}'_x = \hat{U}_p^\dagger(N_pT)\hat{\sigma}_x\hat{U}_p(N_pT) = \sin\theta\cos\phi\hat{\sigma}_x + \sin\theta\sin\phi\hat{\sigma}_y + \cos\theta\hat{\sigma}_z$ where θ, ϕ can be determined numerically. If the pulse propagator only introduces a small error then $\theta \approx \pi/2$ and $\phi \approx 0$. The coherence can then be written as $\mathcal{L} = \sin\theta\cos\phi\mathcal{L}_x + \sin\theta\sin\phi\mathcal{L}_y + \cos\theta\mathcal{L}_z$ where $\mathcal{L}_i(N_pT) = \mathrm{Tr}\{\hat{\sigma}_i\hat{U}(N_pT)\rho_0\hat{U}^\dagger(N_pT)\}$. We now seek $\hat{U}(N_pT)$, the evolution in the toggling frame.

In general, the toggling frame Hamiltonian is no longer periodic and we cannot apply Floquet theory. Instead we proceed by an approach based on the Magnus expansion [38, 37] which provides a static effective Hamiltonian that approximates the dynamics. Strictly, $\hat{U}(N_pT) = \hat{\mathcal{T}}\exp(-i\int_0^{N_pT}\hat{H}(t')dt')$ but the time-ordered exponential is hard to evaluate analytically. The Magnus expansion gives an approximation to this integral and states that $\hat{U}(N_pT) = \exp(\sum_n \chi_n)$ where the first two terms in the sum are

$$\chi_1 = -i\int_0^{N_pT}\hat{H}(t')dt', \tag{6.5}$$

$$\chi_2 = -\frac{1}{2}\int_0^{N_pT}dt_1\int_0^{t_1}dt_2[\hat{H}(t_1), \hat{H}(t_2)]. \tag{6.6}$$

The Magnus expansion is valid for small rotations, i.e. weak-signals and for weakly-coupled spins, when $\chi_2 \ll \chi_1$, we can approximate the evolution with only the first term [37].

Taking only the first order term gives an effective Hamiltonian $\hat{U}(N_pT) \approx \hat{U}_{\mathrm{eff}}(N_pT) = \exp(-i\hat{H}_{\mathrm{eff}}N_pT)$ where $\hat{H}_{\mathrm{eff}} = \frac{1}{N_pT}\int_0^{N_pT}\hat{H}(t')dt'$. If $|\alpha\rangle$ are the nuclear average Hamilto-

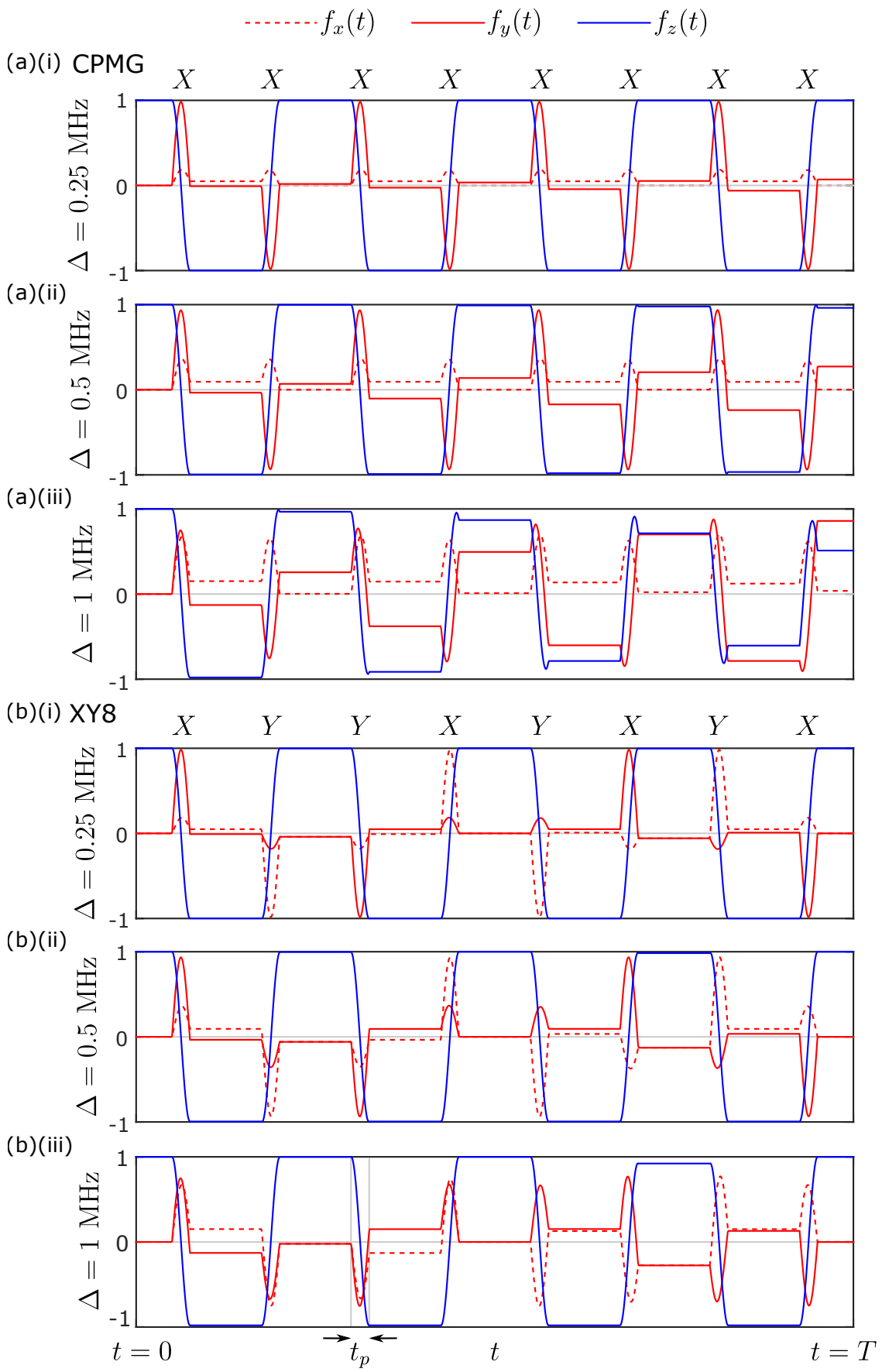

Figure 6.2: The generalised modulation functions for CPMG (parts (a)) and XY8 (parts (b)) with varying detuning strengths. The modulation functions are plotted over 8 pulses. (This is one XY8 period but 4 CPMG periods.) The detunings are listed in Hz to save space but in the text we use Hz$\times 2\pi$ units.

nian states then $\hat{H}_{\text{av}} = \sum_\alpha \omega_\alpha |\alpha\rangle\langle\alpha|$ and $\hat{\tilde{V}}(t) = \sum_{\alpha,\alpha'} V_{\alpha\alpha'} \exp(-i(\omega_{\alpha'} - \omega_\alpha)t)|\alpha\rangle\langle\alpha'|$ where $V_{\alpha\alpha'} = \langle\alpha|\hat{V}|\alpha'\rangle$. Then we can write the effective Hamiltonian as

$$\hat{H}_{\text{eff}} = \frac{1}{N_p T} \int_0^{N_p T} \sum_{i=x,y,z} f_i(t')\hat{\sigma}_i \sum_{\alpha,\alpha'} V_{\alpha\alpha'} \exp(-i(\omega_{\alpha'} - \omega_\alpha)t)|\alpha\rangle\langle\alpha'|dt' \tag{6.7}$$

$$= \sum_{i,\alpha,\alpha'} \frac{1}{N_p T} \int_0^{N_p T} f_i(t') \exp(-i(\omega_{\alpha'} - \omega_\alpha)t')dt'\hat{\sigma}_i V_{\alpha\alpha'}|\alpha\rangle\langle\alpha'| \tag{6.8}$$

$$= \sum_{i,\alpha,\alpha'} \tilde{f}_i(\omega_{\alpha'} - \omega_\alpha)\hat{\sigma}_i V_{\alpha\alpha'}|\alpha\rangle\langle\alpha'|, \tag{6.9}$$

where we have defined the Fourier transform $\tilde{f}_i(w) = \frac{1}{N_p T}\int_0^{N_p T} f_i(t)\exp(-i\omega t)dt$. Equation (6.9) represents the most general effective Hamiltonian derived from this analysis and is a key result of this chapter. In the following we model the detection of a single spin-1/2 nucleus where $\hat{H}_{\text{av}} = \omega_{\text{av}}\hat{I}_z$ and $\hat{V} = A_\perp \hat{I}_x + A_\parallel \hat{I}_z$.

For $\Delta = 0$ the design of most DD sequences ensures that $\tilde{f}_i(0) = 0$. For $\Delta \neq 0$ this is no longer true, however, as the modulation functions are oscillatory we still have that $\tilde{f}_i(0) \approx 0$ and we can neglect these terms. This is especially true when sufficiently many pulse have been applied to average out the oscillations. We can then collect the remaining terms into the form

$$\hat{H}_{\text{eff}} = \sum_{i=x,y,z} |\tilde{f}_i(\omega_{\text{av}})|\hat{\sigma}_i A_\perp \hat{I}_{\phi(f_i(\omega_{\text{av}}))}, \tag{6.10}$$

where $f_i(\omega_{\text{av}}) = |f_i(\omega_{\text{av}})|\exp(i\phi(f_i(\omega_{\text{av}})))$. The Fourier transform of the modulation function has peaks at the DD resonances. The inclusion of finite pulse durations and detunings can shift resonances, create new resonances or modify the height of resonant peaks. Fig. 6.3 compares the coherence modelled using our derived expression for the effective Hamiltonian (Eq. (6.10)) against the coherence simulated by directly propagating the time dependent Hamiltonian. We see a good fit to numerics.

For weak signals we can approximate the effective propagation with $\hat{U}_{\text{eff}}(N_p T) = \hat{\mathbb{I}} - i\hat{H}_{\text{eff}} N_p T - \frac{1}{2}\hat{H}_{\text{eff}}^2 N_p^2 T^2$ and substitute it into our equation for the coherence to obtain

$$\mathcal{L}_x(N_p T) \approx 1 - \frac{1}{2}A_\perp^2(|\tilde{f}_y(\omega_{\text{av}})|^2 + |\tilde{f}_z(\omega_{\text{av}})|^2)N_p^2 T^2, \tag{6.11}$$

$$\mathcal{L}_y(N_p T) \approx \frac{1}{2}A_\perp^2|\tilde{f}_x(\omega_{\text{av}})||\tilde{f}_y(\omega_{\text{av}})|N_p^2 T^2\cos(\phi(\tilde{f}_x(\omega_{\text{av}})) - \phi(\tilde{f}_y(\omega_{\text{av}}))), \tag{6.12}$$

$$\mathcal{L}_z(N_p T) \approx \frac{1}{2}A_\perp^2|\tilde{f}_x(\omega_{\text{av}})||\tilde{f}_z(\omega_{\text{av}})|N_p^2 T^2\cos(\phi(\tilde{f}_x(\omega_{\text{av}})) - \phi(\tilde{f}_z(\omega_{\text{av}}))). \tag{6.13}$$

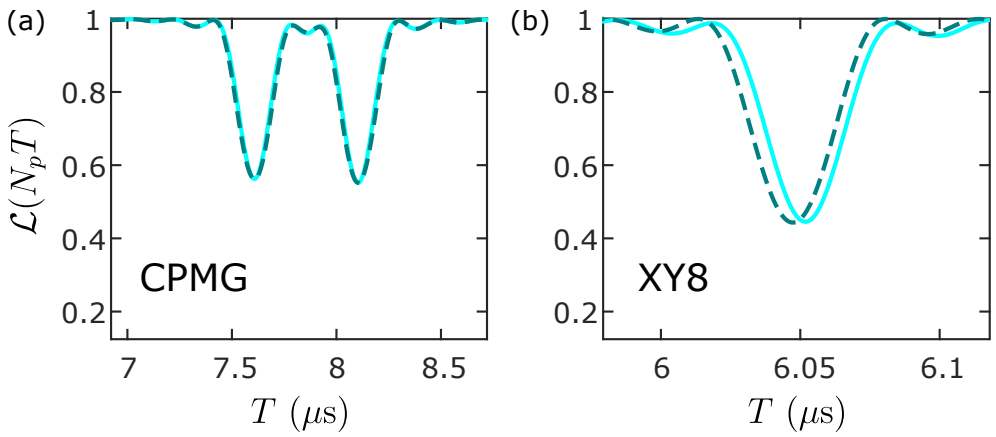

Figure 6.3: We re-plot the simulations made in Fig. 6.1 (cyan solid line) and compare against the prediction based on our derived effective Hamiltonian (teal dashed line) for (a) CPMG and (b) XY8. There is a good fit to numerics. We only plot the $\Delta = 0.5$ MHz $\times 2\pi$ case and for the XY8 sequence we only show the zoomed inset from Fig. 6.1(b).

Thus peaks in $|f_i(\omega_{\text{av}})|$, the DD sequence resonances, correspond to dips in the sensor coherence. This agrees with the usual semi-classical interpretation of DD based sensing that says coherence dips appear when the DD is resonant with an incident AC magnetic field. In fact, a classical field could be treated with a similar analysis if the quantum field $\hat{\tilde{V}}(t)$ in Eq. (6.2) is replaced with a classical field. As the coherence is measured along the x-axis the y and z modulation functions typically have a stronger effect. To understand the effect a static detuning has on the coherence profile we must look at the effect the detuning has on the DD resonances, i.e. we must study $|f_i(\omega_{\text{av}})|$.

For strongly coupled spins it may become important to consider the effect of the higher order Magnus expansion terms. This was done in [38] but without the inclusion of finite pulse durations or detunings. Moreover, Eq. (6.9) is valid for any size of nuclear spin cluster and it would be interesting to use this to analyse the finite pulse effect on cluster dynamics, sensor response and spin correlations as discussed in [37].

We now look at two specific cases discussed in the introduction to this chapter and illustrated in Fig. 6.1.

6.2 The Detuning Effect in CPMG Based Sensing

As shown in Fig. 6.1(a) the presence of a static detuning in finite-pulse-duration CPMG sensing causes the expected resonant coherence dip to split. This is due to the splitting of the resonance in the modulation functions as shown in Fig. 6.4. For zero detuning only the parallel modulation function has appreciable affect on the coherence. At non-

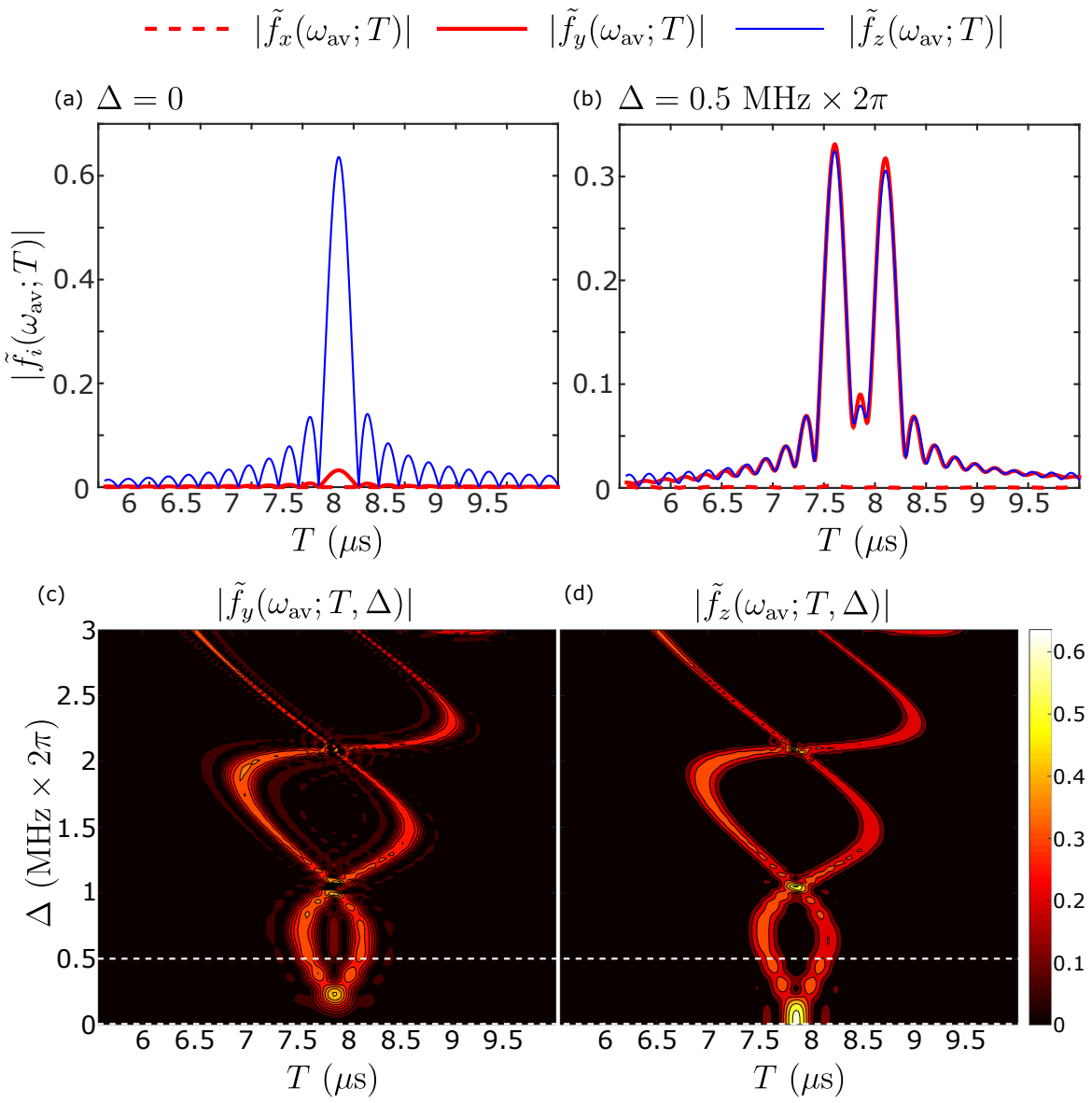

Figure 6.4: CPMG. (a) and (b) show the Fourier transform of the modulation functions for zero and non-zero detunings, evaluated at the nuclear average Hamiltonian frequency $\omega = \omega_{\rm av}$. This is plotted as a scan of the intended DD period, T. (Intended because the detuning breaks the periodicity. In this study we choose an 8 pulse period so we can compare CPMG and XY8.) Notice that for zero detuning the resonant peak is actually twice as high as the split peaks at non-zero detuning.(c) and (d) show color maps detailing how the Fourier transforms of the modulation functions are affected by a scan of detunings. The detuning causes the resonant peak to split or recombine depending on the detuning strength. The white dashed lines indicate the traces shown in (a) and (b). Here we simulate the same experiment shown in Fig. 6.1(a). The x Fourier transform scan is not shown it can be neglected when compared with the y, z-contributions.

zero detunings the perpendicular modulation function $f_y(t)$ takes on the character of the parallel modulation function $f_z(t)$ as seen in Fig. 6.2(a) and now again in Fig. 6.4. The perpendicular modulation function $f_x(t)$ remains small. We see from Fig. 6.4(c) and (d) that for stronger detunings the splitting of the coherence dip seen in Fig. 6.1(a) could be much greater. The splitting of the resonance can be understood as the beating between the usual DD frequency and a new slower frequency introduced because the detuning causes small rotation errors in π-pulse. These two frequencies can be observed in Fig. 6.2(a)(iii).

The splitting of the CPMG signal has important consequences in the presence of strong detunings due to the host nitrogen spin and even the weak detunings caused by inhomogeneous broadening as discussed below in Sec. 6.4. A valuable future project would be to analytically determine the splitting of the resonant peaks so that one quantify the detuning error effect. This dip splitting will become important if the splitting is larger than the coherence dip width.

6.3 The Detuning Effect in XY8 Based Sensing

In Fig. 6.1(b) we saw that static detunings modulate the strength of spurious coherence dips which are present due to the finite pulse duration. This effect was also seen in the previous chapter for the YY8 sequence which is designed to suppress spurious dips but fails when detunings are present (see Fig. 5.4(c)).

The detuning effect on XY8 based sensing is explained by the amplification of the perpendicular (x,y) modulation function resonances as seen in Fig. 6.5(a) and (b) whilst the expected resonance is largely unchanged, Fig. 6.5(c). The resonance positions are not shifted as they are for CPMG because the XY8 sequence successfully mitigates the accumulation of errors at periodic times ($t = mT$) as can be seen from the modulation functions in Fig.6.2(b). Although this may start to fail for very strong detunings. Even though the sequence maintains its periodicity the perpendicular modulation functions are still perturbed during the sequence and this leads to the increase in their resonance strengths. The parallel (z) modulation function is largely unaffected by the detuning and this is seen in the constant resonance height.

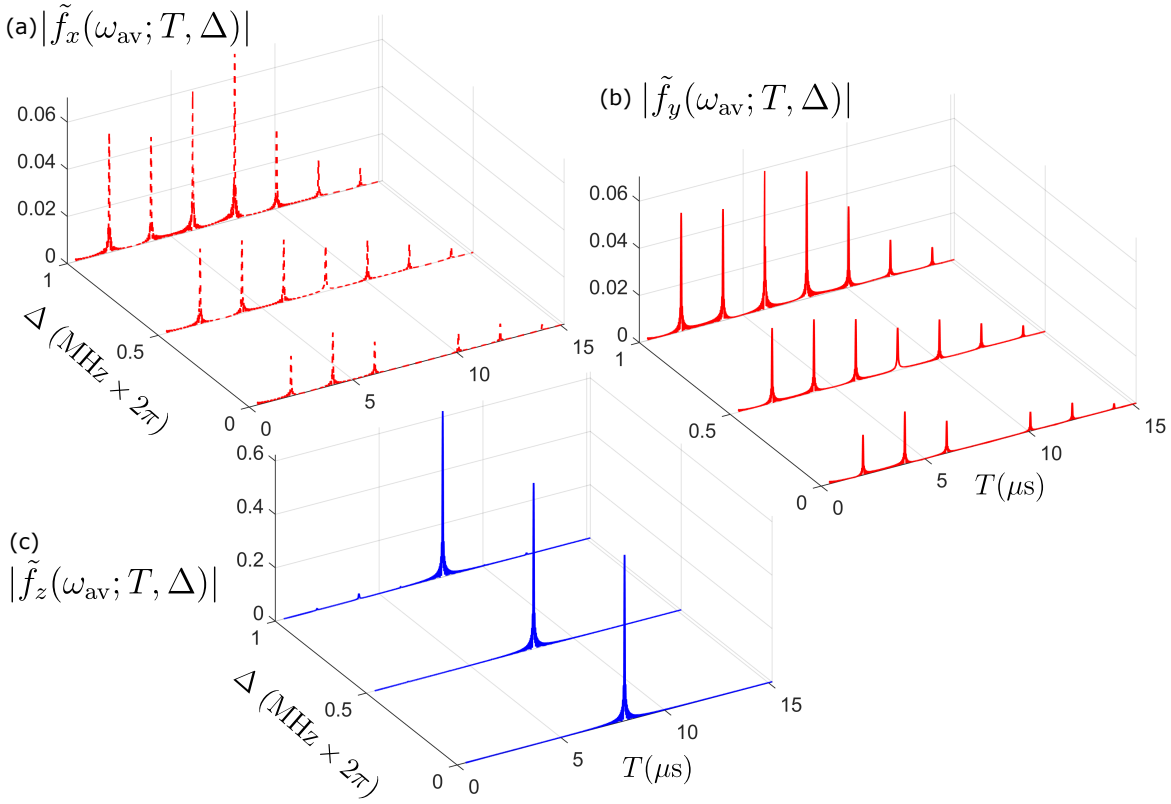

Figure 6.5: XY8. The Fourier transforms of the (a) x, (b) y and (c) z modulation functions evaluated at the average nuclear Hamiltonian frequency $\omega = \omega_{\rm av}$. They are parametrised by the DD sequence period, T, and a static detuning, Δ. The expected DD resonance sits at $T \approx 8$ μs while all other resonances are spurious and are present due to the finite pulse duration. Note the difference in vertical axis scale between plots. Here we simulate the same experiment described in Fig. 6.1(b).The detuning amplifies the resonant peaks in the x, y-spectra explaining the amplification of the spurious signals.

6.4 The Non-Vanishing Effect of Inhomogeneous Broadening

We have shown above that a static detuning causes the CPMG coherence dip to split. If the detuning is quasistatic (static within each experimental run but changing between runs) then the statistical averaging of the signal, to obtain adequate SNR, will cause the CPMG dip to be suppressed. Specifically if a distribution of detunings are present with a width on the order of or greater than the coherence dip width then contribution of many distinct dip splittings will cause the averaged signal to appear spread out and suppressed. Fluctuations in the microwave drive could provide this distribution but a more intrinsic source of quasistatic detunings is inhomogeneous broadening.

Inhomogeneous broadening, as explained in Sec. 2.3.1 is the decay of the NV coherence due to a quasistatic magnetic field created by the random configuration of nuclear spins during each experimental run. In free induction decay experiments the NV dephases in a time, T_2^*, due to inhomogeneous broadening. In Hahn echo and DD experiments, with instantaneous pulses ($t_p = 0$), the dephasing is removed as inhomogeneous broadening is a quasistatic detuning that has no effect. We have shown above that due to the finite duration of microwave pulses that this is not always the case.

We can model the inhomogeneous broadening field as a magnetic field $b_z\hat{\mathbf{z}}$ where b_z is a normal random variable selected from a Gaussian distribution with zero mean and standard deviation, $\sigma = \sqrt{2}/T_2^*$ [143]. Fig. 6.6 shows the difference between XY8 and CPMG detection of a single ^{1}H in the presence of inhomogeneous broadening. The CPMG signal is suppressed as for each static detuning the resonance is split and averaging over the Gaussian distribution of splittings causes the signal to spread out. The XY8 signal is unaffected as the detuning does not split the resonance position. The dephasing time modelled here was $T_2^* = 1$ μs which corresponds to a detuning distribution of $\sigma \approx 225$ kHz$\times 2\pi$ and the Hydrogen spin has hyperfine coupling strength 1 kHz. This effect has implications specifically for detecting spins outside the diamond where the hyperfine coupling to the NV is very weak. This weak coupling translates to a narrow coherence dip so it is easy for a small detuning to split the coherence signal. The dephasing time used here is quite short with some NVs having T_2^*s of 10 or 20 μs but for these longer dephasing times, the detuning could still suppress the signals of more weakly coupled spins. As the sensitivity of NV based sensing increases this suppression effect is an important consideration.

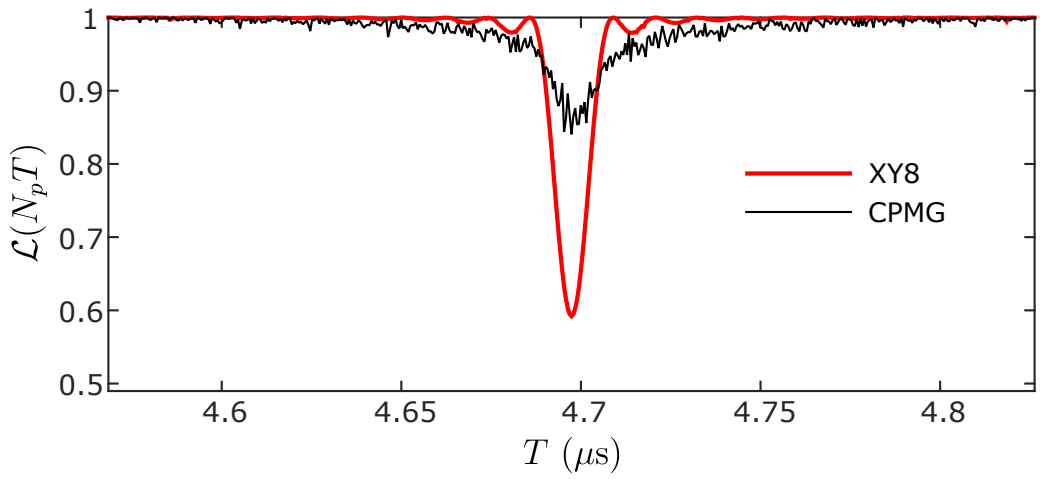

Figure 6.6: Shows the suppression of the CPMG coherence dip due to inhomogeneous broadening. Here we numerically simulate the NV detection of a ^{1}H nuclear spin with hyperfine coupling $[A_x, A_z] = [1, 0]$ kHz $\times 2\pi$. A magnetic field, $B_z = 200$ G, is applied along the NV axis and a total of 800 pulses are applied (of XY8 and CPMG) with pulse duration $t_p = 50$ ns. The inhomogeneous broadening is modelled as a quasistatic magnetic field aligned with the NV axis chosen from a Gaussian distribution with zero mean and standard deviation $\sigma = \sqrt{2}/T_2^*$. We assume $T_2^* = 1$ μs and average over 50 realisations.

6.5 Future Work

Future work could include an analytical study of the modulation function resonances so that one could quantify the CPMG splitting or XY8 spurious dip amplification for instance. This could also be used to quantify the suppression of the CPMG signal due to inhomogeneous broadening and get reasonable bounds for when this can be neglected and when it must be taken into account.

Another important source of detunings is the host nitrogen and it would be useful to study the effects this has on the NV coherence trace. The host nitrogen splits the NV upper energy level by, approximately, the parallel hyperfine coupling strength, $A_\parallel^{\mathrm{N}}$, which is 2.14 MHz$\times 2\pi$ for ^{14}N or 3.03 MHz$\times 2\pi$ for ^{15}N. If the nitrogen levels are not selectively addressed this leads to large detunings which could have a strong effect on the coherence response.

In Chapter 4 we mentioned how the correlated cluster expansion [158], a numerical method for simulating the dynamics of large spin baths, may be affected by the finite pulse durations removing the pure-dephasing nature of the sensor-environment coupling. As we have seen here the bath *can* affect the sensor in unexpected ways (due to inhomogeneous broadening). We restate here that it would be worthwhile studying the effect of finite-duration-pulses (and static detunings) on the sensors interaction with a large spin bath

perhaps via a modified correlated cluster expansion.

Finally, by swapping the quantum operator $\hat{\tilde{V}}(t)$ in Eq. (6.2) for a classical fluctuating field this method could be used to study the finite-duration-pulse and detuning effects on classical field detection.

7 General Conclusions

The work presented in this thesis constitutes four key outcomes. First, we provided the first application of Floquet theory to dynamical decoupling based quantum sensing experiments. Secondly, we performed the first quantum (not semi-classical) analysis of finite-duration-pulse effects in dynamical decoupling experiments. Thirdly, this analysis of finite-duration-pulse effects was used to propose new protocols for enhanced sensing. Finally, we studied the interplay between finite pulse durations and detuning errors and were able to predict the drastic effects (such as coherence dip splitting and suppression) that are overlooked by instantaneous pulse models. Here, we conclude the thesis by reviewing these results before discussing future directions for research.

7.1 Floquet Analysis of Dynamical Decoupling Based Sensing

Motivated by the periodic nature of many dynamical decoupling sequences we presented the first application of Floquet theory for modelling dynamical decoupling based sensing. Initially, we modelled the CPMG detection of a single spin-1/2 assuming that the microwave π-pulses were instantaneous. By constructing the one-period evolution operator and diagonalising it we obtained the system Floquet quasienergies and modes which we used to derive expressions for the sensor coherence response. We found that the characteristic coherence dips are associated with avoided crossings in the Floquet quasienergy spectrum and the width of the avoided crossings determines the width and contrast of the coherence dips. We modelled the NV detection of a single ^{13}C nuclear spin-1/2 and the Si:Bi detection of a ^{29}Si spin dimer and trimer.

7.2 Finite-Duration-Pulse Effects

The power of the Floquet analysis is seen as we expanded the theoretical model to include finite-duration pulses. The association of coherence dips with avoided crossings in

the quasienergy spectrum remains and in fact we see that appearance of spurious dips, present because of the finite pulse-durations [42], is heralded by the opening of previously closed avoided crossings. We are able to predict the full NV-nuclear spin dynamics and the coherence response under any DD sequence and in particular we show how the XY8 and CPMG sequences respond to finite pulse-durations. We point out that the spurious coherence dips are caused by sensor state mixing rather than dephasing and use this to suggest a protocol for determining the nature of coherence dips. We also studied the effect the pulse *shape* has on the spurious response.

7.3 Enhanced Sensing

With our acquired understanding of finite-duration-pulse effects we suggested several protocols to enhance the capabilities of sensing experiments. First we showed we could selectively suppress or amplify spurious signals by shifting all pulse phases by some global phase. The suppression is useful to remove ambiguities in the classification of nuclear spin signals and the amplification is useful when exploiting the natural sharpness of spurious dips to obtain an increased resolution in sensing experiments. Next we showed how to universally suppress spurious signals by randomising the global phase between sequence repetitions. This protocol universally suppresses all spurious dips in the coherence trace and is universally applicable to any choice of pulse sequence.

We also applied Floquet theory to understand how the YY8 sequence [44] suppresses spurious signals. We pointed out that the sequence can still present spurious signals if a detuning is present but showed that our universal scheme for suppressing spurious signals is also applicable in this case.

7.4 Detunings and Finite Pulses

We analytically modelled the effect of detuning errors in finite-duration-pulse DD experiments. Unlike for the instantaneous pulse assumption, the detuning error can have an effect on the dynamics and coherence response. We showed how the XY8 spurious dips can be amplified and the CPMG expected signal can be split. Strikingly, we demonstrated that the CPMG signal can be significantly suppressed just by the inhomogeneous broadening due to the nuclear spin bath. We modelled these experiment by expanding the Magnus expansion approach [38, 37] to include the generalised modulation functions that describe

finite duration pulses.

7.5 Future Work

Future research building on the work presented in this thesis would surely include a study of the finite-duration-pule effect on the detection of larger clusters of nuclear spins and the combined sensor-cluster dynamics. Detection of spin dimers has been demonstrated with the nitrogen vacancy [17, 18] and an interesting question is: do spin dimers present spurious signals also? Of course including detuning errors (from the host nitrogen or inhomogeneous broadening) in this study would be essential for an accurate analysis. A natural extension of considering larger spin clusters is to study the finite-duration-pulse effect on the coherence lifetime of a sensor coupled to an entire spin bath. The available correlated cluster expansion methods [158] for modelling qubit-bath interactions assume instantaneous pulses and it would be worthwhile expanding these techniques to include the finite pule duration.

Our study of the Si:Bi system revealed a highly tunable sensor, with optimal working points - regions where the effective sensor-target coupling is reduced resulting in sharper coherence dips that are valuable for their increased resolution. Future work could include a search to look for these optimal working points in the nitrogen vacancy center or other developing defect systems.

The results presented in Chapter 6 - modelling the detuning error in finite-duration-pulse experiments - raise some further questions for future study. It would be beneficial to quantify the CPMG dip splitting and suppression and this requires an analysis of the generalised modulation function resonances. The presented model is also applicable for studying the finite-duration-pulse effect on classical signals and it would be interesting to compare the difference between the quantum and classical signatures. Several other outstanding questions present themselves: How does the Magnus expansion analysis compare with the Floquet analysis? How does the Hermite pulse achieve its suppression of spurious signals and is this robust to pulse errors? Can we quantify the noise introduced in the randomisation protocol for universally suppressing spurious signals?

The work presented in this thesis provides the necessary basis and tools to answer all these questions as the emerging quantum technology of dynamical decoupling based sensing progresses towards the realisation of functionalised nanoscale NMR and MRI.

A | 2-D Spin Dynamics

A general static 2-D spin Hamiltonian is given by $\hat{H} = \mathbf{h} \cdot \hat{\mathbf{I}}$ where $\hat{\mathbf{I}} = (\hat{I}_x, \hat{I}_y, \hat{I}_z) = \frac{1}{2}(\hat{\sigma}_x, \hat{\sigma}_y, \hat{\sigma}_z)$. (An identity term, $a_0\hat{\mathbb{I}}$, could also be present but this has no effect on the dynamics so can be ignored.) The field $\mathbf{h}$ represents an arbitrary magnetic field felt by the spin and can be written in Cartesian and polar coordinates as $\mathbf{h} = (h_x, h_y, h_z) = r(\sin\theta\cos\phi, \sin\theta\sin\phi, \cos\theta) = r\mathbf{n_h}$ where $|\mathbf{n_h}| = 1$. The Hamiltonian can be diagonalised thus

$$\hat{H} = \begin{pmatrix} \cos\frac{\theta}{2} & -e^{-i\phi}\sin\frac{\theta}{2} \\ e^{i\phi}\sin\frac{\theta}{2} & \cos\frac{\theta}{2} \end{pmatrix} \begin{pmatrix} \frac{r}{2} & 0 \\ 0 & -\frac{r}{2} \end{pmatrix} \begin{pmatrix} \cos\frac{\theta}{2} & e^{-i\phi}\sin\frac{\theta}{2} \\ -e^{i\phi}\sin\frac{\theta}{2} & \cos\frac{\theta}{2} \end{pmatrix}. \tag{A.1}$$

The evolution operator for this Hamiltonian is given by $\hat{U}(t) = \exp(-i\hat{H}t) = \exp(-i\mathbf{h}\cdot\hat{\mathbf{I}}t) = \cos(\frac{rt}{2})\hat{\mathbb{I}} - i\sin(\frac{rt}{2})(\mathbf{n_h}\cdot\hat{\boldsymbol{\sigma}})$ and can be diagonalised thus

$$\hat{U}(t) = \begin{pmatrix} \cos\frac{\theta}{2} & -e^{-i\phi}\sin\frac{\theta}{2} \\ e^{i\phi}\sin\frac{\theta}{2} & \cos\frac{\theta}{2} \end{pmatrix} \begin{pmatrix} e^{-i\frac{rt}{2}} & 0 \\ 0 & e^{+i\frac{rt}{2}} \end{pmatrix} \begin{pmatrix} \cos\frac{\theta}{2} & e^{-i\phi}\sin\frac{\theta}{2} \\ -e^{i\phi}\sin\frac{\theta}{2} & \cos\frac{\theta}{2} \end{pmatrix}. \tag{A.2}$$

Clearly the Hamiltonian and its evolution operator share the same eigenstates which are aligned or anti-aligned with the applied magnetic field, $\mathbf{h}$. If the initial state is not an eigenstate of the Hamiltonian then it will precess about the magnetic field with angular frequency r.

B | Rotating Frames

Here we detail the transformation of a general Hamiltonian, $\hat{H}(t)$, to a frame rotating under a general reference Hamiltonian, $\hat{H}_{\mathrm{r}}(t)$. The Schrödinger equation governing dynamics in the original frame is

$$i\frac{\partial}{\partial t}\left|\psi(t)\right\rangle = \hat{H}(t)\left|\psi(t)\right\rangle . \tag{B.1}$$

To transform to the rotating frame we let

$$\left|\psi(t)\right\rangle = \hat{U}_{\mathrm{r}}(t)\left|\psi'(t)\right\rangle , \tag{B.2}$$

where $\hat{U}_{\mathrm{r}}(t) = \hat{\mathcal{T}}\exp(-i\int_0^t \hat{H}_{\mathrm{r}}(s)ds)$ is the reference evolution operator and $\left|\psi'(t)\right\rangle$ is the state in the rotating frame. Substituting Eq. (B.2) into Eq. (B.1) we obtain

$$i\frac{\partial}{\partial t}(\hat{U}_{\mathrm{r}}(t)\left|\psi'(t)\right\rangle) = \hat{H}(t)\hat{U}_{\mathrm{r}}(t)\left|\psi'(t)\right\rangle , \tag{B.3}$$

$$(i\frac{\partial}{\partial t}\hat{U}_{\mathrm{r}}(t))\left|\psi'(t)\right\rangle + \hat{U}_{\mathrm{r}}(t)(i\frac{\partial}{\partial t}\left|\psi'(t)\right\rangle) = \hat{H}(t)\hat{U}_{\mathrm{r}}(t)\left|\psi'(t)\right\rangle , \tag{B.4}$$

$$(\hat{H}_{\mathrm{r}}(t)\hat{U}_{\mathrm{r}}(t))\left|\psi'(t)\right\rangle + \hat{U}_{\mathrm{r}}(t)(i\frac{\partial}{\partial t}\left|\psi'(t)\right\rangle) = \hat{H}(t)\hat{U}_{\mathrm{r}}(t)\left|\psi'(t)\right\rangle , \tag{B.5}$$

$$\tag{B.6}$$

where we have made use of the product rule for differentiation and the fact that $i\frac{\partial}{\partial t}\hat{U}_{\mathrm{r}}(t) = \hat{H}_{\mathrm{r}}(t)\hat{U}_{\mathrm{r}}(t)$. Next we rearrange the equation and pre multiply by $\hat{U}_{\mathrm{r}}^{\dagger}(t)$ to obtain

$$i\frac{\partial}{\partial t}\left|\psi'(t)\right\rangle = \hat{U}_{\mathrm{r}}^{\dagger}(t)[\hat{H}(t) - \hat{H}_{\mathrm{r}}(t)]\hat{U}_{\mathrm{r}}(t)\left|\psi'(t)\right\rangle \tag{B.7}$$

$$\equiv \hat{H}'(t)\left|\psi'(t)\right\rangle . \tag{B.8}$$

This is the Schrödinger equation for the dynamics in the rotating frame and reveals the transformed Hamiltonian, $\hat{H}'(t) = \hat{U}_{\mathrm{r}}^{\dagger}(t)[\hat{H}(t) - \hat{H}_{\mathrm{r}}(t)]\hat{U}_{\mathrm{r}}(t)$.

C | Spin-1/2 CPMG Evolution

The free evolution under $\hat{H}_{u,d} = \mathbf{h}_{u,d} \cdot \hat{\mathbf{I}}$ where $\mathbf{h}_{u,d} = \omega_{u,d}(\sin\theta_{u,d}, 0, \cos\theta_{u,d})$ is given by

$$\hat{U}^{(0)}_{u,d}(t) = \exp(-i\hat{H}_{u,d}t) = \cos(\frac{\omega_{u,d}t}{2})\hat{\mathbb{I}} - i\sin(\frac{\omega_{u,d}t}{2})(\sin\theta_{u,d}\hat{\sigma}_x + \cos\theta_{u,d}\hat{\sigma}_z), \tag{C.1}$$

as discussed in the previous section, App. A.

The Hahn echo evolution operators are then given by $\hat{U}^{(1)}_u(t = 2\tau) = \hat{U}^{(0)}_u(\tau)\hat{U}^{(0)}_d(\tau)$ and $\hat{U}^{(1)}_d(t = 2\tau) = \hat{U}^{(0)}_d(\tau)\hat{U}^{(0)}_u(\tau)$. Computing the matrix product we find that

$$\hat{U}^{(1)}_u(t = 2\tau) = A_0\hat{\mathbb{I}} - i(A_x\hat{\sigma}_x + A_y\hat{\sigma}_y + A_z\hat{\sigma}_z), \tag{C.2}$$

$$\hat{U}^{(1)}_d(t = 2\tau) = A_0\hat{\mathbb{I}} - i(A_x\hat{\sigma}_x - A_y\hat{\sigma}_y + A_z\hat{\sigma}_z), \tag{C.3}$$

where

$$A_0 = \cos\frac{\omega_u\tau}{2}\cos\frac{\omega_d\tau}{2} - \sin\frac{\omega_u\tau}{2}\sin\frac{\omega_d\tau}{2}\cos(\theta_u - \theta_d), \tag{C.4}$$

$$A_x = \cos\frac{\omega_u\tau}{2}\sin\frac{\omega_d\tau}{2}\sin\theta_d + \cos\frac{\omega_d\tau}{2}\sin\frac{\omega_u\tau}{2}\sin\theta_u, \tag{C.5}$$

$$A_y = -\sin\frac{\omega_u\tau}{2}\sin\frac{\omega_d\tau}{2}\sin(\theta_u - \theta_d), \tag{C.6}$$

$$A_z = \cos\frac{\omega_u\tau}{2}\sin\frac{\omega_d\tau}{2}\cos\theta_d + \cos\frac{\omega_d\tau}{2}\sin\frac{\omega_u\tau}{2}\cos\theta_u. \tag{C.7}$$

The one-period CPMG evolution operator can then be constructed via $\hat{U}^{(2)}_u(t = T = 4\tau) = \hat{U}^{(1)}_u(2\tau)\hat{U}^{(1)}_d(2\tau)$ and $\hat{U}^{(2)}_d(t = T = 4\tau) = \hat{U}^{(1)}_d(2\tau)\hat{U}^{(1)}_u(2\tau)$. Computing the matrix product we find that

$$\hat{U}^{(2)}_u(T) = a_0\hat{\mathbb{I}} - i(a_{ux}\hat{\sigma}_x + a_{uz}\hat{\sigma}_z), \tag{C.8}$$

$$\hat{U}^{(2)}_d(T) = a_0\hat{\mathbb{I}} - i(a_{dx}\hat{\sigma}_x + a_{dz}\hat{\sigma}_z), \tag{C.9}$$

where

$$a_0 = A_0^2 - A_x^2 + A_y^2 - A_z^2 \tag{C.10}$$
$$= \cos\frac{\omega_u T}{4}\cos\frac{\omega_d T}{4} - \sin\frac{\omega_u T}{4}\sin\frac{\omega_d T}{4}\cos(\theta_u - \theta_d),$$
$$a_{ux} = 2(A_0 A_x + A_y A_z), \tag{C.11}$$
$$a_{dx} = 2(A_0 A_x - A_y A_z), \tag{C.12}$$
$$a_{uz} = 2(A_0 A_z - A_y A_x), \tag{C.13}$$
$$a_{dz} = 2(A_0 A_z + A_y A_x). \tag{C.14}$$

The evolution operator can then be diagonalised to obtain the Floquet states and quasienergies

$$\hat{U}^{(2)}_{u,d}(T) = \begin{pmatrix} \cos\frac{\theta^F_{u,d}}{2} & -\sin\frac{\theta^F_{u,d}}{2} \\ \sin\frac{\theta^F_{u,d}}{2} & \cos\frac{\theta^F_{u,d}}{2} \end{pmatrix} \begin{pmatrix} \exp(-i\epsilon T) & 0 \\ 0 & \exp(+i\epsilon T) \end{pmatrix} \begin{pmatrix} \cos\frac{\theta^F_{u,d}}{2} & \sin\frac{\theta^F_{u,d}}{2} \\ -\sin\frac{\theta^F_{u,d}}{2} & \cos\frac{\theta^F_{u,d}}{2} \end{pmatrix} \tag{C.15}$$
$$= \cos\epsilon T\hat{\mathbb{I}} - i\sin\epsilon T(\sin\theta^F_{u,d}\hat{\sigma}_x + \cos\theta^F_{u,d}\hat{\sigma}_z), \tag{C.16}$$

where the Floquet states can be read from the columns of the first matrix and the quasienergies are $\epsilon_1 = -\epsilon_2 \equiv \epsilon$.

The evolution can be described by an effective Hamiltonian, $\hat{U}^{(2)}_{u,d}(T) = \exp(-i\hat{H}^{\text{eff}}_{u,d}T)$, where $\hat{H}^{\text{eff}}_{u,d} = \mathbf{h}^{\text{eff}}_{u,d}\cdot\hat{\mathbf{I}}$ and $\mathbf{h}^{\text{eff}}_{u,d} = 2\epsilon(\cos\theta^F_{u,d}, 0, \sin\theta^F_{u,d})$ so that although the full dynamics within the pulse unit follows some complex path, at stroboscopic times it is equivalent to the rotation of the initial state around the effective field with angular frequency 2ϵ.

Comparing equations Eq. (C.16) and Eq. (C.8),(C.9) we find that the Floquet quasienergy can be obtained from

$$\cos\epsilon T = \cos\frac{\omega_u T}{4}\cos\frac{\omega_d T}{4} - \sin\frac{\omega_u T}{4}\sin\frac{\omega_d T}{4}\cos(\theta_u - \theta_d) \tag{C.17}$$

and the Floquet state angles are given by

$$\tan\theta^F_{u,d} = \frac{a_{u,dx}}{a_{u,dz}}. \tag{C.18}$$

Substituting the Floquet quasienergies and states into the equation for the sensor re-

sponse (Eq. (3.15)) gives

$$\mathcal{L}(N_pT) = 1 - 2\sin^2(\epsilon N_pT)\sin^2\left(\frac{\theta_u^F - \theta_d^F}{2}\right), \tag{C.19}$$

with sensor coherence dips appearing when $\theta_u^F - \theta_d^F = \pi$. i.e. when the effective fields, $\mathbf{h}_{u,d}^{\text{eff}}$, are antiparallel.

Defining the Floquet *phase* as $\varepsilon = \epsilon T$, which is the phase accumulated by the upper state during each period, one can express the sensor response in terms of the Floquet phase entirely, essentially removing $\theta_{u,d}^F$ from the expression. Starting with

$$\sin^2\left(\frac{\theta_u^F - \theta_d^F}{2}\right) = \frac{1}{2}\left(1 - \cos(\theta_u^F - \theta_d^F)\right) \tag{C.20}$$

$$= \frac{1}{2}\left(1 - \left(\cos\theta_u^F\cos\theta_d^F + \sin\theta_u^F\sin\theta_d^F\right)\right) \tag{C.21}$$

$$= \frac{1}{2}\left(1 - \left(\frac{a_{uz}a_{dz} + a_{ux}a_{dx}}{1 - a_0^2}\right)\right), \tag{C.22}$$

where in the last line we have used that $\cos\theta_{u,d}^F = a_{u,dz}/\sqrt{1-a_0^2}$ and $\sin\theta_{u,d}^F = a_{u,dx}/\sqrt{1-a_0^2}$. Next we utilise the expressions Eq. C.11 to find

$$\sin^2\left(\frac{\theta_u^F - \theta_d^F}{2}\right) = \frac{A_y^2}{A_0^2 + A_y^2}. \tag{C.23}$$

Finally we use that $a_0 = \cos(\varepsilon(T))$, $A_0 = \cos(\varepsilon(T/2))$ and $a_0 = 2(A_0^2 + A_y^2) - 1$ to obtain

$$\mathcal{L}(N_pT) = 1 - 2\sin^2(N_p\varepsilon(T))\left[\frac{\cos^2(\varepsilon(T)/2) - \cos^2(\varepsilon(T/2))}{\cos^2(\varepsilon(T)/2)}\right], \tag{C.24}$$

which is completely determined by the Floquet phase, ε. The dip condition in this case is satisfied when $\varepsilon(T_{\text{dip}}/2) = \pi/2$.

Bibliography

[1] Nan Zhao, Jan Honert, Bernhard Schmid, Michael Klas, Junichi Isoya, Matthew Markham, Daniel Twitchen, Fedor Jelezko, Ren-Bao Liu, Helmut Fedder, and Jörg Wrachtrup. Sensing single remote nuclear spins. *Nature nanotechnology*, 7(10):657–662, 2012.

[2] Shimon Kolkowitz, Quirin P Unterreithmeier, Steven D Bennett, and Mikhail D Lukin. Sensing distant nuclear spins with a single electron spin. *Physical review letters*, 109(13):137601, 2012.

[3] TH Taminiau, JJT Wagenaar, T Van der Sar, F Jelezko, Viatcheslav V Dobrovitski, and R Hanson. Detection and control of individual nuclear spins using a weakly coupled electron spin. *Physical review letters*, 109(13):137602, 2012.

[4] JM Taylor, P Cappellaro, L Childress, L Jiang, D Budker, PR Hemmer, A Yacoby, R Walsworth, and MD Lukin. High-sensitivity diamond magnetometer with nanoscale resolution. *Nature Physics*, 4(10):810–816, 2008.

[5] CL Degen. Scanning magnetic field microscope with a diamond single-spin sensor. *Applied Physics Letters*, 92(24):243111, 2008.

[6] Jianming Cai, Fedor Jelezko, Martin B Plenio, and Alex Retzker. Diamond-based single-molecule magnetic resonance spectroscopy. *New Journal of Physics*, 15(1):013020, 2013.

[7] Paul T. Callaghan. *Principles of nuclear magnetic resonance microscopy*. Oxford University Press on Demand, 1993.

[8] Ettore Bernardi, Richard Nelz, Selda Sonusen, and Elke Neu. Nanoscale sensing using point defects in single-crystal diamond: Recent progress on nitrogen vacancy center-based sensors. *Crystals*, 7(5):124, 2017.

[9] Jonas Nils Becker and Christoph Becher. Coherence properties and quantum control of silicon vacancy color centers in diamond. *Physica status solidi (a)*, 214(11), 2017.

[10] Matthias Widmann, Sang-Yun Lee, Torsten Rendler, Nguyen Tien Son, Helmut Fedder, Seoyoung Paik, Li-Ping Yang, Nan Zhao, Sen Yang, Ian Booker, Andrej Denisenko, Mohammad Jamali, S. Ali Momenzadeh, Ilja Gerhardt, Takeshi Ohshima, Adam Gali, Erik Janzén, and Jörg Wrachtrup. Coherent control of single spins in silicon carbide at room temperature. *Nature materials*, 14(2):164–168, 2015.

[11] Andrea Morello, Jarryd J Pla, Floris A Zwanenburg, Kok W Chan, Kuan Y Tan, Hans Huebl, Mikko Möttönen, Christopher D Nugroho, Changyi Yang, Jessica A van Donkelaar, Andrew D C Alves, David N Jamieson, Christopher C Escott, Lloyd C L Hollenburg, Robert G Clark, and Andrew S Dzurak. Single-shot readout of an electron spin in silicon. *Nature*, 467(7316):687–691, 2010.

[12] Yuzhou Wu, Fedor Jelezko, Martin B Plenio, and Tanja Weil. Diamond quantum devices in biology. *Angewandte Chemie International Edition*, 55(23):6586–6598, 2016.

[13] Fedor Jelezko, T Gaebel, I Popa, M Domhan, A Gruber, and Jorg Wrachtrup. Observation of coherent oscillation of a single nuclear spin and realization of a two-qubit conditional quantum gate. *Physical Review Letters*, 93(13):130501, 2004.

[14] L Childress, MV Gurudev Dutt, JM Taylor, AS Zibrov, F Jelezko, J Wrachtrup, PR Hemmer, and MD Lukin. Coherent dynamics of coupled electron and nuclear spin qubits in diamond. *Science*, 314(5797):281–285, 2006.

[15] A Dréau, J-R Maze, M Lesik, J-F Roch, and V Jacques. High-resolution spectroscopy of single NV defects coupled with nearby 13 C nuclear spins in diamond. *Physical Review B*, 85(13):134107, 2012.

[16] Lorenza Viola, Emanuel Knill, and Seth Lloyd. Dynamical decoupling of open quantum systems. *Physical Review Letters*, 82(12):2417, 1999.

[17] Nan Zhao, Jian-Liang Hu, Sai-Wah Ho, Jones TK Wan, and RB Liu. Atomic-scale magnetometry of distant nuclear spin clusters via nitrogen-vacancy spin in diamond. *Nature nanotechnology*, 6(4):242–246, 2011.

[18] Fazhan Shi, Xi Kong, Pengfei Wang, Fei Kong, Nan Zhao, Ren-Bao Liu, and Jiangfeng Du. Sensing and atomic-scale structure analysis of single nuclear-spin clusters in diamond. *Nature Physics*, 10(1):21–25, 2014.

[19] Michael Sean Grinolds, Sungkun Hong, Patrick Maletinsky, Lan Luan, Mikhail D Lukin, Ronald Lee Walsworth, and Amir Yacoby. Nanoscale magnetic imaging of a single electron spin under ambient conditions. *Nature Physics*, 9(4):215–219, 2013.

[20] MS Grinolds, M Warner, Kristiaan De Greve, Yuliya Dovzhenko, L Thiel, Ronald Lee Walsworth, S Hong, P Maletinsky, and Amir Yacoby. Subnanometre resolution in three-dimensional magnetic resonance imaging of individual dark spins. *Nature nanotechnology*, 9(4):279, 2014.

[21] T. Staudacher, F. Shi, S. Pezzagna, J. Meijer, J. Du, C. A. Meriles, F. Reinhard, and J. Wrachtrup. Nuclear magnetic resonance spectroscopy on a (5-nanometer)^3 sample volume. *Science*, 339(6119):561–563, 2013.

[22] HJ Mamin, M Kim, MH Sherwood, CT Rettner, K Ohno, DD Awschalom, and D Rugar. Nanoscale nuclear magnetic resonance with a nitrogen-vacancy spin sensor. *Science*, 339(6119):557–560, 2013.

[23] D Rugar, HJ Mamin, MH Sherwood, M Kim, CT Rettner, K Ohno, and DD Awschalom. Proton magnetic resonance imaging using a nitrogen–vacancy spin sensor. *Nature nanotechnology*, 10(2):120–124, 2015.

[24] C Müller, X Kong, J-M Cai, K Melentijević, A Stacey, M Markham, D Twitchen, J Isoya, S Pezzagna, J Meijer, J F Du, M B Plenio, B Naydenov, L P McGuinness, and F Jelezko. Nuclear magnetic resonance spectroscopy with single spin sensitivity. *Nature communications*, 5:4703, 2014.

[25] A. O. Sushkov, I. Lovchinsky, N. Chisholm, R. L. Walsworth, H. Park, and M. D. Lukin. Magnetic resonance detection of individual proton spins using quantum reporters. *Phys. Rev. Lett.*, 113:197601, 2014.

[26] Igor Lovchinsky, AO Sushkov, E Urbach, NP de Leon, Soonwon Choi, Kristiaan De Greve, R Evans, R Gertner, E Bersin, C Müller, L McGuinness, F Jelezko, RL Walsworth, H Park, and MD Lukin. Nuclear magnetic resonance detection and spectroscopy of single proteins using quantum logic. *Science*, 351(6275):836–841, 2016.

[27] MV Gurudev Dutt, L Childress, L Jiang, E Togan, J Maze, F Jelezko, AS Zibrov, PR Hemmer, and MD Lukin. Quantum register based on individual electronic and nuclear spin qubits in diamond. *Science*, 316(5829):1312–1316, 2007.

[28] P Neumann, N Mizuochi, F Rempp, Philip Hemmer, H Watanabe, S Yamasaki, V Jacques, Torsten Gaebel, F Jelezko, and J Wrachtrup. Multipartite entanglement among single spins in diamond. *Science*, 320(5881):1326–1329, 2008.

[29] Philipp Neumann, Johannes Beck, Matthias Steiner, Florian Rempp, Helmut Fedder, Philip R Hemmer, Jörg Wrachtrup, and Fedor Jelezko. Single-shot readout of a single nuclear spin. *Science*, 329(5991):542–544, 2010.

[30] Tim Hugo Taminiau, Julia Cramer, Toeno van der Sar, Viatcheslav V Dobrovitski, and Ronald Hanson. Universal control and error correction in multi-qubit spin registers in diamond. *Nature nanotechnology*, 9(3):171–176, 2014.

[31] Thaddeus D Ladd, Fedor Jelezko, Raymond Laflamme, Yasunobu Nakamura, Christopher Monroe, and Jeremy Lloyd O'Brien. Quantum computers. *Nature*, 464(7285):45, 2010.

[32] Sebastian Zaiser, Torsten Rendler, Ingmar Jakobi, Thomas Wolf, Sang-Yun Lee, Samuel Wagner, Ville Bergholm, Thomas Schulte-Herbrüggen, Philipp Neumann, and Jörg Wrachtrup. Enhancing quantum sensing sensitivity by a quantum memory. *Nature communications*, 7:12279, 2016.

[33] Matthias Pfender, Nabeel Aslam, Hitoshi Sumiya, Shinobu Onoda, Philipp Neumann, Junichi Isoya, Carlos A Meriles, and Jörg Wrachtrup. Nonvolatile nuclear spin memory enables sensor-unlimited nanoscale spectroscopy of small spin clusters. *Nature Communications*, 8(1):834, 2017.

[34] Brendan John Shields, QP Unterreithmeier, NP De Leon, H Park, and Mikhail D Lukin. Efficient readout of a single spin state in diamond via spin-to-charge conversion. *Physical review letters*, 114(13):136402, 2015.

[35] Gonzalo A Álvarez and Dieter Suter. Measuring the spectrum of colored noise by dynamical decoupling. *Physical review letters*, 107(23):230501, 2011.

[36] Łukasz Cywiński, Roman M Lutchyn, Cody P Nave, and S Das Sarma. How to en-

hance dephasing time in superconducting qubits. *Physical Review B*, 77(17):174509, 2008.

[37] Wen-Long Ma and Ren-Bao Liu. Angstrom-resolution magnetic resonance imaging of single molecules via wave-function fingerprints of nuclear spins. *Phys. Rev. Applied*, 6:024019, 2016.

[38] Andreas Albrecht and Martin B. Plenio. Filter design for hybrid spin gates. *Phys. Rev. A*, 92:022340, 2015.

[39] J Casanova, Z-Y Wang, JF Haase, and MB Plenio. Robust dynamical decoupling sequences for individual-nuclear-spin addressing. *Physical Review A*, 92(4):042304, 2015.

[40] Jon H Shirley. Solution of the Schrödinger equation with a Hamiltonian periodic in time. *Physical Review*, 138(4B):B979, 1965.

[41] Michal Leskes, PK Madhu, and Shimon Vega. Floquet theory in solid-state nuclear magnetic resonance. *Progress in nuclear magnetic resonance spectroscopy*, 57(4):345–380, 2010.

[42] M. Loretz, J. M. Boss, T. Rosskopf, H. J. Mamin, D. Rugar, and C. L. Degen. Spurious harmonic response of multipulse quantum sensing sequences. *Phys. Rev. X*, 5:021009, 2015.

[43] JF Haase, Z-Y Wang, J Casanova, and MB Plenio. Pulse-phase control for spectral disambiguation in quantum sensing protocols. *Physical Review A*, 94(3):032322, 2016.

[44] Zijun Shu, Zhendong Zhang, Qingyun Cao, Pengcheng Yang, Martin B Plenio, Christoph Müller, Johannes Lang, Nikolas Tomek, Boris Naydenov, Liam P McGuinness, Fedor Jelezko, and Jianming Cai. Unambiguous nuclear spin detection using an engineered quantum sensing sequence. *Physical Review A*, 96(5):051402, 2017.

[45] Götz S Uhrig and Stefano Pasini. Efficient coherent control by sequences of pulses of finite duration. *New Journal of Physics*, 12(4):045001, 2010.

[46] CA Ryan, JS Hodges, and DG Cory. Robust decoupling techniques to extend quantum coherence in diamond. *Physical Review Letters*, 105(20):200402, 2010.

[47] Alexandre M Souza, Gonzalo A Álvarez, and Dieter Suter. Robust dynamical decoupling for quantum computing and quantum memory. *Physical review letters*, 106(24):240501, 2011.

[48] JH Shim, I Niemeyer, J Zhang, and D Suter. Robust dynamical decoupling for arbitrary quantum states of a single NV center in diamond. *EPL (Europhysics Letters)*, 99(4):40004, 2012.

[49] J. E. Lang, R. B. Liu, and T. S. Monteiro. Dynamical-decoupling-based quantum sensing: Floquet spectroscopy. *Phys. Rev. X*, 5:041016, 2015.

[50] J. E. Lang, J. Casanova, Z.-Y. Wang, M. B. Plenio, and T. S. Monteiro. Enhanced resolution in nanoscale NMR via quantum sensing with pulses of finite duration. *Phys. Rev. Applied*, 7:054009, 2017.

[51] A. Pontin, J. E. Lang, A. Chowdhury, P. Vezio, F. Marino, B. Morana, E. Serra, F. Marin, and T. S. Monteiro. Imaging correlations in heterodyne spectra for quantum displacement sensing. *Phys. Rev. Lett.*, 120:020503, 2018.

[52] MJ Akram, EB Aranas, NP Bullier, JE Lang, and TS Monteiro. Two-timescale stochastic langevin for quantum nonlinear optomechanics. *arXiv preprint arXiv:1801.08700*, 2018.

[53] Richard R Ernst, Geoffrey Bodenhausen, and Alexander Wokaun. *Principles of nuclear magnetic resonance in one and two dimensions*, volume 14. Clarendon Press Oxford, 1987.

[54] E Mark Haacke, Robert W Brown, Michael R Thompson, and Ramesh Venkatesan. *Magnetic resonance imaging: physical principles and sequence design*, volume 82. Wiley-Liss New York:, 1999.

[55] Daniel Rugar, R Budakian, HJ Mamin, and BW Chui. Single spin detection by magnetic resonance force microscopy. *Nature*, 430(6997):329, 2004.

[56] HJ Mamin, M Poggio, CL Degen, and D Rugar. Nuclear magnetic resonance imaging with 90-nm resolution. *Nature nanotechnology*, 2(5):301, 2007.

[57] CL Degen, M Poggio, HJ Mamin, CT Rettner, and D Rugar. Nanoscale magnetic resonance imaging. *Proceedings of the National Academy of Sciences*, 106(5):1313–1317, 2009.

[58] Ya S Greenberg. Application of superconducting quantum interference devices to nuclear magnetic resonance. *Reviews of Modern Physics*, 70(1):175, 1998.

[59] Denis Vasyukov, Yonathan Anahory, Lior Embon, Dorri Halbertal, Jo Cuppens, Lior Neeman, Amit Finkler, Yehonathan Segev, Yuri Myasoedov, Michael L Rappaport, Martin E Huber, and Eli Zeldov. A scanning superconducting quantum interference device with single electron spin sensitivity. *Nature nanotechnology*, 8(9):639, 2013.

[60] Dmitry Budker and Michael Romalis. Optical magnetometry. *Nature Physics*, 3(4):227, 2007.

[61] Jörg Wrachtrup and Amit Finkler. Single spin magnetic resonance. *Journal of Magnetic Resonance*, 269:225 – 236, 2016.

[62] I Aharonovich, S Castelletto, DA Simpson, CH Su, AD Greentree, and S Prawer. Diamond-based single-photon emitters. *Reports on progress in Physics*, 74(7):076501, 2011.

[63] FP Bundy, H Tracy Hall, HM Strong, and RH Wentorf Jun. Man-made diamonds. *Nature*, 176(4471):51, 1955.

[64] Seiichiro Matsumoto, Yoichiro Sato, Masayuki Tsutsumi, and Nobuo Setaka. Growth of diamond particles from methane-hydrogen gas. *Journal of Materials Science*, 17(11):3106–3112, 1982.

[65] Yu-Chen Chen, Patrick S Salter, Sebastian Knauer, Laiyi Weng, Angelo C Frangeskou, Colin J Stephen, Shazeaa N Ishmael, Philip R Dolan, Sam Johnson, Ben L Green, Gavin W Morley, John G Newton, Mark E an Rarity, Martin J Booth, and Jason M Smith. Laser writing of coherent colour centres in diamond. *Nature Photonics*, 11(2):77, 2017.

[66] A Gruber, A Dräbenstedt, C Tietz, L Fleury, J Wrachtrup, and C Von Borczyskowski. Scanning confocal optical microscopy and magnetic resonance on single defect centers. *Science*, 276(5321):2012–2014, 1997.

[67] Gopalakrishnan Balasubramanian, Philipp Neumann, Daniel Twitchen, Matthew Markham, Roman Kolesov, Norikazu Mizuochi, Junichi Isoya, Jocelyn Achard, Johannes Beck, Julia Tissler, Vincent Jacques, Philip R. Hemmer, Fedor Jelezko, and

Jörg Wrachtrup. Ultralong spin coherence time in isotopically engineered diamond. *Nature materials*, 8(5):383–387, 2009.

[68] Lucio Robledo, Lilian Childress, Hannes Bernien, Bas Hensen, Paul FA Alkemade, and Ronald Hanson. High-fidelity projective read-out of a solid-state spin quantum register. *Nature*, 477(7366):574–578, 2011.

[69] Andrei Faraon, Charles Santori, Zhihong Huang, Victor M. Acosta, and Raymond G. Beausoleil. Coupling of nitrogen-vacancy centers to photonic crystal cavities in monocrystalline diamond. *Phys. Rev. Lett.*, 109:033604, 2012.

[70] G De Lange, ZH Wang, D Riste, VV Dobrovitski, and R Hanson. Universal dynamical decoupling of a single solid-state spin from a spin bath. *Science*, 330(6000):60–63, 2010.

[71] Nan Zhao, Sai-Wah Ho, and Ren-Bao Liu. Decoherence and dynamical decoupling control of nitrogen vacancy center electron spins in nuclear spin baths. *Physical Review B*, 85(11):115303, 2012.

[72] Nir Bar-Gill, Linh M Pham, Andrejs Jarmola, Dmitry Budker, and Ronald L Walsworth. Solid-state electronic spin coherence time approaching one second. *Nature communications*, 4:1743, 2013.

[73] Mohamed H Abobeih, Julia Cramer, Michiel A Bakker, Norbert Kalb, Daniel J Twitchen, Matthew Markham, and Tim H Taminiau. One-second coherence for a single electron spin coupled to a multi-qubit nuclear-spin environment. *Nature Communications*, 9(2552), 2018.

[74] JR Maze, PL Stanwix, JS Hodges, S Hong, JM Taylor, P Cappellaro, L Jiang, MV Gurudev Dutt, E Togan, AS Zibrov, A Yacoby, RL Walsworth, and MD Lukin. Nanoscale magnetic sensing with an individual electronic spin in diamond. *Nature*, 455(7213):644, 2008.

[75] G De Lange, D Ristè, VV Dobrovitski, and R Hanson. Single-spin magnetometry with multipulse sensing sequences. *Physical Review Letters*, 106(8):080802, 2011.

[76] Eric Van Oort and Max Glasbeek. Electric-field-induced modulation of spin echoes of NV centers in diamond. *Chemical Physics Letters*, 168(6):529–532, 1990.

[77] Florian Dolde, Helmut Fedder, Marcus W Doherty, Tobias Nöbauer, Florian Rempp, Gopalakrishnan Balasubramanian, Thomas Wolf, Friedemann Reinhard, Lloyd CL Hollenberg, Fedor Jelezko, and Jörg Wrachtrup. Electric-field sensing using single diamond spins. *Nature Physics*, 7(6):459, 2011.

[78] Preeti Ovartchaiyapong, Kenneth W Lee, Bryan A Myers, and Ania C Bleszynski Jayich. Dynamic strain-mediated coupling of a single diamond spin to a mechanical resonator. *Nature communications*, 5:4429, 2014.

[79] VM Acosta, E Bauch, MP Ledbetter, A Waxman, L-S Bouchard, and D Budker. Temperature dependence of the nitrogen-vacancy magnetic resonance in diamond. *Physical review letters*, 104(7):070801, 2010.

[80] X-D Chen, C-H Dong, F-W Sun, C-L Zou, J-M Cui, Z-F Han, and G-C Guo. Temperature dependent energy level shifts of nitrogen-vacancy centers in diamond. *Applied Physics Letters*, 99(16):161903, 2011.

[81] P. Neumann, I. Jakobi, F. Dolde, C. Burk, R. Reuter, G. Waldherr, J. Honert, T. Wolf, A. Brunner, J. H. Shim, D. Suter, H. Sumiya, J. Isoya, and J. Wrachtrup. High-precision nanoscale temperature sensing using single defects in diamond. *Nano Letters*, 13(6):2738–2742, 2013.

[82] D Maclaurin, MW Doherty, LCL Hollenberg, and AM Martin. Measurable quantum geometric phase from a rotating single spin. *Physical review letters*, 108(24):240403, 2012.

[83] MP Ledbetter, Kasper Jensen, Ran Fischer, Andrey Jarmola, and Dmitry Budker. Gyroscopes based on nitrogen-vacancy centers in diamond. *Physical Review A*, 86(5):052116, 2012.

[84] Ashok Ajoy and Paola Cappellaro. Stable three-axis nuclear-spin gyroscope in diamond. *Physical Review A*, 86(6):062104, 2012.

[85] Marcus W. Doherty, Viktor V. Struzhkin, David A. Simpson, Liam P. McGuinness, Yufei Meng, Alastair Stacey, Timothy J. Karle, Russell J. Hemley, Neil B. Manson, Lloyd C. L. Hollenberg, and Steven Prawer. Electronic properties and metrology applications of the diamond NV^- center under pressure. *Phys. Rev. Lett.*, 112:047601, 2014.

[86] D Le Sage, K Arai, DR Glenn, SJ DeVience, LM Pham, L Rahn-Lee, MD Lukin, A Yacoby, A Komeili, and RL Walsworth. Optical magnetic imaging of living cells. *Nature*, 496(7446):486, 2013.

[87] David R Glenn, Kyungheon Lee, Hongkun Park, Ralph Weissleder, Amir Yacoby, Mikhail D Lukin, Hakho Lee, Ronald L Walsworth, and Colin B Connolly. Single-cell magnetic imaging using a quantum diamond microscope. *Nature methods*, 12(8):736, 2015.

[88] Chi-Cheng Fu, Hsu-Yang Lee, Kowa Chen, Tsong-Shin Lim, Hsiao-Yun Wu, Po-Keng Lin, Pei-Kuen Wei, Pei-Hsi Tsao, Huan-Cheng Chang, and Wunshain Fann. Characterization and application of single fluorescent nanodiamonds as cellular biomarkers. *Proceedings of the National Academy of Sciences*, 104(3):727–732, 2007.

[89] Georg Kucsko, PC Maurer, Norman Ying Yao, Michael Kubo, HJ Noh, PK Lo, Hongkun Park, and Mikhail D Lukin. Nanometre-scale thermometry in a living cell. *Nature*, 500(7460):54, 2013.

[90] LT Hall, GCG Beart, EA Thomas, DA Simpson, LP McGuinness, JH Cole, JH Manton, RE Scholten, Fedor Jelezko, Jörg Wrachtrup, S Petrou, and L C L Hollenburg. High spatial and temporal resolution wide-field imaging of neuron activity using quantum NV-diamond. *Scientific reports*, 2:401, 2012.

[91] John F Barry, Matthew J Turner, Jennifer M Schloss, David R Glenn, Yuyu Song, Mikhail D Lukin, Hongkun Park, and Ronald L Walsworth. Optical magnetic detection of single-neuron action potentials using quantum defects in diamond. *Proceedings of the National Academy of Sciences*, 113(49):14133–14138, 2016.

[92] Gopalakrishnan Balasubramanian, IY Chan, Roman Kolesov, Mohannad Al-Hmoud, Julia Tisler, Chang Shin, Changdong Kim, Aleksander Wojcik, Philip R Hemmer, Anke Krueger, Tobias Hanke, Alfred Leitenstorfer, Rudolf Bratschitsch, Fedor Jelezko, and Jörg Wrachtrup. Nanoscale imaging magnetometry with diamond spins under ambient conditions. *Nature*, 455(7213):648–651, 2008.

[93] Zhen-Yu Wang, Jan F Haase, Jorge Casanova, and Martin B Plenio. Positioning nuclear spins in interacting clusters for quantum technologies and bioimaging. *Physical Review B*, 93(17):174104, 2016.

[94] Wenchao Ma, Fazhan Shi, Kebiao Xu, Pengfei Wang, Xiangkun Xu, Xing Rong, Chenyong Ju, Chang-Kui Duan, Nan Zhao, and Jiangfeng Du. Resolving remote nuclear spins in a noisy bath by dynamical decoupling design. *Phys. Rev. A*, 92:033418, 2015.

[95] Nan Zhao, Jörg Wrachtrup, and Ren-Bao Liu. Dynamical decoupling design for identifying weakly coupled nuclear spins in a bath. *Phys. Rev. A*, 90:032319, 2014.

[96] Wen-Long Ma and Ren-Bao Liu. Proposal for quantum sensing based on two-dimensional dynamical decoupling: NMR correlation spectroscopy of single molecules. *Phys. Rev. Applied*, 6:054012, 2016.

[97] Xi Kong, Alexander Stark, Jiangfeng Du, Liam P McGuinness, and Fedor Jelezko. Towards chemical structure resolution with nanoscale nuclear magnetic resonance spectroscopy. *Physical Review Applied*, 4(2):024004, 2015.

[98] Abdelghani Laraoui, Florian Dolde, Christian Burk, Friedemann Reinhard, Jörg Wrachtrup, and Carlos A Meriles. High-resolution correlation spectroscopy of 13 C spins near a nitrogen-vacancy centre in diamond. *Nature communications*, 4:1651, 2013.

[99] Jens M Boss, KS Cujia, Jonathan Zopes, and Christian L Degen. Quantum sensing with arbitrary frequency resolution. *Science*, 356(6340):837–840, 2017.

[100] Simon Schmitt, Tuvia Gefen, Felix M Stürner, Thomas Unden, Gerhard Wolff, Christoph Müller, Jochen Scheuer, Boris Naydenov, Matthew Markham, Sebastien Pezzagna, Jan Meijer, Ilia Schwarz, Martin B Plenio, Alex Retzker, Liam P McGuinness, and Fedor Jelezko. Submillihertz magnetic spectroscopy performed with a nanoscale quantum sensor. *Science*, 356(6340):832–837, 2017.

[101] Thomas Wolf, Philipp Neumann, Kazuo Nakamura, Hitoshi Sumiya, Takeshi Ohshima, Junichi Isoya, and Jörg Wrachtrup. Subpicotesla diamond magnetometry. *Physical Review X*, 5(4):041001, 2015.

[102] Stephen J DeVience, Linh M Pham, Igor Lovchinsky, Alexander O Sushkov, Nir Bar-Gill, Chinmay Belthangady, Francesco Casola, Madeleine Corbett, Huiliang Zhang, Mikhail Lukin, Hongkun Park, Amir Yacoby, and Ronald L Walsworth. Nanoscale NMR spectroscopy and imaging of multiple nuclear species. *Nature nanotechnology*, 10(2):129–134, 2015.

[103] Levi P Neukirch, Jan Gieseler, Romain Quidant, Lukas Novotny, and A Nick Vamivakas. Observation of nitrogen vacancy photoluminescence from an optically levitated nanodiamond. *Optics letters*, 38(16):2976–2979, 2013.

[104] M. Scala, M. S. Kim, G. W. Morley, P. F. Barker, and S. Bose. Matter-wave interferometry of a levitated thermal nano-oscillator induced and probed by a spin. *Phys. Rev. Lett.*, 111:180403, 2013.

[105] Andreas Albrecht, Alex Retzker, and Martin B. Plenio. Testing quantum gravity by nanodiamond interferometry with nitrogen-vacancy centers. *Phys. Rev. A*, 90:033834, 2014.

[106] Hannes Bernien, Bas Hensen, Wolfgang Pfaff, Gerwin Koolstra, MS Blok, Lucio Robledo, TH Taminiau, Matthew Markham, DJ Twitchen, Lilian Childress, and Ronald Hanson. Heralded entanglement between solid-state qubits separated by three metres. *Nature*, 497(7447):86, 2013.

[107] Bas Hensen, Hannes Bernien, Anaïs E Dréau, Andreas Reiserer, Norbert Kalb, Machiel S Blok, Just Ruitenberg, Raymond FL Vermeulen, Raymond N Schouten, Carlos Abellán, W Amaya, V Pruneri, M W Mitchell, M Markham, D J Twitchen, D Elkouss, S Wehner, T Taminiau, and R Hanson. Loophole-free bell inequality violation using electron spins separated by 1.3 kilometres. *Nature*, 526(7575):682–686, 2015.

[108] Jonathan D Breeze, Enrico Salvadori, Juna Sathian, Neil McN Alford, and Christopher WM Kay. Continuous-wave room-temperature diamond maser. *Nature*, 555(7697):493, 2018.

[109] Paz London, J Scheuer, J-M Cai, I Schwarz, A Retzker, Martin B Plenio, M Katagiri, T Teraji, S Koizumi, J Isoya, R Fischer, Liam P McGuinness, B Naydenov, and Fedor Jelezko. Detecting and polarizing nuclear spins with double resonance on a single electron spin. *Physical review letters*, 111(6):067601, 2013.

[110] Daniel Abrams, Matthew E Trusheim, Dirk R Englund, Mark D Shattuck, and Carlos A Meriles. Dynamic nuclear spin polarization of liquids and gases in contact with nanostructured diamond. *Nano letters*, 14(5):2471–2478, 2014.

[111] Jonathan P King, Keunhong Jeong, Christophoros C Vassiliou, Chang S Shin, Ralph H Page, Claudia E Avalos, Hai-Jing Wang, and Alexander Pines. Room-

temperature in situ nuclear spin hyperpolarization from optically pumped nitrogen vacancy centres in diamond. *Nature communications*, 6:8965, 2015.

[112] Q Chen, I Schwarz, Fedor Jelezko, A Retzker, and Martin B Plenio. Optical hyperpolarization of C 13 nuclear spins in nanodiamond ensembles. *Physical Review B*, 92(18):184420, 2015.

[113] Q. Chen, I. Schwarz, F. Jelezko, A. Retzker, and M. B. Plenio. Resonance-inclined optical nuclear spin polarization of liquids in diamond structures. *Phys. Rev. B*, 93:060408, 2016.

[114] Jianming Cai, Fedor Jelezko, and Martin B Plenio. Hybrid sensors based on colour centres in diamond and piezoactive layers. *Nature communications*, 5:4065, 2014.

[115] Ning Wang, Gang-Qin Liu, Weng-Hang Leong, Hualing Zeng, Xi Feng, Si-Hong Li, Florian Dolde, Helmut Fedder, Jörg Wrachtrup, Xiao-Dong Cui, Sen Yang, Quan Li, and Ren-Bao Liu. Magnetic criticality enhanced hybrid nanodiamond thermometer under ambient conditions. *Physical Review X*, 8(1):011042, 2018.

[116] Takayuki Iwasaki, Fumitaka Ishibashi, Yoshiyuki Miyamoto, Yuki Doi, Satoshi Kobayashi, Takehide Miyazaki, Kosuke Tahara, Kay D Jahnke, Lachlan J Rogers, Boris Naydenov, Fedor Jelezko, Satoshi Yamasaki, Shinji Nagamachi, Toshiro Inubushi, Norikazu Mizuochi, and Mutsuko Hatano. Germanium-vacancy single color centers in diamond. *Scientific reports*, 5:12882, 2015.

[117] Petr Siyushev, Mathias H. Metsch, Aroosa Ijaz, Jan M. Binder, Mihir K. Bhaskar, Denis D. Sukachev, Alp Sipahigil, Ruffin E. Evans, Christian T. Nguyen, Mikhail D. Lukin, Philip R. Hemmer, Yuri N. Palyanov, Igor N. Kupriyanov, Yuri M. Borzdov, Lachlan J. Rogers, and Fedor Jelezko. Optical and microwave control of germanium-vacancy center spins in diamond. *Phys. Rev. B*, 96:081201, 2017.

[118] Takayuki Iwasaki, Yoshiyuki Miyamoto, Takashi Taniguchi, Petr Siyushev, Mathias H Metsch, Fedor Jelezko, and Mutsuko Hatano. Tin-vacancy quantum emitters in diamond. *Physical review letters*, 119(25):253601, 2017.

[119] S Ditalia Tchernij, Tobias Herzig, Jacopo Forneris, J Küpper, Sébastien Pezzagna, Paolo Traina, Ekaterina Moreva, Ivo Pietro Degiovanni, Giorgio Brida, Natko Skukan, M Genovese, M Jakšić, J Meijer, and P Olivero. Single-photon-emitting

optical centers in diamond fabricated upon Sn implantation. *ACS Photonics*, 4(10):2580–2586, 2017.

[120] Li-Ping Yang, Christian Burk, Matthias Widmann, Sang-Yun Lee, Jörg Wrachtrup, and Nan Zhao. Electron spin decoherence in silicon carbide nuclear spin bath. *Physical Review B*, 90(24):241203, 2014.

[121] David J Christle, Abram L Falk, Paolo Andrich, Paul V Klimov, Jawad Ul Hassan, Nguyen T Son, Erik Janzén, Takeshi Ohshima, and David D Awschalom. Isolated electron spins in silicon carbide with millisecond coherence times. *Nature materials*, 14(2):160, 2015.

[122] Alexei M Tyryshkin, Shinichi Tojo, John JL Morton, Helge Riemann, Nikolai V Abrosimov, Peter Becker, Hans-Joachim Pohl, Thomas Schenkel, Michael LW Thewalt, Kohei M Itoh, and S A Lyon. Electron spin coherence exceeding seconds in high-purity silicon. *Nature materials*, 11(2):143–147, 2012.

[123] Gary Wolfowicz, Alexei M Tyryshkin, Richard E George, Helge Riemann, Nikolai V Abrosimov, Peter Becker, Hans-Joachim Pohl, Mike LW Thewalt, Stephen A Lyon, and John JL Morton. Atomic clock transitions in silicon-based spin qubits. *Nature nanotechnology*, 8(8):561, 2013.

[124] MH Mohammady, GW Morley, and TS Monteiro. Bismuth qubits in silicon: the role of EPR cancellation resonances. *Physical review letters*, 105(6):067602, 2010.

[125] SJ Balian, Gary Wolfowicz, John JL Morton, and TS Monteiro. Quantum-bath-driven decoherence of mixed spin systems. *Physical Review B*, 89(4):045403, 2014.

[126] Gavin W Morley, Petra Lueders, M Hamed Mohammady, Setrak J Balian, Gabriel Aeppli, Christopher WM Kay, Wayne M Witzel, Gunnar Jeschke, and Tania S Monteiro. Quantum control of hybrid nuclear–electronic qubits. *Nature materials*, 12(2):103–107, 2013.

[127] Jarryd J Pla, Kuan Y Tan, Juan P Dehollain, Wee H Lim, John JL Morton, Floris A Zwanenburg, David N Jamieson, Andrew S Dzurak, and Andrea Morello. High-fidelity readout and control of a nuclear spin qubit in silicon. *Nature*, 496(7445):334–338, 2013.

[128] Jarryd J Pla, Fahd A Mohiyaddin, Kuan Y Tan, Juan P Dehollain, Rajib Rahman, Gerhard Klimeck, David N Jamieson, Andrew S Dzurak, and Andrea Morello. Coherent control of a single Si 29 nuclear spin qubit. *Physical review letters*, 113(24):246801, 2014.

[129] Bruce E Kane. A silicon-based nuclear spin quantum computer. *Nature*, 393(6681):133–137, 1998.

[130] Romana Schirhagl, Kevin Chang, Michael Loretz, and Christian L Degen. Nitrogen-vacancy centers in diamond: nanoscale sensors for physics and biology. *Annual review of physical chemistry*, 65:83–105, 2014.

[131] L Rondin, JP Tetienne, T Hingant, JF Roch, P Maletinsky, and V Jacques. Magnetometry with nitrogen-vacancy defects in diamond. *Reports on Progress in Physics*, 77(5):056503, 2014.

[132] Dieter Suter and Fedor Jelezko. Single-spin magnetic resonance in the nitrogen-vacancy center of diamond. *Progress in nuclear magnetic resonance spectroscopy*, 98:50–62, 2017.

[133] Marcus W Doherty, Neil B Manson, Paul Delaney, Fedor Jelezko, Jörg Wrachtrup, and Lloyd CL Hollenberg. The nitrogen-vacancy colour centre in diamond. *Physics Reports*, 528(1):1–45, 2013.

[134] Christian L Degen, F Reinhard, and P Cappellaro. Quantum sensing. *Reviews of modern physics*, 89(3):035002, 2017.

[135] Arthur Schweiger and Gunnar Jeschke. *Principles of pulse electron paramagnetic resonance*. Oxford University Press, 2001.

[136] NB Manson, JP Harrison, and MJ Sellars. Nitrogen-vacancy center in diamond: Model of the electronic structure and associated dynamics. *Physical Review B*, 74(10):104303, 2006.

[137] David A Broadway, James DA Wood, Liam T Hall, Alastair Stacey, Matthew Markham, David A Simpson, Jean-Philippe Tetienne, and Lloyd CL Hollenberg. Anticrossing spin dynamics of diamond nitrogen-vacancy centers and all-optical low-frequency magnetometry. *Physical Review Applied*, 6(6):064001, 2016.

[138] E. L. Hahn. Spin echoes. *Phys. Rev.*, 80:580–594, 1950.

[139] H. Y. Carr and E. M. Purcell. Effects of diffusion on free precession in nuclear magnetic resonance experiments. *Phys. Rev.*, 94:630–638, 1954.

[140] Saul Meiboom and David Gill. Modified spin-echo method for measuring nuclear relaxation times. *Review of scientific instruments*, 29(8):688–691, 1958.

[141] Terry Gullion, David B Baker, and Mark S Conradi. New, compensated Carr-Purcell sequences. *Journal of Magnetic Resonance (1969)*, 89(3):479 – 484, 1990.

[142] Setrak J Balian, Ren-Bao Liu, and TS Monteiro. Keeping a spin qubit alive in natural silicon: Comparing optimal working points and dynamical decoupling. *Physical Review B*, 91(24):245416, 2015.

[143] Wen Yang, Wen-Long Ma, and Ren-Bao Liu. Quantum many-body theory for electron spin decoherence in nanoscale nuclear spin baths. *Reports on Progress in Physics*, 80(1):016001, 2016.

[144] Dieter Suter and Gonzalo A Álvarez. Colloquium: Protecting quantum information against environmental noise. *Reviews of Modern Physics*, 88(4):041001, 2016.

[145] Linh M. Pham, Stephen J. DeVience, Francesco Casola, Igor Lovchinsky, Alexander O. Sushkov, Eric Bersin, Junghyun Lee, Elana Urbach, Paola Cappellaro, Hongkun Park, Amir Yacoby, Mikhail Lukin, and Ronald L. Walsworth. NMR technique for determining the depth of shallow nitrogen-vacancy centers in diamond. *Phys. Rev. B*, 93:045425, 2016.

[146] André Eckardt and Egidijus Anisimovas. High-frequency approximation for periodically driven quantum systems from a floquet-space perspective. *New journal of physics*, 17(9):093039, 2015.

[147] Soonwon Choi, Joonhee Choi, Renate Landig, Georg Kucsko, Hengyun Zhou, Junichi Isoya, Fedor Jelezko, Shinobu Onoda, Hitoshi Sumiya, Vedika Khemani, Curt von Keyserlingk, Norman Y Yao, Eugene Demler, and Mikhail D Lukin. Observation of discrete time-crystalline order in a disordered dipolar many-body system. *Nature*, 543(7644):221, 2017.

[148] MH Mohammady, GW Morley, A Nazir, and TS Monteiro. Analysis of quantum coherence in bismuth-doped silicon: a system of strongly coupled spin qubits. *Physical Review B*, 85(9):094404, 2012.

[149] Setrak Jean Balian. Quantum-bath decoherence of hybrid electron-nuclear spin qubits. *arXiv preprint arXiv:1510.08944*, 2015.

[150] Dale Li, A. E. Dementyev, Yanqun Dong, R. G. Ramos, and S. E. Barrett. Generating unexpected spin echoes in dipolar solids with π pulses. *Phys. Rev. Lett.*, 98:190401, 2007.

[151] Dale Li, Yanqun Dong, R. G. Ramos, J. D. Murray, K. MacLean, A. E. Dementyev, and S. E. Barrett. Intrinsic origin of spin echoes in dipolar solids generated by strong π pulses. *Phys. Rev. B*, 77:214306, 2008.

[152] AA Maudsley. Modified carr-purcell-meiboom-gill sequence for nmr fourier imaging applications. *Journal of Magnetic Resonance (1969)*, 69(3):488–491, 1986.

[153] Warren S. Warren. Effects of arbitrary laser or NMR pulse shapes on population inversion and coherence. *The Journal of Chemical Physics*, 81(12):5437–5448, 1984.

[154] L. M. K. Vandersypen and I. L. Chuang. NMR techniques for quantum control and computation. *Rev. Mod. Phys.*, 76:1037–1069, 2005.

[155] Andreas Reiserer, Norbert Kalb, Machiel S Blok, Koen JM van Bemmelen, Tim H Taminiau, Ronald Hanson, Daniel J Twitchen, and Matthew Markham. Robust quantum-network memory using decoherence-protected subspaces of nuclear spins. *Physical Review X*, 6(2):021040, 2016.

[156] Jonathan Zopes, K Sasaki, Kristian S Cujia, Jens M Boss, Kevin Chang, Takuya F Segawa, Kohei M Itoh, and Christian L Degen. High-resolution quantum sensing with shaped control pulses. *Physical review letters*, 119(26):260501, 2017.

[157] J Casanova, Z-Y Wang, I Schwartz, and MB Plenio. Shaped pulses for energy efficient high-field NMR at the nanoscale. *arXiv preprint arXiv:1805.01741*, 2018.

[158] Wen Yang and Ren-Bao Liu. Quantum many-body theory of qubit decoherence in a finite-size spin bath. *Physical Review B*, 78(8):085315, 2008.

[159] Thomas Unden, Priya Balasubramanian, Daniel Louzon, Yuval Vinkler, Martin B. Plenio, Matthew Markham, Daniel Twitchen, Alastair Stacey, Igor Lovchinsky, Alexander O. Sushkov, Mikhail D. Lukin, Alex Retzker, Boris Naydenov, Liam P. McGuinness, and Fedor Jelezko. Quantum metrology enhanced by repetitive quantum error correction. *Phys. Rev. Lett.*, 116:230502, 2016.